Author/s:
He, Xin

Title:
Development of Multispectral Image Sensors by Exploring Nanophotonics

Date:
2020

Development of Multispectral Image Sensors by Exploring Nanophotonics

Xin He

ORCID iD: 0000-0002-5843-0332

Doctor of Philosophy

July 2020

Melbourne School of Engineering

Department of Electrical and Electronic Engineering

Submitted in partial fulfilment for the degree of

Doctor of Philosophy

Abstract

Development of Multispectral Image Sensors

by Exploring Nanophotonics

Author: Xin He

Principle Supervisor: Dr Ranjith Rajasekharan Unnithan

Co-Supervisors: Dr Hemayet Uddin

& Prof Ampalavanapillai Nirmalathas

A multispectral image camera system captures image data within specific wavelength ranges in narrow spectral bands across the electromagnetic spectrum. In the recent years, image sensors integrated with multiple optical filters with narrow spectral width have been widely used for most of the multispectral imaging across multiple applications, such as area imaging, medical detection, object identification, remote sensing and so on. There were two kinds of multispectral imaging system reported before. The first one is multispectral image cameras that combines multiple cameras mounted with optical bandpass filters and optics with different peak wavelengths and their spectral width depends on applications. The second imaging system is a single sensor based multispectral camera that integrates multiple filters (called filter mosaic) on a single image sensor. The existing filter mosaic fabrication technology disclosed so far is using multilayer coating technique and requires highly accurate alignment with

micro-lithography facility. Based on this manufacturing process, each filter has to be fabricated separately with multiple steps, such as baking, exposure, development which significantly increases the fabrication complication and cost. This limits the wide use of this promising multispectral imaging in many applications.

This thesis investigates the development of new low-cost single sensor based multispectral cameras using different filter mosaic technologies exploring plasmonics, multilayer coating based on heterostructured dielectrics or hybrid metal-dielectric structures.

The thesis starts with an introduction, Chapter 1 presenting the filter technologies, simulation techniques and fabrication technologies. This is followed by presenting a novel technique to enhance the transmission efficiency of plasmonic colour filters based on the coaxial hole array in Chapter 2. Chapter 3 demonstrates CMY camera (cyan, magenta and yellow) using subtractive colour mixing. A colour filter mosaic made of metal-dielectric-metal nanorods is developed and then integrated on a MT9P031 CMOS image sensor to demonstrate its performance. In Chapter 4, the multispectral image camera based on a single sensor is developed using a hybrid filter mosaic integrated onto a Sony monochrome image sensor. Moreover, the multispectral imaging algorithm is used to reconstruct a colour image of a 24 - patch Macbeth Chart. Later, this image sensor was integrated with a DJI drone for the area imaging application. Chapter 5 presents new multispectral filter technologies which is polarization and incident angle independent. Lastly, Chapter 6 presents conclusions and discusses the future research directions. Appendix presents an optical bandpass filter mosaic and multispectral camera based on a mass producible filter technology with spectral width of only 17nm in the near IR wavelength and this technology is confidential and licensed as a trade secret to the University of Melbourne. Therefore, only parts of the technology is disclosed in the appendix due to a company formation (PIXsensor).

Declaration

1. The thesis comprises only my original work towards the Doctor of Philosophy except where indicated in the preface;
2. Due acknowledgement has been made in the text to all other material used;
3. The thesis is within maximum word limit in length, exclusive of tables, maps, bibliographies and appendices.

Xin He

July 2020

Preface

This thesis is mainly based on four journal papers (three published and one under review) and four peer reviewed conference publications. The author of this thesis is the primary author and main contributor of all the eight publications. The thesis author also designed the structures, performed the simulations, fabricated and tested the devices as well as wrote the manuscripts.

Chapter 2, Chapter 4 and Chapter 5 in this thesis is based on the publications below, the permission to reuse the journal articles were granted and listed below:

1. Reproduced from [**Xin He**, Yajing Liu, Kumar Ganesan, Arman Ahnood, Paul Beckett, Fatima Eftekhari, Dan Smith, MD Hemayet Uddin, Efstratios Skafidas, Ampalavanapillai Nirmalathas, and Ranjith Rajasekharan Unnithan, "A Single Sensor Based Multispectral Imaging Camera using a Narrow Spectral Band Colour Mosaic Integrated on the Monochrome CMOS Image Sensor", APL Photonics, 5, 046104, 2020], with the permission of AIP Publishing.
2. © [2018] IEEE. Reprinted, with permission, from [**He, X**.; O'Keefe, N.; Liu, Y.; Sun, D.; Uddin, H.; Nirmalathas, A.; Unnithan, R. R. , Transmission Enhancement in Coaxial Hole Array Based Plasmonic Color Filter for Image Sensor Applications, IEEE Photonics Journal, and Aug/2018 of publication]
3. **He, X.**, Liu, Y., Beckett, P., Uddin, M.H., Nirmalathas, A. and Unnithan, R.R. (2020), Hybrid Color Filters for Multispectral Imaging. Adv. Theory Simul.. doi:10.1002/adts.202000137

Moreover, contents in Chapter 3 is from submitted manuscript (under review) as following:

1. **Xin He**, Yajing Liu, Paul Beckett, Hemayet Uddin, Ampalavanapillai Nirmalathas, and Ranjith Rajasekharan Unnithan, A CMY camera using nanorod filter mosaic integrated on a CMOS image sensor.

Lastly, some contents in this thesis are from the peer reviewed conference papers listed below:

1. **Xin He**, Yajing Liu, Hemayet Uddin, Ampalavanapillai Nirmalathas, Ranjith R Unnithan, "Compound Nanostructure of Metallic Nanoholes with 1D Photonic Crystal for Multispectral Imaging Applications", in CLEO 2020, OSA Technical Digest (Optical Society of America, 2020), paper JTu2D.19.
2. **Xin He**, Yajing Liu, Hemayet Uddin, Ampalavanapillai Nirmalathas, Ranjith R Unnithan, "Integration of Angle Independent CMY Nanorod Colour Filter mosaic on CMOS Image Sensor", in CLEO 2020, OSA Technical Digest (Optical Society of America, 2020), paper JTu2D.22.
3. **Xin He**, Yajing Liu, Paul Beckett, Hemayet Uddin, Ampalavanapillai Nirmalathas, and Ranjith Rajasekharan Unnithan "Transmission enhancement in plasmonic nanohole array for colour imaging applications", Proc. SPIE 11200, AOS Australian Conference on Optical Fibre Technology (ACOFT) and Australian Conference on Optics, Lasers, and Spectroscopy (ACOLS) 2019, 112003M (30 December 2019); doi:10.1117/12.2541299
4. **Xin He,** Nicholas O'Keefe, Dechuan Sun, Yajing Liu, Hemayet Uddin, Ampalavanapillai Nirmalathas, and Ranjith Rajasekharan Unnithan, "Plasmonic Narrow Bandpass Filters Based on Metal-Dielectric-Metal for Multispectral Imaging," in CLEO Pacific Rim Conference 2018, OSA Technical Digest (Optical Society of America, 2018), paper Th4E.5.

Conference Presentations:

1. **<u>Xin He</u>**, Yajing Liu, Fatima Eftekhari, Guangyuan Si, Tatiana Pinedo Rivera, Yang Lim, Dan Smith, Hemayet Uddin, Ranjith Rajasekharan Unnithan, "Recent Lithography Technologies for Optical Filter Fabrication", CSIRO event, ANFF-VIC Capability Update, Melbourne, February 2019.
2. **<u>Xin He</u>**, Yajing Liu, Nicholas O'Keefe, Dechuan Sun, Noor E Karishma Shaik, Fatima Eftekhari, Ranjith Rajasekharan Unnithan, "Infrared Filters based on Metal Dielectric Metal for Multispectral Image Sensors", International Conference on Emerging Advanced Nanomaterials (ICEAN), Newcastle, October 2018.

Acknowledgement

This 3.5 years' PhD study makes my life much more meaningful than when I started to work 3.5 years ago. Research is an unknown journey that is quite different from the coursework study. For example, there is no clear outline telling PhD scholars what they should learn or which way is correct. Researchers are more like adventurers, they need to learn from their failures, but also must know why they are successful after so many attempts. Different from industrial research, academic research concentrates more on the novelty or creativity. A new idea could come from daily life, such as Newton discovered gravity after an apple fell on his head. My supervisor said that academic researchers spend majority of their time creating novel idea or technology, but industrial researchers use 90% of their time doing the development and optimization. During this 3.5 years, I not only did a large amount of academic work but also licensed one of my filter mosaic designs and fabrication methodology to the University for a company formation (PIXsensor). I am proud of myself after these 3.5 years' study because of the excellent learning outcomes and research skills developed. Therefore, I would like to sincerely thank my principal supervisor Dr Ranjith R Unnithan, if he did not choose me as his PhD student, I would not have achieved the performance today including proving myself.

I would like to thank my parents and parents in law for their support. Due to my progress review was held in February every year, it was hard for us to participate spring festivals with them. I also want to thank my cousin Yichun Lu, although she lived with my wife and me for only 2 years during this time, she always shared her funny stories happened in her school, which made us relaxed after work. I would like to thank my wife Yajing Liu for her selfless care. She chose to stay with me every spring festival instead of going home to see her family. Moreover, my wife also gave me valuable suggestions while working in the same group. I would not have achieved this performance without her help in my life. Lastly, I would like to thank other people below who gave me help in these three years:

Co-supervisor: Dr Hemayet Uddin and Prof Ampalavanapillai Nirmalathas.

Collaborators: Dr Paul Beckett

Trainers: Dr Kumar Ganesan, Dr Arman Ahood, Dr Fatima Eftekhari, Dr Yang Lim, Mr Dan Smith, Dr Guangyuan Si, Dr John Zhu, Dr Abu Sadek, Dr Ricky Tjeung, Dr Ash dyer, Dr Tatiana Pinedo Rivera, Mr John Paul Teodosio, Dr Vahid R. Adineh.

DEDICATED TO

MY PARENTS, PARENTS IN-LAW AND MY WIFE

Contents

List of Contributions

The contributions or innovations of this thesis are presented below:

(1) The coaxial hole array based plasmonic colour filters have advantages such as fine wavelength tuneability, use of single nanoscale metal layer, incident angle insensitive and polarization independent. However, this kind of structure has limited transmission efficiency, due to the peak wavelength depends on the spacing (details in Chapter 2) that is around 10nm, which results in a transmission efficiency less than 10%. Therefore, there needs a way to enhance the transmission efficiency. I have developed a new strategy to enhance the transmission efficiency of the coaxial hole array based plasmonic colour filters without compromising their advantages.

(2) CMY colour camera is different from the RGB counterpart where the subtractive colours cyan, magenta and yellow are used. In RGB space, a red filter transmits only about 1/3 of the visible light as the remaining light is absorbed in the filter (only red light pass through the filter). In general, CMY colour filters pass approximately twice the spectral power compared to RGB filters and so are promising candidates for low-light imaging applications. Examples include

astronomical imaging, of nebula and the like, that are characterized by weak images against a dark background. Conventional CMY colour filters made of pigments and dyes are limited in performance for the next generation image sensors with submicron pixel size. This is because the conventional CMY filters cannot be fabricated in nanoscale as they use their absorption properties to subtract colours. Since the image companies started making the submicron pixel image sensors (for example, Sony's 800 nm pixel sensor media announcement), there is an urgency for different CMY colour filter technologies suitable for the submicron pixels. I have developed a new CMY camera using polarization independent nanoscale CMY colour filter mosaic made of Al-TiO_2-Al nanorods integrated on a MT9P031 CMOS image sensor, and the colour imaging is demonstrated with the standard 12 colour Macbeth colourchecker.

(3) Multispectral imaging has wide applications in the area imaging, medical care, precision agriculture and so on. There are two kinds of multispectral imaging system (shown in Chapter 1). The first one combines multiple cameras, each of them is mounted with optical bandpass filters and optics. This makes them heavy, power hungry and will create image coregistration problem. The second one is

single sensor based multispectral camera (SSMC) using a filter mosaic that has multiple filter bands. This SSMC overcomes the limitations of the conventional MCs. They are much lighter compared with the former one, but each filter has different thickness that requires “n” manufacturing process, where n is the number of bands (filters). This makes the SSMCs very expensive due to complexity of their manufacturing. I have developed a filter mosaic technology where all the bands in the filter mosaic can be fabricated in a single stage. Furthermore, the filter mosaic was integrated onto a Sony monochrome image sensor to make a SSMC. I have demonstrated the performance using a Macbeth color chart and by retrieving individual bands from the Macbeth chart. The SSMC was then fitted onto a DJI drone to demonstrate its imaging capabilities in a field.

(4) I have demonstrated another multispectral filter mosaic technology based on computational simulations in Chapter 5. This new filter technology only requires single exposure fabrication for all the bands. Moreover, this kind of technology is also polarization and incident angle independent.

(5) Appendix demonstrates my IP disclosure (licensed for PIXsensor company formation). The multispectral camera with different

number of bands (from 3 to 6) is developed using a novel filter mosaic design and fabrication strategy using mass producible, photolithography. The peak wavelength varies from 500nm to 900nm with spectral width at FWHM from 17nm to 50nm. This multispectral camera is then used to analyse plant conditions.

Table of Figures

List of Abbreviations

AFM	Atomic force microscopy
ALD	Atomic layer deposition
CFA	Colour filter array
DRIE	Deep reactive-ion etching
EBL	Electron beam lithography
FEM	Finite element method
FIB	Focused ion beam
FWHM	Full Width Half Maximum
GMRF	Guided-mode resonance filter
HV	High voltage
IPA	Isopropyl alcohol
LSP	Localized surface plasmons
MC	Multispectral camera
MDM	Metal-Dielectric-Metal
MIBK	Methyl isobutyl ketone
NIR	Near infrared
MIS	Multispectral imaging system
PBC	Periodic boundary condition
PD	Photodetector

PEC	Perfect electric conductor
PECVD	Plasma-enhanced chemical vapor deposition
PML	Perfect matched layer
PMMA	Polymethyl methacrylate
PMC	Perfect magnetic conductor
PPA	Polyphthalamide
SBC	Scattering boundary condiction
SEM	Scanning electron microscopy
SPP	Surface plasmon polaritons
SSMC	Single sensor based multispectral camera
TE	Transmission efficiency
t-SPL	Thermal scanning probe lithography

Chapter 1 Introduction

1. Background

1.1 Conventional Colour Filters and Image Sensors

Since the first colour digital camera came to the market in 20^{th} century, image sensor research has enjoyed a boom time. The image sensor in camera is the essential part that converts an optical signal to digital. This digital signal can then further be processed for the colour reconstruction, resulting in a colour image.

The resolution of an image sensor is directly determined by the number of pixels. In a typical array, such as the one shown below in Figure 1.1, for example, a microlens array is positioned on top in order to focus the incident light [1-10]. The focused light will then reach the colour filter array (CFA), and only the desired colour of light, i.e., that in a particular band of wavelengths, will pass through this layer to be collected by the photodetector (PD). Subsequent steps may include additional analog processing or analog to digital conversion [1-14], followed by colour reconstruction and the application of interpolation, or smoothing algorithms (also called "demosaicing"). Additionally, the black matrix within the structure shown in Figure 1.1 below acts to isolate adjacent pixels when integrating the CFA onto the substrate.

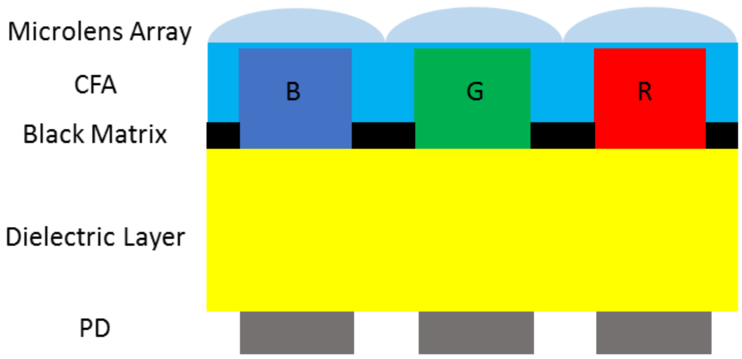

Figure 1.1 2D schematic of pixel structure.

One example of the integration of CFA onto an image sensor can be found in [8], and the process is illustrated below:

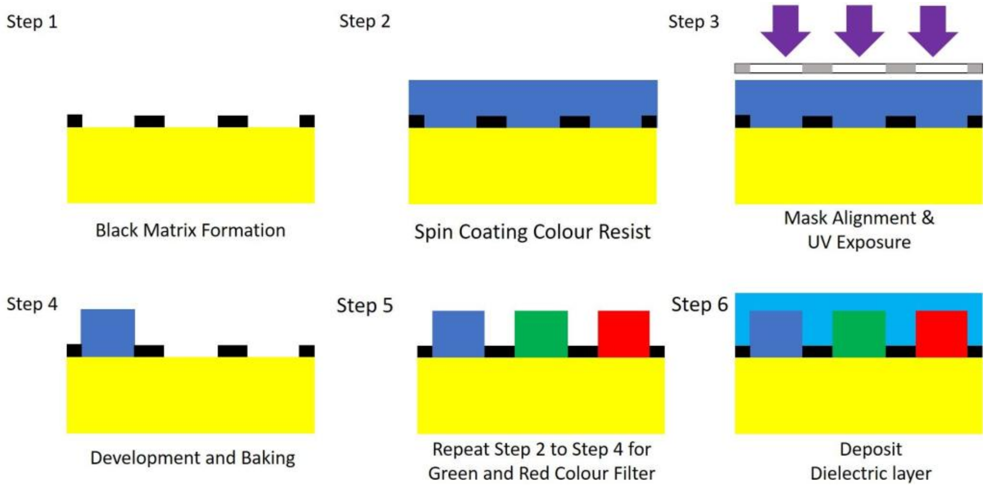

Figure 1.2 Manufacturing process for fabricating conventional colour filter on a thin dielectric substrate.

In the CFA fabrication outlined in Figure 1.2, a very thin dielectric, typically Si_3N_4 or SiO_2 is used to form the substrate, which is in direct contact with the PD within the image sensor. Therefore, a thinner dielectric substrate results in the less spatial crosstalk between adjacent pixels, and, ideally, the CFA should directly contact the PD. There are many different kinds of conventional colour filter material, most of them company-confidential. An organic polymer-based colour resist is used here as an example. This colour filter material can be spin-coated onto a substrate and behaves like a negative photo resist in that the part exposed by the UV light will remain after the development and baking. The colour resist would become harder when exposed UV light, usually, the exposure time must be well tested, too long or short exposure time results in a unperfect exposed shape. Moreover, the developing time must be very accuracy within 1s tolerance, more or less time could introduce the size of the developed area becomes larger or smaller, respectively. The baking temperature should also be verified, too high temperature would melt the colour resist rather than make it stay on the substrate. So the colour resist material is sensitive to the UV radiation and some chemical solutions like developer. The same steps need to be used for all the remaining filters. Thus, during the UV exposure, the mask must be carefully aligned, both with the underlying PD and with the adjacent layers. Finally, a thin dielectric layer is deposited resulting in a flat surface on which the microlens array can be integrated. In some of the commercial work that has been disclosed, ITO is used for this layer [8].

I have undertaken a preliminary experiment to investigate the structure and properties of a typical CFA and microlens array. Here, the image sensor of a CANON 1000D camera was used and was removed after disassembling the camera (Figure 1.3a-c). The lowpass filter (UV block filter) was removed with knife, and the protective glass was also removed with laser cutter (Figure 1.3d).

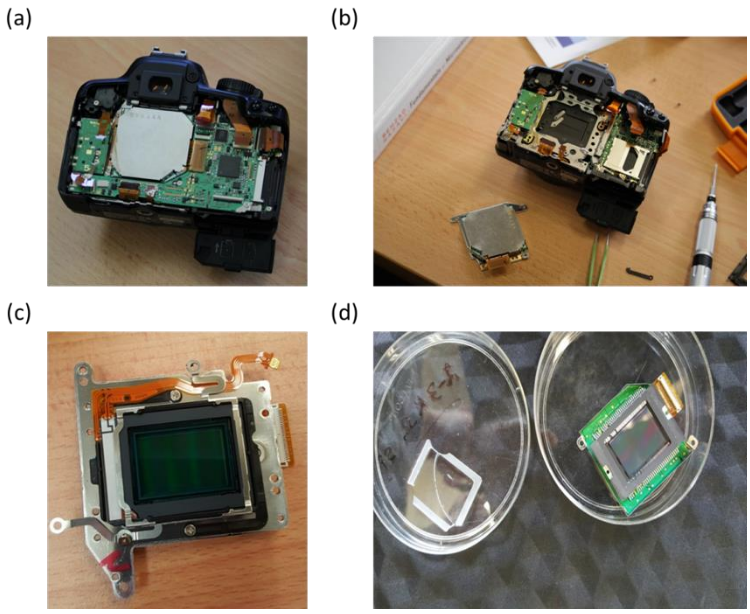

Figure 1.3 Process to remove the image sensor out from the camera

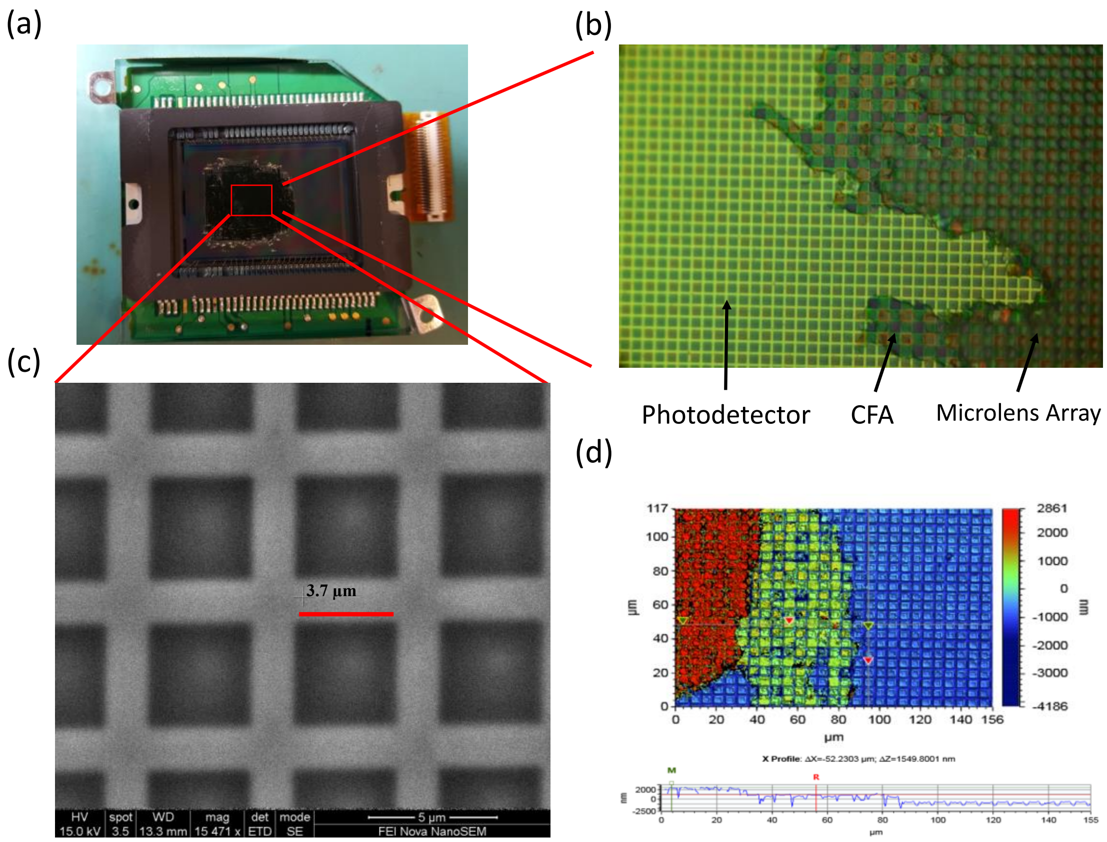

Figure 1.4 The experiments with image sensor of CANON 1000D camera (a) After Bayer layer removal, (b) Microscopic image of the microlens array, CFA and PD, (c) PD measurement with SEM, (d) Height measurement with optical profilometry.

The next step is to remove the bayer layer from the image sensor. Firstly, the image sensor was exposed to an oxygen plasma with 50W power for two hours, which softened the microlens array and colour filter layers sufficiently to allow them to be easily removed with a purpose-built wooden scraper (Figure 1.4a). In the microscope image shown in Figure 1.4b, the microlens array and CFA are totally removed on the left side, while only the microlens array was removed from the area in the center of the image. In Figure 1.4c, a scanning electron microscopy (FEI NovaNanoSEM-430) was used to image the PD under each pixel more accurately. It was observed that the sensitive area is about 70% of the overall pixel size of 5.6µm X 5.6µm indicating that in order to avoid introducing spatial crosstalk, the tolerance for misalignment between the CFA and PD must be less than 1.7µm. In Figure 1.4d, an optical profilometer (Bruker Contour GT-I) was used to measure the thickness of CFA, which was found to be approximately 1.5µm. So according to the measurement, the minimum required colour resist volume to produce different colour is $\mathrm{V = s \times h = d^2 \times h = 5.6^2 \times 1.5 = 0.04704ml}$.

Therefore, it could be concluded that the conventional colour filters have the following disadvantage [15-23]: materials (or at least the ones that have been disclosed to date) seem to be sensitive to the UV light and some chemical solution, such as developer, it also would become unstable at elevated temperatures. The organic dye based material requires certain volume to produce different scattering colours, which results in a large thickness of 1.5µm has potential to produce more spatial crosstalk between adjacent pixels when the pixel size is reduced to submicron-meter scale. Finally, the CFA manufacturing requires multiple steps for each filter, and therefore increases the fabrication cost and complication when the number of filters increases.

1.2 Multispectral Imaging System and its Applications

1.2.1 Current Multispectral Imaging System in the Market

The concept of a multispectral imaging system (MIS) was invented decades ago and since then has attracted much research across a range of applications. MIS captures images in narrow spectral bands across the electromagnetic spectrum. Depending on the application, the spectral width varies between 10 nm and 90 nm.

Generally, there have been three broad classes of MIS organisation reported previously. The first uses a narrow band illuminator [30-33]. In this case, the most general (i.e., cost effective) image sensors in the market can be employed as long as their sensitive wavelength covers their range of interest. Therefore, the key technology driver to narrow down the target by reducing the FWHM operates on the transmitter (illuminator) rather than the receiver (sensor).

The second is called "push-broom" MIS in which the incident light is split into multiple bands with different peak wavelengths and small FWHM. While a simple prism can act as a beam splitter, the optical system in this MIS can still be very complicated because it often needs multiple reflections with many prisms. Therefore, the whole imaging system becomes very bulky, as demonstrated in [34].

The third class of MIS uses narrow bandpass optical filters and avoids the need for additional illuminators or a complicated optical system. This type of MIS can either use a simple optical filter wheel with a single camera [27] or associate the separate bandpass filters with multiple cameras [35-36]. However, these may still exhibit large size and weight that can limit their applications. In both cases, these MIS systems results in image co-registration problems. In the optical filter wheel case, the narrow band images corresponding to a single "shot" are separated in time, thus causing problems with overlapping moving targets and the like. In systems with multiple cameras, each of the images is taken from a slightly different field of view. In either case, significant further image processing will be required [37-40].

Single sensor based multispectral image systems have emerged recently onto the market [41-43]. This class of MIS integrates the narrow bandpass filter array directly on the image sensor. However, while in most cases the details of the specific filter technology is carefully guarded trade secret, some narrow bandpass filter patents plus work from IMEC [41] reveal filter structures based on multilayer coatings. In this case, the peak wavelength can be tuned by varying material thickness. As a result, each filter has a unique thickness, and the fabrication process required to integrate the filter array onto the image sensor would be similar to the conventional colour image sensor technology. The number of processing steps is directly proportional to the number of bands, which will significantly increase the fabrication cost and complexity for multispectral systems.

1.2.2 Applications of Multispectral Imaging System (MIS)

Examples include MiDAR project funded by National Aeronautics and Space Administration (NASA), which combines narrow band transmitter and receiver system. The objective is to explore aspects of the Earth from the air such as detecting the position of mines. It also has the ability to investigate the underwater conditions [24].

Normalised difference vegetation index (NDVI) is a common measure in remote sensing for agriculture. As healthy leaves emit more NIR light than dead or stressed leaves [29], agriculture research is able to use drones integrated with MIS to over- fly crop regions and quickly determine NDVI based on the equation: $\mathrm{NDVI} = \frac{(\mathrm{NIR}-\mathrm{R})}{(\mathrm{NIR}+\mathrm{R})}$. In this way, it becomes easy to evaluate plant condition in real time and predict important parameters, such as the harvest rate.

MIS also plays an important role in the Healthcare area. MIS techniques operating in the NIR and red edge wavelengths are currently used in hospitals to locate the position of veins [25]. As the NIR light can penetrate the skin and increase the contrast between blood and skin, images of the vein under the skin can be easily found and superimposed on top of the skin. It also can detect disease within some structures in the body [26-28], such as distinguishing the ulcer and erythematous regions.

2. Literature Review on Optical filters

This section would focus on different optical filter design with dielectric based structure (e.g. prism, multilayer coating, dielectric GMRF) and metal containing based structure (e.g. plasmonic filter).

2.1 Optical System based on the Prism/Beam Splitter

Colour camera imaging systems based on interference filters were developed many years ago-as early as 1965 [44-45]. These optical filters are conventionally set up to transmit red, green and blue colours, as these are the basic colours in the additive model. With different combinations of RGB, other colours can be produced. Therefore, this camera system has three interference filters and three sensors to collect the optical intensity value, results in a large, bulky system.

Beam splitting based optics have also been used in the MIS systems [46]. The beam splitter is composed of mirrors and prisms that can transmit and reflect the desired light of interest. The transmitted and reflected light is then filtered by a Bragg grating, where $\lambda = 2d\cos\phi$, λ is the desired peak wavelength, d is the grating pitch size, ϕ is the angle of incident light.

2.2 Multilayer Coating

2.2.1 Fabry–Pérot (FP) Etalon and its Applications in the Optical Filtering

The basic structure of the FP etalon is shown in Figure 1.5. Here, the center medium has a smaller refractive index n_2 than two outer layers (n_1). Normally, a very thin metallic layer would be deposited on the two inner sides of the middle medium to reduce the light leakage.

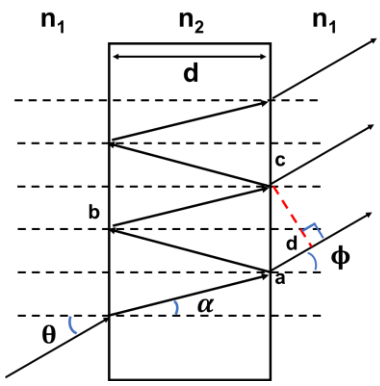

Figure 1.5 The basic structure of the FP etalon

The path difference between two adjacent refraction light is defined as: $\Delta = \mathrm{n_2(ab + bc) - n_1(ad) = 2n_2dcos\,(\alpha)}$, while the relative phase change is: $\eta = \frac{2\pi}{\lambda}\Delta = \frac{4\pi \mathrm{n_2 dcos\,(\alpha)}}{\lambda}$. Thus the transmitted power is maximized when $\eta = 2m\pi$, for m is integer, if it is assumed that the incident angle is 0, then $\alpha = 0$ so that the peak wavelength is given by $\lambda = \frac{2\mathrm{n_2}d}{m}$, m is integer, m=1,2,3…etc.

Further, the metallic coatings can also be replaced by other metal dielectric materials that act as antireflective layer and has the thickness of $\frac{\lambda}{4n}$, where n is the refractive index of the antireflective layer. Many metal-dielectric-metal (MDM) resonators have been proposed to reduce the reflections have also been used for colour filtering [49], as absorber layers [50-52] and antireflection coatings [53-56].

As mentioned above, the mirror does not need to be metallic, but dielectric material can also be used as a mirror. In this case, the large refractive index difference between two adjacent layers is the factor to produce the narrow band filters. In [57], the mirror is made of combinations of dielectric materials with larger refractive index material (i.e., TiO_2) surrounding a smaller one (i.e., in SiO_2 or MgO). As a result, the FWHM was reduced to 10nm and this kind of structure can be thought of narrow bandpass filter. An alternative structure presented in [58] is based on a double FP with a silver mirror and a cavity formed from Ta_2O_5, which results in a FWHM of 50nm. And by replacing dielectric in the middle with photoresist, the FWHM could also be reduced to less than 50nm [59].

2.2.2 Photonic Bandgap and its Applications in the Optical Filtering

A multilayer film structure based on one-dimensional photonic crystals was introduced by John et.al in [60-61]. The propagation speed of light will change in different dielectrics according to the equation: $\mathrm{ck} = \omega(\mathrm{k})\mathrm{n}$, where n is the refractive index of dielectric, k is the wavevector that is periodic in the 1D photonic crystal structure with a period of $2\pi/\mathrm{p}$, and p is the period of the multilayer. When light propagates through this multilayer structure, two adjacent layers with different refractive indices will create a photonic band gap. Note as $\Delta\omega$, the mode with the frequency in the bandgap will be rejected, therefore light with the corresponding wavelength will be rejected.

The gap to mid-gap ratio can be approximated as $\frac{\Delta\omega}{\omega_m} \approx \frac{\sin(\frac{\pi l_1}{\mathrm{p}})\Delta n^2}{\pi n^2}$, where ω_m is the mid-gap frequency and n is the smaller refractive index of the adjacent two layers. It is clear that this ratio will reach maximum when $\frac{l_1}{p} = \frac{1}{2}$. The bandgap will increase as the refractive index difference becomes larger. In other words, if layer 1 as has the refractive index n_1 and thickness l_1 and its adjacent layer 2 with n_2 and l_2, then when $l_1n_1=l_2n_2$, the gap size will be maximized and therefore the incident light will produce a very narrow spectrum. Such an effect can be used to create narrow bandpass optical filters.

Normally, photonic crystal structures are analysed by considered all layers to be formed from dielectric materials. Prior proposals [60-62] in which the adjacent layers are made up of pairs of Si/SiO_2 layers repeated 12 times have shown significantly reduced values of FWHM. In [63], the Metallic Photonic Bandgap structure is repeated 40 times to further reduce the FWHM. Some patents on narrow bandpass filters with multilayer structure were also presented in [64- 70].

2.3 Optical Filter with Dielectric Nanostructure

2.3.1 Dielectric Guided-mode-resonance Filter (GMRF)

The Photonic bandgap filter is based on a dielectric multilayer repeating in the vertical direction. In contrast, the unit nanostructure of the dielectric GMRF repeats in the horizontal direction shown in the Figure 1.6, below. As shown, the permittivity of the top layer and the spacing around the grating (medium 1) is ε_1, while ε_2 and ε_3 are the permittivity of the grating and substrate (medium 2 nd 3), respectively.

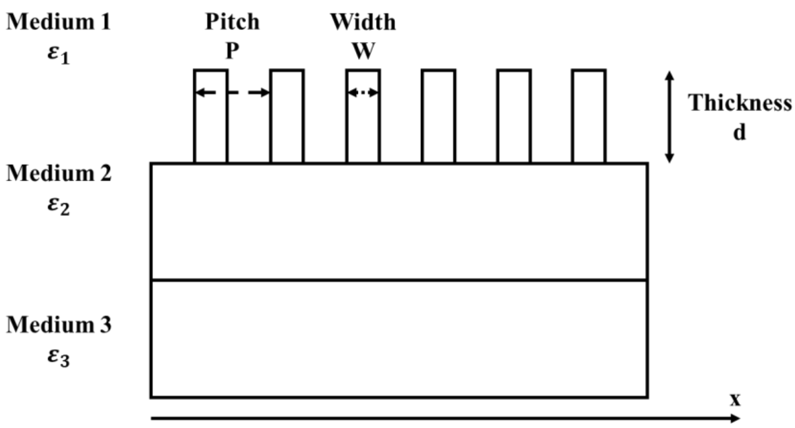

Figure 1.6 2D structure of GMRF in [71]

In this GMRF, $\varepsilon_2 = \varepsilon_g + Acos(\frac{2\pi}{P}x)$, where A is the amplitude P is the pitch (period) of the grating [71]. Therefore, the condition of the GMRF is given by:

$\varepsilon_2 > \varepsilon_g > \varepsilon_1, \varepsilon_3$.

In [72], a single SiN grating layer forming a 1D GMRF was demonstrated a FWHM of less than 1nm while in [73], a double grating structure was also introduced to decrease the

FWHM. However, these techniques may only be able to suppress secondary peaks and produce a sharp peak at certain peak wavelengths within a short range (less than 10nm). By sealing the dielectric grating with another material (e.g. SiO_2…), as shown in Figure 1.7 below, and also increasing the refractive index difference between nH and nL [74], it is possible to achieve a FWHM of less than 1nm as well as suppressing other peaks across the visible wavelength range. This types of structures could become more effective when the peak wavelength can be more easily tuned. Further, 2D GMRFs have also been proposed as good candidates for narrow band filters [75-77]. However, this kind of filters only work in the reflection mode and cannot be used for the multispectral filter.

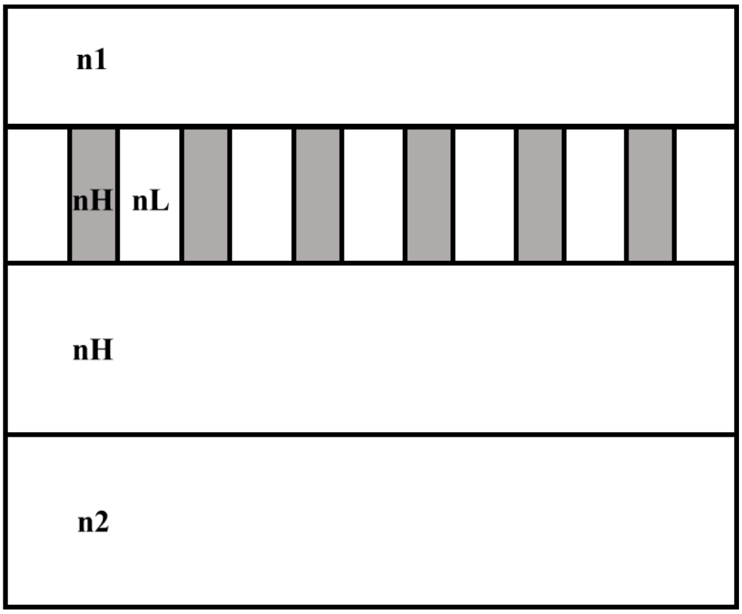

Figure 1.7 Improved dielectric GMRF structure in [74]

2.3.2 Silicon Nanowire

The optical properties of some dielectric nanowires depends on their radius r and the refractive index n of the material with the relationship [78]: $\lambda \approx \frac{2\pi rn}{p}$, p=1,2,3… This equation can also be used for dielectric nanorod, resonator or nanodisk structures, even at larger sizes. It may even be valid when the dielectric material with large refractive index exhibits high confinement modes. Silicon has a large refractive index (as high as 4), and is therefore suitable for use in colour filtering [78-83]. A multispectral filter based on Si nanowire was presented in [80] and used to perform multispectral imaging. A colour image could be reconstructed from the multispectral camera based on the integration of the Si nanowire array onto a monochrome image sensor and, by using NIR illumination, objects behind a black screen could be observed by analysing the data from NIR band of the multispectral camera [80].

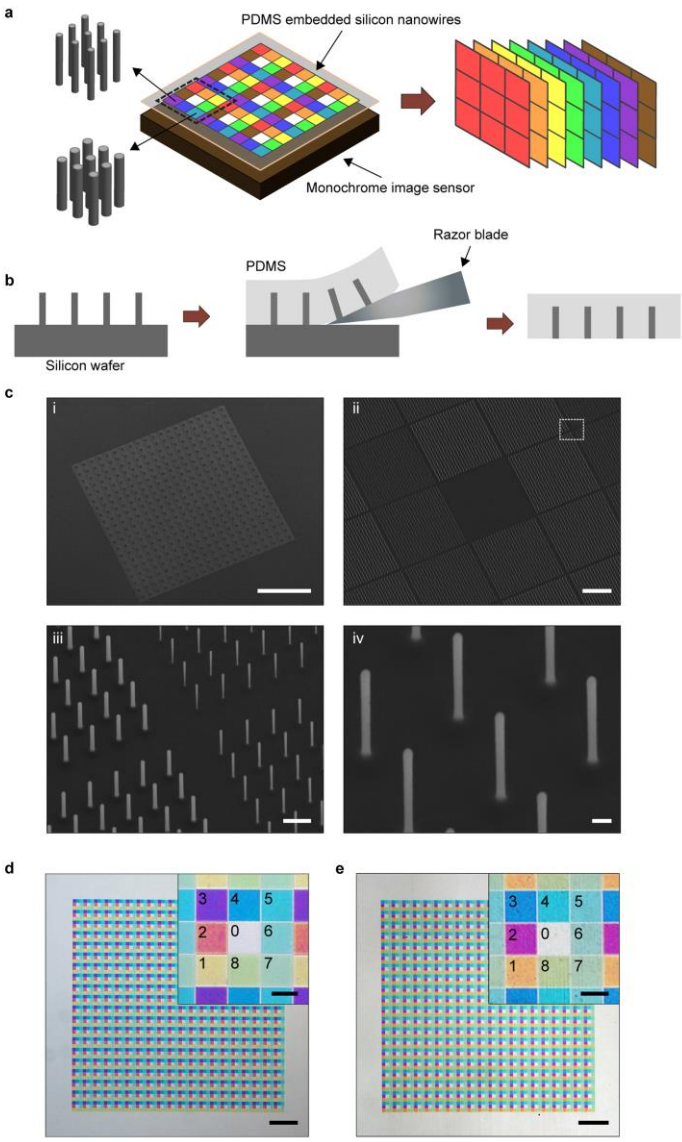

Figure 1.8 Schematic of nanowire based multispectral filter and its microscope images [80].

2.4 Plasmonic Filter

It has been observed that light can be diffracted to different wavelength light while passing through a small metallic hole less than 100nm in diameter [47-48]. The holes may be circular, rectangular, even non-regular in structure. Regardless of the shape, its behaviour can be described and predicted in terms of Plasmonic theory, which comprises two cases. Surface plasmon polaritons (SPP) occurs if the plasmon is excited and propagated at the interface between the metal and dielectric. Additionally, localized surface plasmons (LSP) are evident when the excited plasmons are not propagating at the surface of the metallic nanoparticle (e.g. nanosphere, nanodisk) but it is still coupling to the electromagnetic field [84]. For the SPP, the propagation constant be written as: $\beta = k_0\sqrt{\frac{\varepsilon_1\varepsilon_2}{\varepsilon_1+\varepsilon_2}}$, $k_0 = \frac{\omega}{c} = \frac{\frac{2\pi c}{\lambda}}{c} = \frac{2\pi}{\lambda}$, Whereas for the LSP case, the peak wavelength mostly depends on the size, such as the radius of the nanosphere or nanodisk.

2.4.1 Plasmonic Filter based on the Metallic Nanoslit Grating

For the metallic nanoslit grating structure, the propagation constant while considering the first scattering order is $\beta = \pm\frac{2\pi}{P} + k_0\sin\theta$, where P is the period of the grating and θ is the incident angle. When the angle of incidence of the light is normal to the sensor surface, $\theta = 0$. So that: $k_0\sqrt{\frac{\varepsilon_1\varepsilon_2}{\varepsilon_1+\varepsilon_2}} = \frac{2\pi}{P}$, then $\lambda = P\sqrt{\frac{\varepsilon_1\varepsilon_2}{\varepsilon_1+\varepsilon_2}}$. Thus it can be seen that the peak wavelength is proportional to the grating period.

Based on this theory, the influence on the optical transmission efficiency with grating thickness has been investigated [85]. Many colour filters based on metallic grating has been proposed and analysed. For example, in [22], a 1D Ag nanoslit grating on the quartz was shown to reach 60% transmission efficiency while producing subtractive colour primaries: yellow, magenta and cyan. More recently, a MDM nanoslit grating was also shown to produce additive colours, such as red, green and blue colour [86-87]. Metal nanoslit gratings have also been used for the narrow bandpass filters with smaller FWHM [23, 88-90]. The dual MDM grating filter (repeating in the horizontal direction) exhibits a FWHM of 64nm at a wavelength around 1500nm [23].

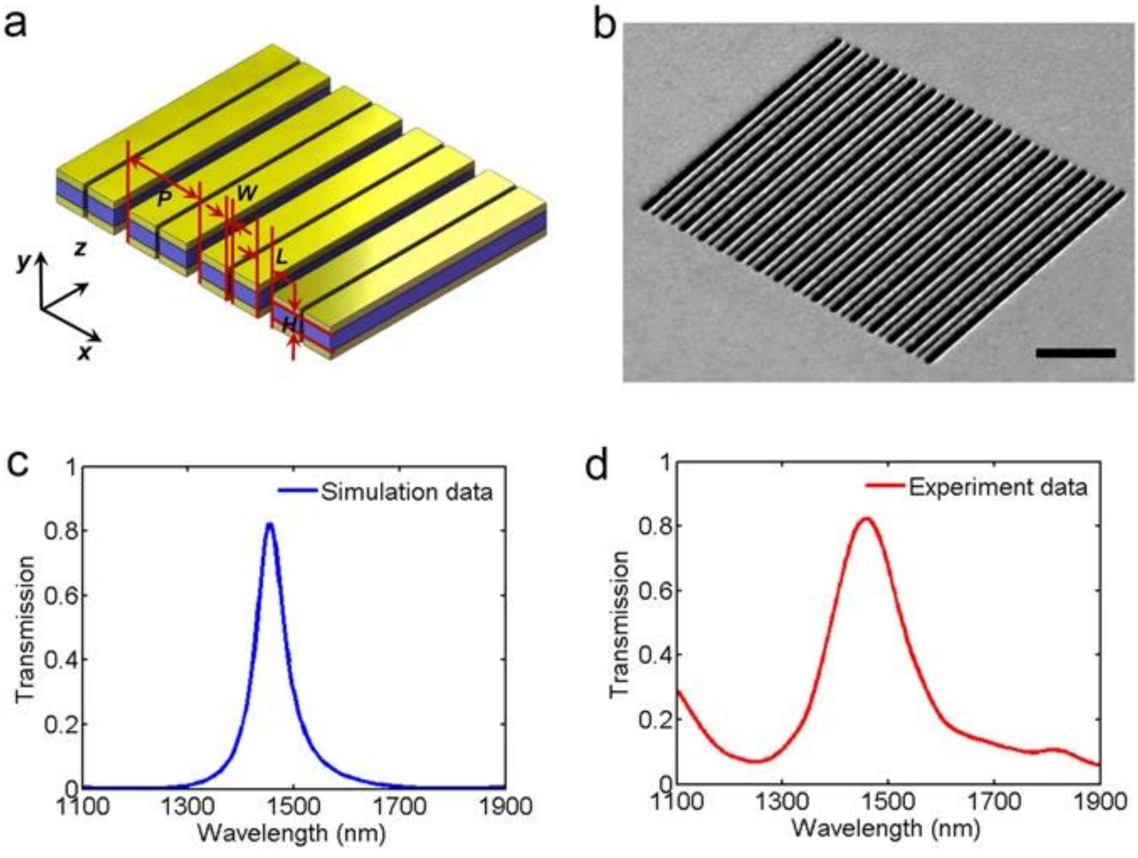

Figure 1.9 Schematic of multispectral filter based on dual MDM grating [23].

The MDMDM nanoslit grating (i.e., double MDM repeating in the vertical direction) proposed in [88], has a minimum FWHM of less than 30nm while a simple Al nanoslit on a Al_2O_3 buffer layer has been shown to reduce the FWHM to around 14nm [90].

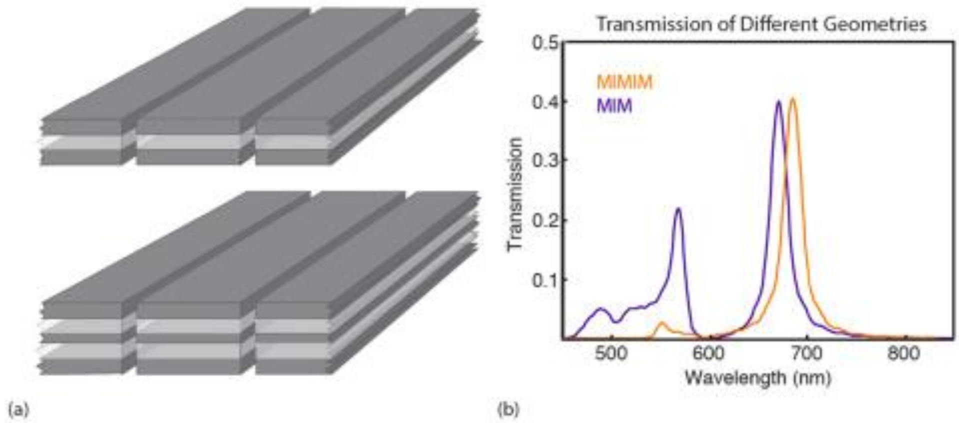

Figure 1.10 Schematic of MDM and MDMDM nanoslit grating and their results [88].

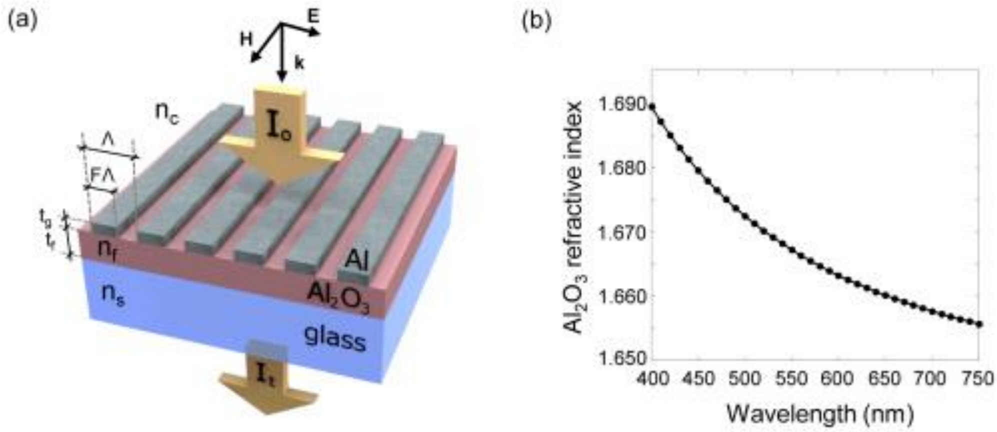

Figure 1.11 Schematic of multispectral filter based on Al nanoslit on a Al_2O_3 buffer layer

However, a major problem with the metallic nanoslit grating is that it is polarization dependent that could be described as the spectrum under TE wave would be different from that under TM wave, which was proved from the theory and experiments [15-23, 44-45, 84]. This feature may be a disadvantage for imaging applications if the incident light is polarized. Consequently, the optical system may need additional optics, such as a polarizer. When the incident light combines TE and TM wave. In such cases, where one polarization mode is blocked and thus only one is effective, the available optical power is reduced by half.

2.4.2 Plasmonic Filter based on the Metallic Nanohole Array

There are two common arrangements of metallic nanohole array: square and hexagonal. The propagation constant (β) of both of these topologies can be described as [47]:

$\beta = K_0\sin\theta \pm nG_x + nG_y = K_0\sin\theta \pm (n+m)\frac{2\pi}{p}$ and the peak wavelength (λ) will be given for square array: $\lambda = \frac{P}{\sqrt{\frac{4}{3}(n^2+m^2)}}\sqrt{\frac{\varepsilon_1\varepsilon_2}{\varepsilon_1+\varepsilon_2}}$ and hexagonal hole array: $\lambda = \frac{P}{\sqrt{\frac{4}{3}(n^2++nm+m^2)}}\sqrt{\frac{\varepsilon_1\varepsilon_2}{\varepsilon_1+\varepsilon_2}}$, where n and m are the scattering order, ε_1 and ε_2 are the dielectric constant of the dielectric and metal.

These models have been used previously to analyse the behaviour of plasmonic colour filters formed from hexagonal hole arrays in aluminium films [15, 18, 91-94]. The FWHM has been shown to vary from 90nm to 180nm while the peak wavelength is the red region. Moreover, a plasmonic colour filter formed using a hexagonal hole arrangement is polarization independent and has higher transmission efficiency than the square array [18].

Most recently, a large plasmonic colour filter array was fabricated and integrated on a monochrome CMOS image sensor. After the image processing steps such as demosaicing, white balance and gamma correction, a full colour image could be reconstructed [93].

Multispectral filters based on metallic hole arrays have been presented that operate at visible and NIR wavelengths [21, 95-96]. A nanohole array inserted in gold film was fabricated with EBL patterning followed by wet etching [96]. The measured FHWM is around 100nm with 60% transmission efficiency. This multispectral filter has been integrated with an optical system, including a telecentric lens and CMOS image sensor, to image leaf at different wavelengths. Another multispectral filter based on a gold nanohole array was fabricated on a GaAs substrate for the mid IR imaging which is from 7µm to 14µm. It is assembled with a thermal camera in a black body, to reconstruct images of hot metal objects under 100°C [96]. The FWHM is around 450nm.

2.4.3 Plasmonic Filter based on the Metallic Nanoparticle

The optical properties of metallic nanoparticles can be represented by the LSP theory, in which the resonant wavelength is strongly determined by its size, rather than the period [84, 97-102]. Note that the resonant wavelength here is the valley wavelength, the region of minimum transmission. The resulting colour is subtractive colours, such as cyan, magenta and yellow, but not additive colours like red, green blue. Examples includes arrays using aluminium disks [98-99], silver disks [100] and gold nanorods [102]. The 40nm Ag disk colour filter has maximum transmission efficiency around 60%, and its resonant wavelength remains constant across a range of incident angles up to 80° [100]. Even though the first peak would reduce but has little effect on the produced colour. Even the spectrum of the 20nm Al disk in [98-99] shows no changes as the incident angle varies from 0° to 70°. The reason is probably the thinner disk is more symmetrical than the thicker disk and therefore more insensitive to the incident angle. Therefore, most LSP based structures are polarization independent and incident angle insensitive, except some structures with larger thickness such as nanorod, which offers an advantage over SPP based filters. Moreover, they also transfer much larger optical power levels than the additive colour filter, making them better suited for the photographic targets with extremely dark background. However, there have been no subtractive colour filters integrated on the image sensors for colour imaging introduced before, and this will be the subject of Chapter 3.

2.4.4 Plasmonic Filter based on the Metallic Apertures

The theory of single coaxial hole inserted in the metal film was derived in a sphere coordinate [103] and the peak wavelength is determined by the spacing in the coaxial holes, but not the hole size or the period. The wavelength dependent propagation constant is: $\beta = \frac{m\pi - \varphi}{d}$, where m=1, 2, 3,…etc, φ is the reflection phase, d is the thickness of the metal film [19].

Coaxial hole structures also exhibit the Metal-Dielectric-Metal FP effect, and so will also result in a narrow-band spectrum. In [103], a filter was presented where the peak wavelength varied from 500nm to 650nm, as the spacing between Au coaxial hole changes from 20 to 40nm. The minimum FWHM observed was 40nm [103]. However, the maximum transmission efficiency of this kind of structure is usually smaller than 20% because of the small spacing [103-105]. The plasmonic coaxial holes also have high tolerance to incident angle (FFOV up to 80°) and the array is polarization independent. To compensate for the disadvantage of the small transmission efficiency, this thesis provides a solution in Chapter 2 [17].

2.5 Other colour imaging techniques

It is worth mentioning another imaging technique called multi-colour imager [106]. Different from colour filtering technology, the multi-colour imager uses wavelength-dependent absorbers. The multispectral imaging system could be created by designing multispectral detectors, that is a different research field.

2.6 Conclusions

Colour filters with various structures and materials have been previously described for which the peak wavelength can be tuned to pass different colours by changing thickness of each layer. These include Fabry–Pérot based filters [49-56, 58], photonic bandgap filters [59-62], dielectric multilayer [57, 64-70]). While in some periodic arrays, the peak wavelength is proportional to the pitch size (e.g. dielectric GMRF [71-77], plasmonic grating [22-23, 85-90], nanohole array [15-16, 18, 20-21, 91-96]). For some metallic nanoparticle (e.g. silicon nanowire [78-83], nanodisk [97-100], nanorod [101], nanorectangular [102]), their sizes would determine the peak wavelength. And in some metallic apertures, the peak wavelength relates to the spacing (e.g. coaxial hole [103-105]). However, the maximum transmission efficiency of this kind of structure is usually smaller than 20% because of the small spacing [103-105]. The plasmonic coaxial holes also have high tolerance to incident angle (FFOV up to 80°) and the array is polarization independent. To compensate for the disadvantage of the small transmission efficiency, this thesis provides a solution in Chapter 2 [17].

Different strategies have been employed to reduce the spectral width (FWHM) of the narrow bandpass filters were presented. Most early proposals were based on the dielectric GMRF, for which the FWHM could be less than 1nm. However, this technique covers only cover a limited range of wavelengths and the peak wavelength cannot be easily tuned [71-74]. Later the multilayer coating technologies with tens of layers were introduced [57, 64-70]. The main advantages of this structure is that the peak wavelength can be finely tuned by changing the thickness. While this can be achieved precisely using atomic layer deposition (ALD), it requires multiple steps for a large multispectral filter array and extremely accurate alignment between stages during fabrication.

The next stage in the development of multispectral imaging saw the introduction of narrow bandpass filters formed from silicon nanowires were integrated onto a monochrome image sensor. The primary disadvantage of this technique is its large FWHM i.e., larger than 90nm in the proposals to date [80]. Metallic nanoslit grating filters have been shown to have a FWHM of around 20nm [23, 90], but may require additional optics to block one polarization component of the incident light, which then halves the incident optical power. Moreover, to date there has been only one report [107] describing the use of a nanoslit grating in front of an optical system, in this case, the filter was not closely integrated with the image sensor and required very complicated software post-processing to create the image.

A metallic nanohole based narrow bandpass filter was analysed using simulation in [21] and was predicted have a FWHM less than 50nm. Further, narrow metallic nanohole arrays have been fabricated and integrated with a bulky optical system to perform the imaging. These were shown to have FWHM values around 100nm in the visible and NIR wavelength [95] and 400nm at mid-IR wavelengths [96]. At this point in time there has been no previous work demonstrating the integration multispectral filter array using a single exposure fabrication methodology onto a standard image sensor to perform multispectral imaging. This is the focus of Chapter 4 in this thesis.

3 Optical Material

This section would analyse the general material used in the optical filter concluded in the literature review above, such as Fabry–Pérot based filters, photonic bandgap filters, plasmonic grating, nanohole array, metallic nanoparticle and metallic apertures.

For the multilayer structure, including Fabry–Pérot based filters, photonic bandgap filter, dielectric multilayer. The choice of the material highly depends on the operating wavelength of the optical filter. For example, if the optical filter is working in the visible wavelength (from 400nm to 700nm), then the dielectric material, such as SiO_2, MgO, Ta_2O_5, TiO_2 and others that could be transparent in this wavelength range [108]. Among them, TiO_2 can have the largest refractive index of 3.2 in some case [56], which could have larger refractive index difference with SiO_2 (1.42), and therefore becomes common material for this multilayer structure. E-beam evaporator, sputter, PECVD, ALD and Ion beam deposition (IBD) are general deposition facility. In this specific case (Multilayer), the roughness is the biggest challenge, if one layer deposition is not flat enough, the layers above it will not be smooth as well and even worse. From the facilities above, ALD could give a most smooth surface, as it deposits the material in atom scale, but this results in a slowest deposition rate among them. E-beam evaporator seems to be most common deposition facility in the academic research centers, as it has most nanofabrication applications (such as lift off process) that cannot be done with other deposition facilities. Moreover, E-beam evaporator can control the deposition rate and roughness well, but the layers may not condense closely, which would significantly decrease the optical properties of the multilayer based filter. The solution is to use the Ion assist (normally Argon gas) while doing the deposition [108].

For optical filters using Plasmonics theory, metal material is the most important part. Au, Ag and Al are common material for the plasmonic filter operating in the visible and NIR wavelength (from 400nm to 1000nm) [109], as chromium (Cr), nickel (Ni), tungsten (W), and titanium (Ti) would introduce less transmission efficiency and broad spectrum because of its lossy optical property [110]. While Au may not support resonance wavelength larger than 550nm, thus cannot be used for generating the blue and green colours. Ag would be quickly oxidized within two weeks. Moreover, Au and Ag have bad adhesion on most substrates, such as quartz (SiO_2), sapphire (Al_2O_3). They need additional seed layer (such as Cr, Ti), these material may reduce the transmission efficiency and wider the spectrum linewidth as introduced before [111]. There exists some structures not using seed layer between Au or Ag and dielectric substrate, but the filter area are quite small and not practical for the imaging applications [23]. Al has been well known as CMOS compatible material, on the contrary, it does not need seed layer, and the colour filters made of Al also have high transmission efficiency for more than 40% [92-93].

4 Research Methods

4.1 Simulation Methods

The simulation software used in the project is COMSOL Multiphysics based on the finite element methods (FEM) [112]. For example, in the figure below, the 1D curve structure can be divided into small pieces and represented with differential equations. The same method can be applied into 2D and 3D structures, resulting in a mesh (see 4.1.3). Moreover, COMSOL is a powerful software that can simulate applications in the mechanical engineering, chemistry, even nuclear reactor. In this thesis, radio frequency (RF) module is used to design the filter, and this section would explain the simulation methods used in the projects in details.

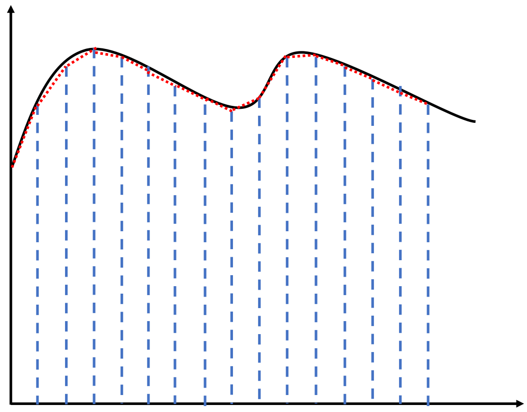

Figure 1.12 theory of differential equation in 1D domain

4.1.1 Geometrical Structure and Material

The first step to do simulation is to construct the geometrical structure. A simple simulation example is shown below, the top and bottom parts are perfect matched layers (PML), its function would be introduced in the next section. The middle part is used to construct the filter, where complicated geometric structure can be designed and built. The rest two parts indicate top coating and the substrate (bottom part in green). If there is no coating on the top of the filter (which means top is air), then semi-infinite conditions can be applied [18], where perfect electric conductor (PEC) and perfect magnetic conductor (PMC) conditions are applied to the layer or boundary perpendicular to the direction of electric field and magnetic field, respectively. Their theory would be presented in the next section.

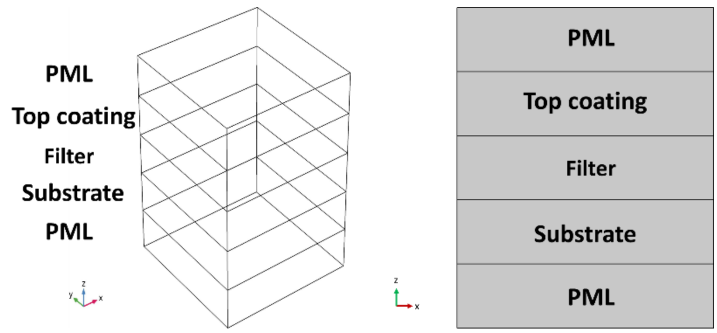

Figure 1.13 Example using COMSOL in 2D and 3D

Material property can be used for the layers in 2D models and domains in 3D models. Refractive index is a very important material property to design the optical filters. In material library in the COMSOL software, these parameters can be directly used. However, the same material deposited with different deposition methods under various environment can be quite different. Therefore, it is much better to measure the exact material property with characteristic facilities, such as ellipsometer. Then these data can be imported to COMSOL with interpolation function. For example, the real and imaginary part for Al can be defined as Al_Re and Al_Im, respectively. Later in the material section, Al refractive index can be expressed as Al_Re(lamd[1/nm]) and Al_Im(lamd[1/nm]) and define the relative layers in 2D models or domains in 3D models, where lamd is the wavelength.

4.1.2 Boundary Conditions

With COMSOL software, several boundary conditions need to be set correctly, different from other simulation software (e.g. FDTD), the incorrect setting could alert users, COMSOL would still give the results that can be not right. Generally, there are 7 kinds of boundary conditions in the RF model which are perfect matched layers (PML), scattering boundary conditions (SBC), port boundary conditions, perfect electric conductor (PEC) conditions, perfect magnetic conductor (PMC) conditions, periodic boundary conditions (PBC) and transition boundary condition (TBC).

4.1.2.1 Perfect Matched Layer (PML) and Scattering Boundary Condition (SBC)

PML has the ability to absorb the reflected light which may be caused by metal material, and therefore exists secondary light source to transmit through the simulation structure, which causes wrong results. However, as mentioned before, these wrong results may be not alerted by the software. To further absorb the reflected light, SBC should be applied around PMLs. Lastly, PML should be applied on the top and bottom of the whole simulation blocks [113] shown in figure below.

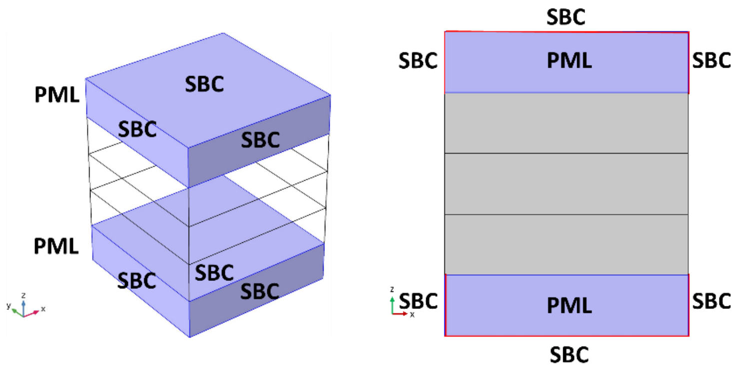

Figure 1.14 Example of using SBC with COMSOL

4.1.2.2 Port Boundary Condition (PBC)

Port boundary conditions are used for the boundaries (in 2D) or the layers (3D) to excite or stop light. Various predefined light sources can be chosen, which are numeric, rectangular and periodic. Users can also define their preferred source in the port mode setting, where the direction of electric or magnetic field, propagation constant $k = \frac{\omega}{c} = \frac{\frac{2\pi nc}{\lambda}}{c} = \frac{2\pi n}{\lambda}$ (n is the refractive index of the layer or domain where exciting and stop the light) and phase direction can be defined. While applying PML on the top and bottom, the interior slit needs to be activated and appropriate direction needs to be set as shown below:

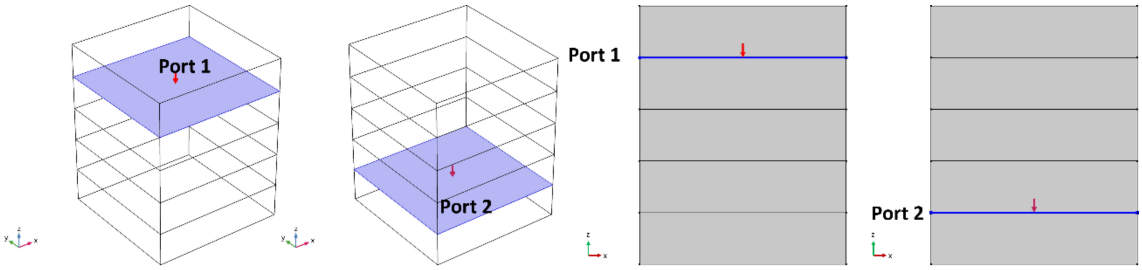

Figure 1.15 Example of using port boundary condition with COMSOL

4.1.2.3 Perfect Electric Conductor (PEC) Condition and Perfect Magnetic Conductor (PMC) Condition

The theory of PEC conditions and PMC conditions can be described below [113]:

For PEC: $\mathbf{n} \times \mathbf{E} = \mathbf{0}$

Which indicates the electric field perpendicular to this layer or boundary can be absorbed.

For PMC: $\mathbf{n} \times \mathbf{M} = \mathbf{0}$

Which indicates the magnetic field perpendicular to this layer or boundary can be absorbed.

PEC and PMC can be used together for the semi-infinite layer/domain, assume the electric field of incident light source is x direction, while the magnetic field is y direction. Therefore, PEC and PMC can be applied as following [18]:

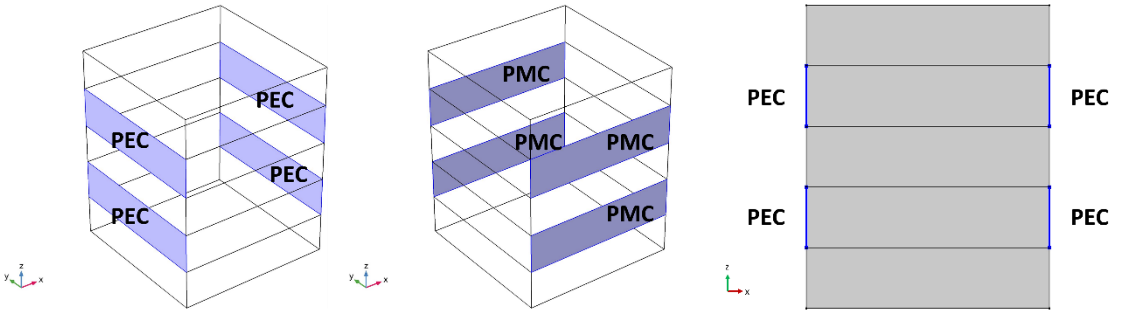

Figure 1.16 Example of using PEC and PMC with COMSOL

4.1.2.4 Periodic Boundary Condition and Transition Boundary Condition

PBC can be applied to the boundaries and layers that surround the filter structure, which repeats the block inside and can significantly reduce the computational time [113]. An example is shown below:

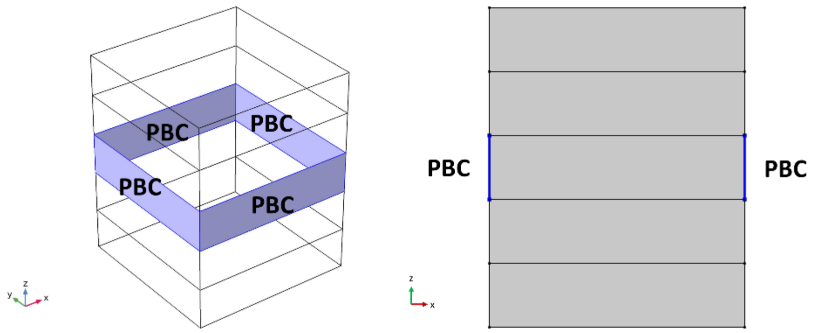

Figure 1.17 Example of using PBC with COMSOL

TBC can be used for the layers that are too thin in the whole geometric structure, such as the adhesion layer for the optical filter [113]. Moreover, the refractive index can also be set for this thin layer and no mesh will be required.

4.1.3 Mesh

Mesh is a very important part in the simulation software like COMSOL, which is based on the FEM. In 2D simulations, a triangular partitioning is typically as this guarantees full coverage of the simulated area without grossly overcomplicating the mesh. The exception is the PMLs, generally applied to the boundaries, for which a sweep mesh in rectangular shape is used. In 3D structures, the PBC layers are divided into triangular pieces, while the main structure (except PMLs) are divided into small tetrahedrons. The PMLs use a 3D sweep technique together with distribution function to mesh the layers between PML and main structure.

Lastly, the absolute value of the transmission efficiency is calculated by abs(emw.S21)^2 in the RF model (ewfd in wave optics model).

4.2 Nanofabrication Methods

This section will focus on those only nanofabrication techniques used in the projects demonstrated in this thesis

4.2.1 Lithographic Technology

There are various approaches to performing lithographic patterning on photo resist, such as creating the pattern on polymethyl methacrylate (PMMA) with HV electron beams (e.g. EBL). In this case, the sample will require development with MIBK diluted with IPA. It must be noted that EBL will have proximity effects. The electron beam can penetrate through the resist and make a pattern on it, but it will not stop by the resist, if the dose used is large, the electron beam would arrive and be reflected by the substrate (which relates to the material of substrate) and hit the resist again, which make the pattern become worse. Moreover, when the electron beam hit different resist, the resist would become different material after this chemical reaction. Thus, it needs developer to remove this new chemical resist and it becomes vacant. Therefore, a dose test, the developer concentration as well as developing time are essentially optimized [114-115].

Thermal scanning probe lithography (t-SPL) systems [116-117], such as the Nanofrazor [118], can directly write the pattern onto a resist such as polyphthalamide (PPA). The material is directly evaporated by an ultra-sharp heated scanning probe tip and therefore does not require high voltages. On the other hand, the system operates at high temperature, around 900°. Although in practice it has been found that the heat tends not to transfer through the PPA to the underlying surface. While directly patterning the resist does avoid the need for a development step, this is replaced by the requirement to remove the PPA residue, normally achieved using a process like deep reactive-ion etching (DRIE). The reaction that happens in the DRIE chamber is a chemical reaction in the presence of various single or mixed gas streams with plasma assist in which the etching rate can be controlled by varying the power and gas flow rate.

Focused ion beam (FIB) is also an important nanofabrication facility. FIB usually has two guns, one is used for imaging in the same way as SEM, while the other is used for milling the nanostructure in the sample with materials, such as gallium [119-120]. Although it has the advantage of being a maskless fabrication technique like EBL, some gallium residue may remain, causing contamination of the sample. Moreover, it also can cut the cross section and image the side of the sample.

4.2.2 Thin Film Deposition

Plasma-enhanced chemical vapour deposition (PECVD) is one of the best way to deposit amorphous (a-) material, such as a-SiO_2, a-Si_3N_4. The precursors mixed with a gas plasma would result in a very conformal deposition, which is more uniform and faster than sputter deposition and e-beam evaporator [121]. Moreover, a heater is available in most PECVD models that can help the material condense onto the sample. The sputter deposition uses a RF/AC/DC source to physically etch the material from the target with gas assistance and direct it to the sample [122]. An e-beam evaporator uses HV to mill the target material and evaporate it onto the sample, it is quite essential while performing nanofabrication with a lift off process.

4.2.3 Characteristics

Scanning electron microscope (SEM) is used for scanning samples with HV electron beams. The atoms within the sample will react with the electron beam to produce a signal to image sub-micron features of the sample. This microscopy function is critical to be able to determine if the various steps of patterning, etching and lift off have worked as required. However, the samples must be imaged in a vacuum chamber to avoid Contamination [123-124].

Atomic force microscopy (AFM) can also perform the sub-micron microscopy imaging. AFM operates in a similar way to t-SPL but has a read-out function only. It can work in an ambient environment, does not require a vacuum, and there is no need to fix the sample in position. It also does not suffer from diffraction limits [125]. The deposition thickness of thin film under different environment are not the same. For example, while using the sputter to deposit metal, it needs Argon gas to strike the plasma, and therefore the deposition pressure are different, resulting in a various deposition rate. The way to know the exact thickness is to use AFM to measure the sample. Furthermore, AFM also can be used to measure the roughness of the material surface, which has significant influence on the optical properties.

A final useful technique to investigate the sample properties is the ellipsometry, so-called because it measures the ellipse of polarization generated when a polarized light beam reflects obliquely from the surface a sample. As light reflected by different thin film will exhibit different phase information, ellipsometry uses light at varying angles to the sample to investigate optical properties such as refractive index [126]. For example, a material such as TiO_2 will exhibit different values of refractive index when deposited with or without oxygen assist, and ellipsometry can be used to find this slight difference within its diffraction limit and to assist researchers to figure out the reason.

Chapter 2 Transmission Enhancement in Coaxial Hole Array Based Plasmonic Color Filter for Image Sensor Applications

Plasmonic colour filters based on the hexagonal arrangement of coaxial hole array in aluminium have been demonstrated as a promising candidate for colour filter development due to polarization and incident angle insensitivity. They also comprise a single nanometer thick metal film, demonstrate good line width, CMOS compatibility and fine colour tunability. However, the low transmittance of the coaxial hole array based filters limits their use in potential applications such as image sensors and displays. This chapter introduces a new method to increase transmittance in coaxial hole array based filters by tuning localized surface plasmons and surface plasmon polaritons. In this method, coaxial holes of small diameters are filled along with a large size coaxial hole array to form a combined filter geometry with optimized parameters in aluminium film using computational techniques. The simulation results will have potential applications in CMOS image sensors, submicron pixel development, microdisplays and liquid crystal over silicon devices (LCoS).

Index Terms: Plasmonic colour filter, Coaxial hole array, Localized surface plasmon.

1. Introduction

As demand for high-resolution imagery continues to expand in consumer, scientific and industrial applications there is a need for smaller, highly tunable and robust colour filters [15, 92-93, 127]. Precise control of wavelength provides vivid colour response and improved selectivity. CMOS image sensor technologies have undergone enormous advances in recent years to increase performance and reduce pixel size. Along with reducing the transistor size to nanoscale for image sensors, submicron scale filters are also required to perform filtering for image acquisition sensors, next generation spatial light modulators [128-130] and high-resolution microdisplays.

Conventional colour filters are made from pigments and dyes. The filter colour response is directly related to the absorption coefficient, which in turn is related to the area/volume of the filters. Therefore, it is difficult to make nanometer-sized colour filters using pigments and dyes [12, 15, 18, 92-93, 127]. Recently, colour filters based on the titanium oxide nanodisk operating in reflection mode were reported as having good optical performance because of its low loss and high refractive index in the visible range [131]. However, this design is not suitable for image sensor applications due to their operation in reflection mode. Moreover, the titanium oxide nanodisk is not CMOS compatible. Plasmonic colour filters based on aluminium are better candidates to most of the all-dielectric colour filters due to their CMOS compatibility, ability to operate in transmission mode, use of single namometer thick film and excellent colour tunability (from UV to NIR range) [18-19, 92]. Furthermore, the filter spectral response can be carefully controlled by parameterising structure geometry, producing artificial material properties engineered to specific design and application requirements. There have been many demonstrations of colour filters employing plasmonic effects in the literature, especially using nanostructures in thin metal film [12, 15, 18-19, 22, 92-95, 103, 105, 109, 127, 132-143]. Such colour filters can be fabricated using a single perforated metal film with the thickness of 50 to 200nm. Despite these promising attributes, plasmonic filters still suffer from the poor transmission and incident angle sensitivity which have limited the scope of target applications and increased deployment requirements in

CMOS and display applications. For example, the peak transmittance wavelength for a simple hole array based plasmonic colour filters depends on the angle of the incident light because the surface plasmons based effect in the hole array is angle sensitive [18, 138]. If such a hole array filter were used in an image sensor, the filter will transmit only the desired colour at normal incidence while different colors would be filtered at oblique incidences.

Plasmonic colour filters based on the coaxial holes were reported using gold (Au) [105]. However, the coaxial hole array in Au film is limited to produce the resonance peak at wavelengths less than 480nm [105] due to the material limitation [109]. It has been demonstrated that transmittance of a square aperture array in the silver film can be enhanced using suitably placed small squares [140], however, the square aperture is polarization sensitive. Other designs were reported by creating symmetric patterns inserted into the metal film to increase the transmittance, such as the nano trench or cavity [141-142]. Extra coating on the Ag-Si film was also demonstrated to enhance the transmittance [143] based on the Fabry–Pérot resonances. However, these demonstrated structures are not covering full colours in the visible range, and Ag oxidizes in air. Au and Ag based filters are not CMOS compatible and also require a seed layer for better adhesion to substrates which increases the fabrication complexity.

Recently, it has been reported that vivid red, green and blue colours could be produced by plasmonic colour filters based on the hexagonal arrangement of coaxial holes in aluminium [19] and it is a promising candidate for image sensor applications, due to its angle insensitive and polarization independent characteristics. However, the transmittance of colour filters based on coaxial hole arrays is too low to be used in an image sensor or display as the transmittance reported in the literature varies from 5%

(red) to more than 20% (blue) [19]. This is because, for the localized surface plasmon, peak wavelength depends on gap size, thus as the gap decreases a shift towards the red region is introduced. Therefore, it is important to develop techniques to increase the transmittance of plasmonic colour filters without compromising important characteristics such as polarization and incident angle insensitivity, good line width, fine tuning capability and CMOS compatibility.

This chapter presents a technique to enhance transmittance of plasmonic colour filters based on the coaxial hole array in aluminium to overcome the limitation of low transmittance in the coaxial hole array filter using two different coaxial holes geometry that is independently tuned to the same colour (wavelength), followed by merging both the coaxial geometries to make a combined geometry.

2. Simulation Model and Optimization Method

The plasmonic resonance peaks responsible for obtaining different colours in a coaxial geometry are predominantly due to localized surface plasmons (Fabry–Pérot resonances) supported in a cylindrical resonance cavity. The cavity is excited by cylindrical surface plasmons formed by a metal film with finite thickness and two end faces. Tuning of colours was obtained by varying inner (r1) and outer (r2) radii of the coaxial hole using localized surface plasmons. The resonance peak (peak transmittance wavelength) can be obtained using different combinations of the inner (r1) and outer radii (r2)) as shown in Figure 2.1. The desired colour (transmittance peak) can be calculated using the equation $l = (n\pi - \Omega)/\beta$ [12, 18, 132], where l, n, Ω and β are the thickness of the metal film, the order of the Fabry-Pérot resonance, the phase of reflection constant and the propagation constant respectively. There is also a minor contribution to resonance peaks in the coaxial hole array geometry due to the pitch between coaxial holes caused by surface plasmons polaritons [19, 105].

The coaxial hole array in the hexagonal arrangement was simulated using a unit cell of a regular hexagon as shown in Figure 2.1a where W and L are defined as the separation between large coaxial holes in x and y directions respectively. The relationship between W and L are chosen such as $\mathrm{L} = 2 \times \mathrm{W} \times \frac{\sqrt{3}}{2} = \sqrt{3}\mathrm{W}$ for producing hexagonal geometry. To increase the transmittance, hexagonal geometry of large coaxial holes array (LCHA in blue regular hexagon block in Figure 2.1a is combined with an additional coaxial hole array with a smaller radius (SCHA in Figure 2.1b) to create a dual coaxial hole array (DCHA) in such a way that the combined geometry is polarization insensitive. In DCHA, the distance between two adjacent small coaxial holes is the same as the length d_1, the distance between the adjacent large coaxial hole and small coaxial hole. With the angle $\theta = 60^{\circ}$, as a result, $d_1= d_2= d_3= d_4= d_5=\frac{1}{3}\mathrm{L}=\frac{\sqrt{3}}{3}\mathrm{W}$ as shown in Figure 2.1c. The 3D geometries are computationally investigated using the finite element method (FEM) implemented in COMSOL MULTIPHYSICS. The simulation unit is highlighted by the red diamond block in Figure 2.1c and its top view is shown in Figure 2.1d. The simulation model consists of a 150nm thick layer of aluminium on a semi-infinite glass substrate (n=1.5) with 200nm thickness to find the wavelength at which maximum transmittance occurs for the filters. The top layer is air with a thickness of 200nm. Light is excited from the aluminium side (top side) using port boundary conditions. S-parameters are used to find the transmittance ($|S21|^2$) of the filters. Perfectly matched layer (PML) is used on the top and at the bottom of the model to avoid effects of reflected light in the transmittance spectrum.

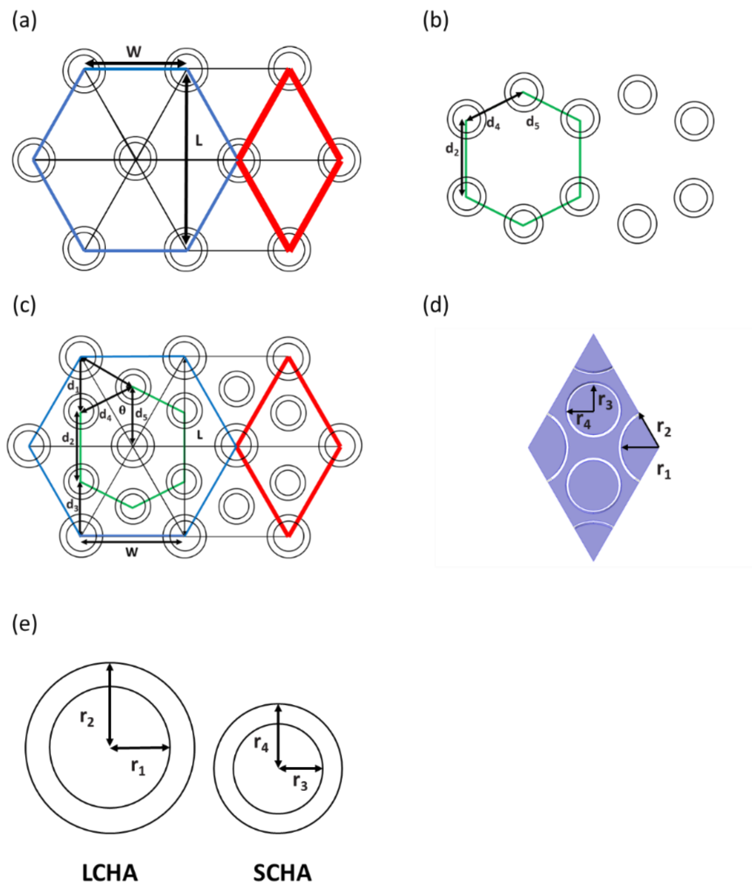

Figure 2.1 Schematic of (a) Large coaxial hole array (LCHA): Coaxial hole array showing a unit cell (red) used for simulation. Periodic boundary condition was used on four sides to simulate an array (b) Small coaxial hole array (SCHA) (c) Dual coaxial hole array (DCHA) made of a combination of large coaxial hole array (LCHA) and small coaxial hole array (SCHA) (d) Top view of DCHA unit cell (e) The radius of LCHA and SCHA.

Details of the incident wave are shown in Figure 2.2, and formula for electric field to study polarization and angle sensitivity is given below [144].

$$E_x = A\sin(\frac{\pi}{2} - \theta)\cos(\pi + \varphi)\, e^{-j(k_x \cdot x + k_y \cdot y + k_z \cdot z)},$$

$$E_y = A\sin(\frac{\pi}{2} - \theta)\sin(\pi + \varphi)\, e^{-j(k_x \cdot x + k_y \cdot y + k_z \cdot z)},$$

$$E_z = A\cos(\frac{\pi}{2} - \theta) e^{-j(k_x \cdot x + k_y \cdot y + k_z \cdot z)},$$

$$|E| = \sqrt{E_x{}^2 + E_y{}^2 + E_z{}^2} = A, k_x = k\sin\theta\cos\varphi, k_y = k\sin\theta\sin\varphi, k_z = k\cos\theta.$$

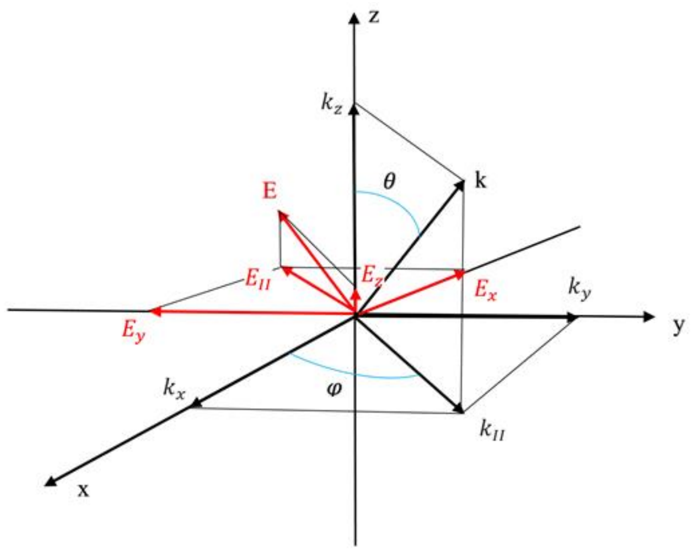

Figure 2.2 Schematic of incident plane wave: k is the propagation constant, θ is the angle of incidence and ϕ is the polarization angle.

The θ is the incident angle, φ is the polarization angle which is in the direction of $E_{//}$. Propagation constant k is defined as (2π×n)/λ where n is the refractive index of the simulation domain (air) where the port is set for illumination. The refractive indices of aluminium at different wavelengths are taken from Palik's experiment [145]. The incident angle θ was varied to study the effect of transmittance with respect to the angle of incidence. Similarly, polarization angle ϕ was varied to study polarization sensitivity.

3. Results

Based on the simulation models discussed above, in the first step, a large coaxial hole array is designed to produce the peak wavelength of 650nm (red colour filter) by tuning inner (r1) and outer (r2) radii to 120nm and 130nm, respectively by tuning the localized surface plasmons. This is followed by tuning the pitch to 420nm for $LCHA_R$ by tuning LSP. $LCHA_R$ gives a transmittance of 6.2% and a line width of 180nm (FWHM). In the second step, another small coaxial hole array is designed to the same peak wavelength of 650nm by tuning inner and outer radii to 83nm and 90nm, respectively ($SCHA_R$). $SCHA_R$ gives a 5.6% transmittance with FWHM of 150nm. In the final step, both $LCHA_R$ and $SCHA_R$ are combined to create the dual coaxial hole array ($DCHA_R$) with the enhanced transmittance of 15.5% with FWHM of 215nm. These results are presented in Figure 2.3. The insets of the Figure 2.3 show normalized electric field on $LCHA_R$, $SCHA_R$ and $DCHA_R$ which shows that both large and small coaxial hole arrays are excited by the incident light, and both are contributing to transmission. The increased transmittance is due to the coupling of plasmon resonances in both large and small coaxial holes constructively by geometrical tuning.

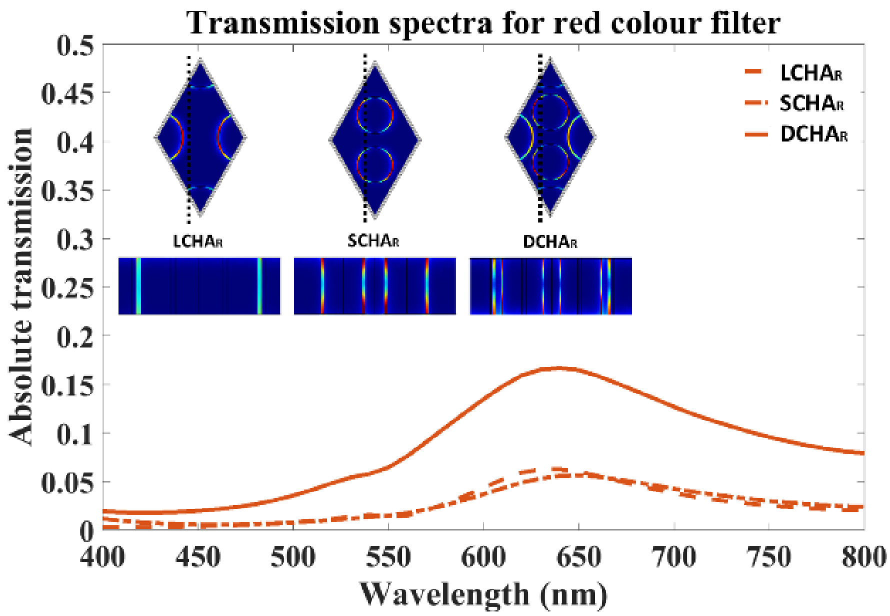

Figure 2.3 Simulation results of red colour filter: Transmission spectra of large coaxial hole array ($LCHA_R$), small coaxial hole array ($SCHA_R$) and dual coaxial hole array ($DCHA_R$). Subset images show normalized electric field from top view and lateral cross section along the dotted black line for $LCHA_R$, $SCHA_R$ and $DCHA_R$.

RGB colours are required for making the bayer pattern in CMOS image sensors. Hence the same scheme used for the red colour is applied for both green and blue colour filters. The blue colour ($LCHA_B$) is obtained by tuning the pitch size to 260nm, and radii to r_1=40nm and r_2=50nm. $LCHA_B$ is then combined with a small coaxial hole array tuned to the same wavelength ($SCHA_B$) with r_3=40nm, r_4=50nm to obtain $DCHA_B$. For the green colour ($LCHA_G$), pitch size is 430nm, r_1 and r_2 are 106nm and 130nm respectively. Then combining another smaller coaxial hole array ($SCHA_G$) with r_3=70nm, r_4=80nm for the green colour ($DCHA_G$).

The transmission spectra of blue and green colour filter for LCHA, SCHA and DCHA are shown in Figure 2.4 and Figure 2.5 respectively, and their line widths (FWHM) are tabulated in Table 2.1. The transmittance is increased more than 2x for red colour filter, 1.4x for green colour and 4x for blue colour. These results will have potential applications in developing micron and submicron colour filter development for CMOS sensors, micro-displays and spatial light modulators. CIE 1931 chromaticity diagram was plotted for red, green and blue colour filters using chromaticity coordinates obtained from simulation results for LCHA and DCHA (Figure 2.6). The CIE chromaticity chart shows that the pure colour perceived by human vision is obtained from the spectrum of different colour filters. From the CIE chromaticity charts of LCHA and DCHA, it is shown that the measured chromaticity coordinates of the RGB filters falls around the achromatic point. For the green and red DCHA colour filters, their positions are slightly shifted on the CIE chart towards the center (white light) compared to SCHA. But the shift is still falling around the achromatic point and is within the acceptable limit. In terms of colour reconstructions, SCHA will perform better than DCHA as it covers a larger range in the CIE chart. As a result, more colours can be reconstructed for SCHA. This effect is due to a slight increase in FWHM after combining LCHA and SCHA. This demonstrates the capability of DCHA based colour filters with increased transmittance for a large degree of colour range tuning applications such as CMOS image sensors.

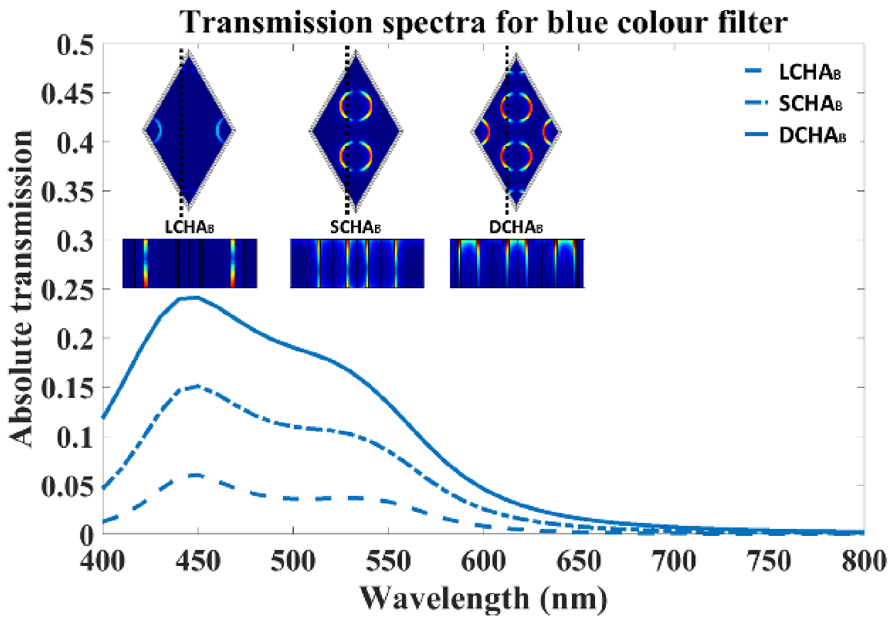

Figure 2.4 Simulation results of blue colour filter: Transmission spectra of large coaxial hole array ($LCHA_B$), small coaxial hole array ($SCHA_B$) and dual coaxial hole array ($DCHA_B$). Subset images show normalized electric field from top view and lateral cross section along the dotted black line for $LCHA_B$, $SCHA_B$ and $DCHA_B$.

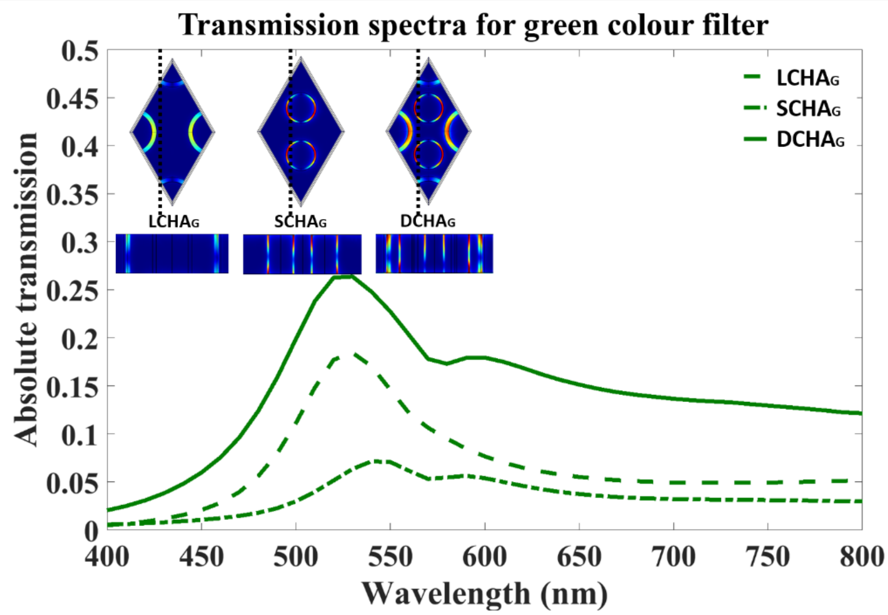

Figure 2.5 Simulation results of green colour filter: Transmission spectra of large coaxial hole array ($LCHA_G$), small coaxial hole array ($SCHA_G$) and dual coaxial hole array ($DCHA_G$). Subset images show normalized electric field from top view and lateral cross section along the dotted black line for LCHA, SCHA and DCHA.

Table 2.1 Maximum transmittance, peak wavelength and FWHM for LCHA, SCHA and DCHA of blue, green and red colour filter.

Colour	Model	Maximum transmittance	Peak wavelength	FWHM
Blue	$LCHA_B$	6.0%	450nm	140nm
	$SCHA_B$	15.0%	450nm	150nm
	$DCHA_B$	24%	450nm	150nm
Green	$LCHA_G$	18.4%	530nm	120nm
	$SCHA_G$	7.1%	530nm	180nm
	$DCHA_G$	26.4%	530nm	200nm
Red	$LCHA_R$	6.2%	650nm	180nm
	$SCHA_R$	5.6%	650nm	150nm
	$DCHA_R$	15.5%	650nm	215nm

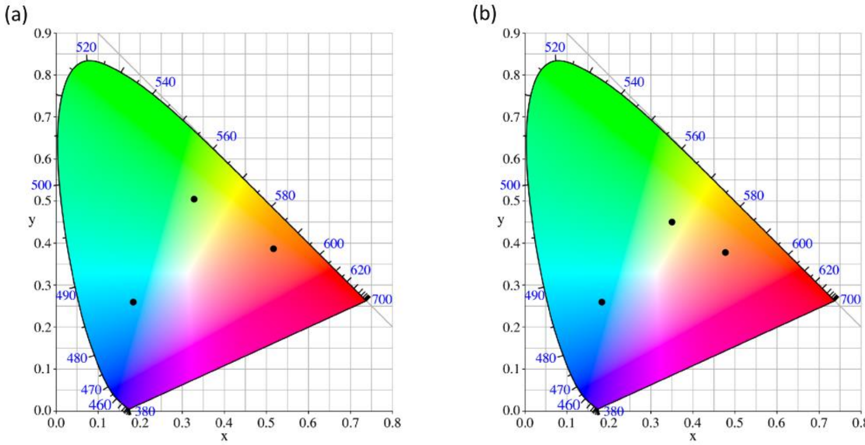

Figure 2.6 CIE chromaticity chart of blue, green and red colour filter for (a) LCHA, and (b) DCHA.

There are two important requirements for a colour filter to be used in CMOS image sensors, viz polarization insensitivity and angle independence. The polarization insensitivity ensures capturing the exact colour and intensity of objects irrespective of the rotation of camera/sensor. Angle independence is essential to obtain the same colour of objects irrespective of the angle of recording. For example, if the filters are angle sensitive, the same object will be recorded with different colours at different angles of the image capture. The transmittance of DCHA is studied for three different polarization angles, 0°, 45° and 90°. A red DCHA colour filter ($DCHA_R$) is taken as an example as shown in Figure 2.7a. The results show the DCHA is almost polarization insensitive. Furthermore, transmission characteristics of the red colour DCHA are studied for different incident angles (full field angle: FFOV), 0°, 30° and 60°, as shown in Figure 2.7b. There is no shift in the peak wavelength with respect to angle, and hence the transmitted colour will be the same from different angles of illumination with a small reduction in the intensity (~ 3.5%). These results show that DCHA design is very promising for colour filter development due to angle insensitivity, polarization insensitivity, good line width (FWHM), fine tuning ability and CMOS compatibility.

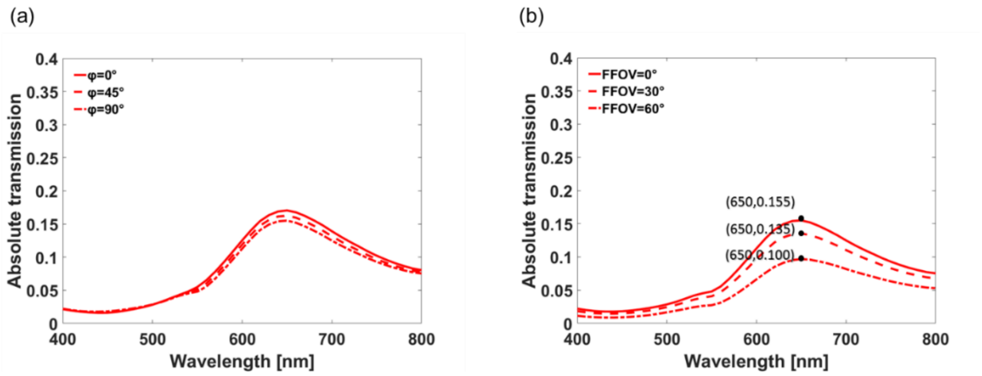

Figure 2.7 Simulation results of transmission spectrum of DCHA for different polarizations and angle of excitations (a) the polarization angles ϕ=0°, ϕ=45°, ϕ=90° and corresponding transmission spectra showing DCHA is polarization insensitive (b) angle dependence of DCHA shows no shift in peak wavelength with respect to angle and variation in transmittance is negligible. Here, the angle of incidence (excitation) represented as full field of view (full angle), FFOV= 0°, 30°, 60°.

4. Conclusion

This chapter presents a technique to increase peak transmittance of the hexagonal arrangement of coaxial hole array in aluminium without compromising its polarization insensitivity, line width and angle insensitivity. In the proposed technique, one large coaxial hole array is designed for a peak wavelength of interest after optimization, followed by designing a small coaxial hole array to the same peak wavelength. These two coaxial hole arrays are then combined in a suitable fashion to enhance the transmittance. The transmittance is increased more than 2x for red colour filter, 1.4x for green colour and 4x for blue colour, which are generally larger than 15%, and from the CIE chart, even though their positions are a bit closer to the center, vivid colours can still be presented. These results will have potential applications in developing micron and submicron colour filter development for CMOS sensors, micro-displays and spatial light modulators. However, making the pattern with feature size around 10nm in the coaxial hole array through 150nm Al film is quite difficult even with recent advanced nanofabrication facilities, such as FIB or EBL.

Chapter 3 A CMY Camera using Nanorod Filter Mosaic Integrated on a CMOS Image Sensor

CMY colour camera is different from the RGB counterpart where the subtractive colours cyan, magenta and yellow are used. CMY camera performs better than RGB camera in low light conditions. However, conventional CMY colour filter technology made of pigments and dyes are limited in performance for the next generation image sensors with submicron pixel sizes. This is because the conventional CMY filters cannot be fabricated in nanoscale as they use their absorption properties to subtract colours. The chapter presents a CMY camera developed using nanoscale CMY colour filter mosaic size of 4 mm x 4mm with each filter colour size of 4.4 µm made of Al-TiO_2-Al nanorods integrated on a MT9P031 CMOS image sensor. The colour imaging is demonstrated using a 12 colour Macbeth chart. The developed technology will have applications in astronomy, low exposure time imaging in biology and photography.

1. Introduction

In a conventional CMOS based image sensor, colour imaging relies on the integration of filters on top of the photodetector array. These filters typically cover the three primary colours (bands), red (around 650 nm), green (550 nm) and blue (450 nm) (RGB), predominately in a Bayer pattern [15, 17-19, 91-93, 127, 139, 146-148]. As the human eye is more sensitive to green light than either red or blue, the widely used Bayer filter mosaic is formed with twice as many green as red or blue filters. RGB colour space uses an additive colour mixing of red, green and blue that combine to create a white output.

In contrast, CMY (cyan, magenta and yellow) is a subtractive colour mixing scheme where colour filters are used to remove certain wavelengths of white light. For example, cyan is obtained when the red is subtracted from an image. Similarly, magenta and yellow are obtained by subtracting the green and blue respectively. In RGB space, a red filter transmits only about 1/3 of the visible light as the remaining light is absorbed in the filter (only the red light passes through the filter). But the counterpart cyan filter in CMY colour space transmits about 2/3 of the spectrum because only the red is subtracted and the remaining is transmitted through the filter. In general, CMY colour filters pass approximately twice the spectral power as a corresponding RGB filters [47] and so are promising candidates for low-light imaging applications. Examples include astronomical imaging, of nebula and the like, that are characterized by weak images against a dark background. Furthermore, more images are required to be captured in short exposure time in astronomy for imaging objects before rotation effects blur the image (example, Jupiter) and this requires high transmission filter schemes such as CMY. Conventional CMY colour filters are made of organic dye-based materials or pigments. They use their absorption properties to subtract selected wavelengths. However, as the pixel size in the image sensor is reduced to a submicrons, the conventional CMY colour filters start to suffer from colour cross talk as they will not be able to operate in nanoscale thickness [15, 17-18, 91-93, 127, 139, 146-147]. Furthermore, the existing CMY technology must be fabricated in several steps, which presents severe challenges when trying to accomplish submicron scale alignment. These demand the development of new CMY colour filter technologies.

Colour filters based on plasmonic effects [15, 17-19, 21-22, 45, 87, 91-93, 100, 102, 127, 133, 139, 146-155] are suitable for CMY colour filter development due to their precise colour tuning using nanoscale thick film. Colour filters based on localized surface plasmons are superior to the filters based on surface plasmons as the former is angle independent. The angle independency of LSP based filters make the transmitted colours same for any angle of excitation and this is an important requirement for image sensor applications. Recently gold (Au) nano-disk based CMY filters have been demonstrated with good characteristics such as polarization independence and angle insensitivity [102]. However, Au based plasmonic colour filters are limited in colour tuning, especially below 550 nm as Au does not readily support plasmonic resonance peaks below 550nm [109]. CMY filters based on silver (Ag) nanoslit [22] and nano-disk [100] are reported with high transmission coefficient. But Ag oxidizes quickly in air and degrades the optical properties without extra coating that can affect the filter characteristics. Al is well known for its CMOS compatibility. Furthermore, there will be a thin Al_2O_3 layer formation on the surface of Al, different from Ag, and this layer will prevent Al being further oxidized. The CMY colour filters operating in reflection based on the surface plasmon polaritons (SPP) are demonstrated in [151-154], but the reflection mode is not suitable for image sensor applications. To date, there have been no demonstration of developing a CMY filter mosaics and their integration on image sensors to make a CMY camera for imaging applications and this is the first such demonstration.

This chapter presents a nanoscale thick CMY colour filter built from a hexagonal array of Al-TiO_2-Al nanorods on a quartz substrate that is derived from a subtractive MDM (metal-dielectric-metal) nanohole array structure. The structure exhibits a high transmission efficiency and narrow bandwidth to produce a superior colour separation. The colour tuning is achieved by varying rod radius across the nanorod array, while keeping the base thickness constant, thereby making a mosaic of CMY filters across the substrate. An optical filter mosaic of size 4mm x 4mm was integrated onto a monochrome image sensor (MT9P031) to make a CMY camera, followed by demonstrating its imaging capabilities using the 12 colour Macbeth chart.

2. Results

2.1 Filter Design

Figure 3.1a shows the proposed structure of a CMY colour filter. The colour filters are made of Al-TiO_2-Al nanorods fabricated on a quartz substrate and then embedded in SOG (spin on glass [156]) matrix for the refractive index matching.

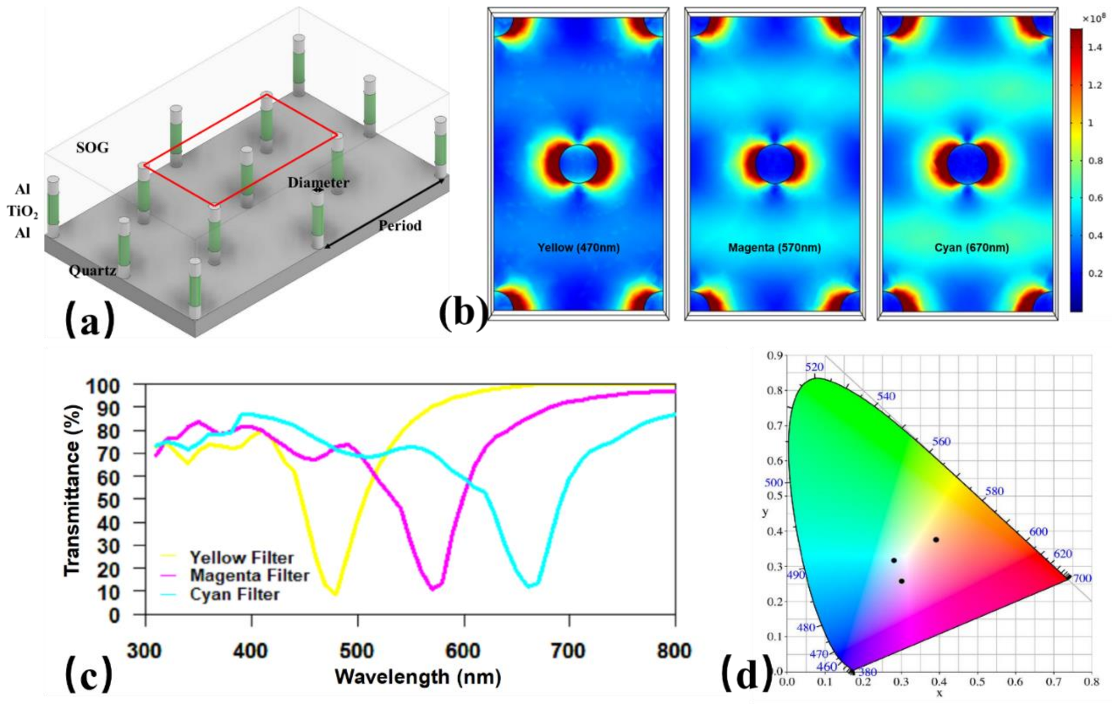

Figure 3.1 Simulation results of Al-TiO_2-Al nanorod based CMY (cyan, magenta, yellow) colour filter mosaic: (a) Al-TiO_2-Al nanorods in hexagonal array on a quartz substrate covered with spin-on-glass, (b) The normalized electric field at valley wavelength for the filters, yellow (470 nm), magenta (570 nm) and cyan (670 nm) Electric field at 470nm, (c) Numerically simulated transmission spectra of the CMY colour filters . The

wavelength is swept from 300 nm to 800 nm (d) CIE chart of simulated CMY colours in the filter mosaic.

The optical characteristics of this structure arise from a Fano resonance in which the top and bottom metal disk operate together as a coupled dipole and hence enhancing the magnetic field between them to produce both destructive and constructive (i.e., in-phase and anti-phase) interference modes. Choosing an appropriate radius and period for the structures results in a narrow reflection peak and a deep transmission valley that are sensitive to the symmetry of the dipole elements [157]. It has been shown in previous work related to nanodisks [155, 157] that these structures exhibit a broad (in-phase) resonance at smaller wavelengths and a narrow anti-phase resonance at larger wavelengths. This can be described in terms of a Q factor, which is proportional to the ratio of the resonant frequency to the FWHM. It is also clear that, while introducing asymmetries can strengthen the peaks (in particular, the anti-phase resonance), it introduces an undesirable sensitivity to the angle of incidence [157]. As a result, our work has kept the thickness and radius of both the top and bottom metal disks the same. This also has the added advantage of simplifying its fabrication.

The CMY filters were computationally investigated using the finite element method (FEM) implemented in COMSOL MULTIPHYSICS. The simulation model consists of a unit cell on a semi-infinite thick quartz substrate consisting of a single nanorod at the centre and one-quarter of nanorod at each corner as shown in Figure 3.1a. The simulation unit on the semi-infinite glass substrate is covered with spin on glass. Furthermore, the perfect matched layer (PML) is applied on the top and at the bottom, periodic boundary conditions are applied on the four side of the simulation unit as highlighted in red block

(Figure 3.1a.) For calculating the peak wavelengths, the refractive index of glass is taken as 1.5, spin of glass 1.45 and the wavelength dependent refractive index of Al from Rakic's data [158]. TiO_2 was deposited with E-beam evaporator and the refractive index experimentally measured as 2.1. This value is used in the simulation model. The simulated transmission spectrum for CMY colour filters are shown in Figure 3.1c. The normalised electric field of each colour filter, yellow (470 nm), magenta (570 nm) and cyan (670 nm) at their resonant wavelength (valley wavelength) is shown in Figure 3.1b. The layer thickness, period and rod diameter are summarised in Table 3.1. Figure 3.1d shows that the CIE chromaticity chart of the simulated CMY colour filters values are falling in the appropriate part of the colour space and their suitability for the imaging applications.

Table 3.1 Parameter of Al-TiO_2-Al nanorod.

	Cyan	Magenta	Yellow
Top Al thickness	40nm	40nm	40nm
TiO_2 thickness	90nm	90nm	90nm
Bottom Al thickness	40nm	40nm	40nm
Period	500nm	430nm	350nm
Diameter	60nm	50nm	40nm

2.2 Fabrication Method

A 4 mm x 4 mm size CMY colour mosaic was fabricated with an arrangement of CMYM colour unit repeating in both horizotal and vertical directions to get an array, on a quartz substrate. The fabrication strategy using a PMMA-MMA bilayer is shown in Figure 3.2. Firstly, a 1mm thick quartz substrate was cleaned with acetone under sonication for 5minutes followed by IPA and DI water rinse. Then the substrate was preheated on a heater under 80degree for 10minutes and then a thin EL9 (MMA) layer was spin coated on the quartz at 3000rpm for 1.5minutes and baked under 180degree heater for 15minutes. Next a thin PMMA A2 layer was spin coated onto the sample at 3000rpm for 1.5minutes and baked at 180degree for 5 minutes. Due to the charging problem of quartz substrate with electron beam lithography (EBL), a 30nm Cr layer was deposited on the sample by conformal sputtering to finish the sample preparation. After patterning with EBL (Vistec EBPG5000plusES), the Cr layer was removed using 1 minute in Cr etchant, stopped by 5% H_2SO_4. The sample was then developed with diluted MIBK (MIBK:IPA=1:3) for 1 minute and stopped by IPA and DI water. After development, various shapes in PMMA and MMA are shown in Figure 3.2. The bowl shape in the MMA, for example, will make the later lift off easier due to the smaller contact area between the Al-TiO_2-Al nanorod and quartz. Lastly, the Al-TiO_2-Al nanorod was deposited by E-beam evaporator (Intlvac Nanochrome II), note that the deposition rate of TiO_2 is 0.1nm/s. After the lift off, the CMYM colour filter was completed after being spin coated with SOG (Desert NDG-2000) at 2000rpm for 20second and baked at 210 degree for 15minutes.

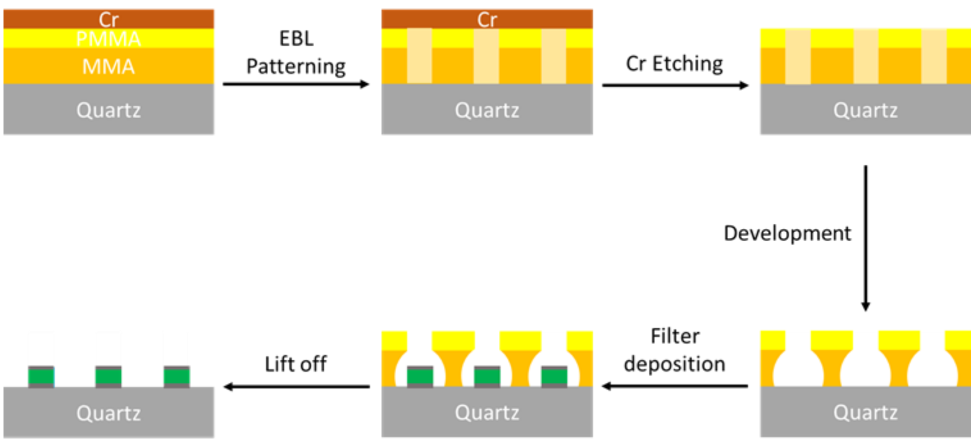

Figure 3.2 Fabrication strategy for making Al-TiO_2-Al nanorod based CMY colour filter mosaic

Figure 3.3d shows optical images of the CMYM filter mosaic in transmission mode under an optical microscope (Olympus BX53M) with 20×magnification. An enlarged CMYM is shown in Figure 3.3e. The SEM image of the filter mosaic (cyan) from the top view is shown in Figure 3.3f. Figure 3.3g shows in reflection mode that the reflected light from the sample (Figure 3.3e) is RGB colour. The transmission spectrum from the fabricated CMY colour mosaic was measured using a CRAIC spectrometer (Apollo Raman™ Microspectrometer) as shown in Figure 3.3h. From the spectrum measurement, it can be seen the maximum transmission of Cyan, Magenta and Yellow colour filter could be 90%. The transmission spectrum displayed high transmission without any secondary resonance from UV to Near-IR wavelength. Figure 3.3i shows the experiemtally measured CIE chromaticity chart of the CMY colour filters. And the detailed results are collated in Table 3.2.

Table 3.2 Optical characteristics of the CMY filter mosaic.

	Cyan		Magenta		Yellow	
	Simulation	Experiment	Simulation	Experiment	Simulation	Experiment
Valley wavelength (nm)	660	670	580	580	470	480
Maximum transmission contrast (%)	60	45	70	47	80	50
Maximum transmission efficiency (%)	90	90	100	92	100	90

From Figure 3.3h, the valley wavelength in the simulation is almost constant with that in the experiments. It could be seen the maximum transmission contrast is reduced, which also happened in the other experiments [155]. This difference may be caused by the rough surface while depositing TiO_2, to keep a more pure metal oxide property that give us a relatively high refractive index, the deposition rate with E-beam evaporator needs to be as high as possible, which results in a rough surface (around 3-5nm measured by Atomic Force Microscopy). Therefore, the top Al disk becomes rough as well. However, the maximum transmission efficiency in the experimental measurement is nearly the same as simulation result, which could give us a large optical intensity, and the influence with the smaller transmission contrast to the colour imaging applications is considered minimum. Furthermore, the contrast can be corrected in the image processing part.

2.3 Filter Integration and Image Reconstruction

The CMYM mosaic was integrated on a CMOS sensor using flip-chip bonder (Fineplacer @Lambda) and captured raw images for further analysis. The CMOS image sensor used in this experiment is a monochrome sensor MT9P031 with pixel size 2.2µm. Figure 3.3a shows that CMY colour filter mosaic is aligned and glued on the image sensor, the glue is homemade with PMMA powder diluted with anisole solution. The high transmission efficiency of the CMY colour filter is demonstrated using the University logo on the white paper that could be seen through filter clearly (Figure 3.4). The whole filter mosaic size is 4mm x 4mm, each colour filter covers 2 by 2 pixels to increase the light absorption and decrease the spatial crosstalk. Therefore, the filter colour pixel size is 4.4µm. The image sensor integrated with the mosaic is then fitted with an optics with *f* number of 1.4 for imaging as shown in Figure 3.3b. The compact size of the CMY camera is shown with respect to a coin in Figure 3.3c.

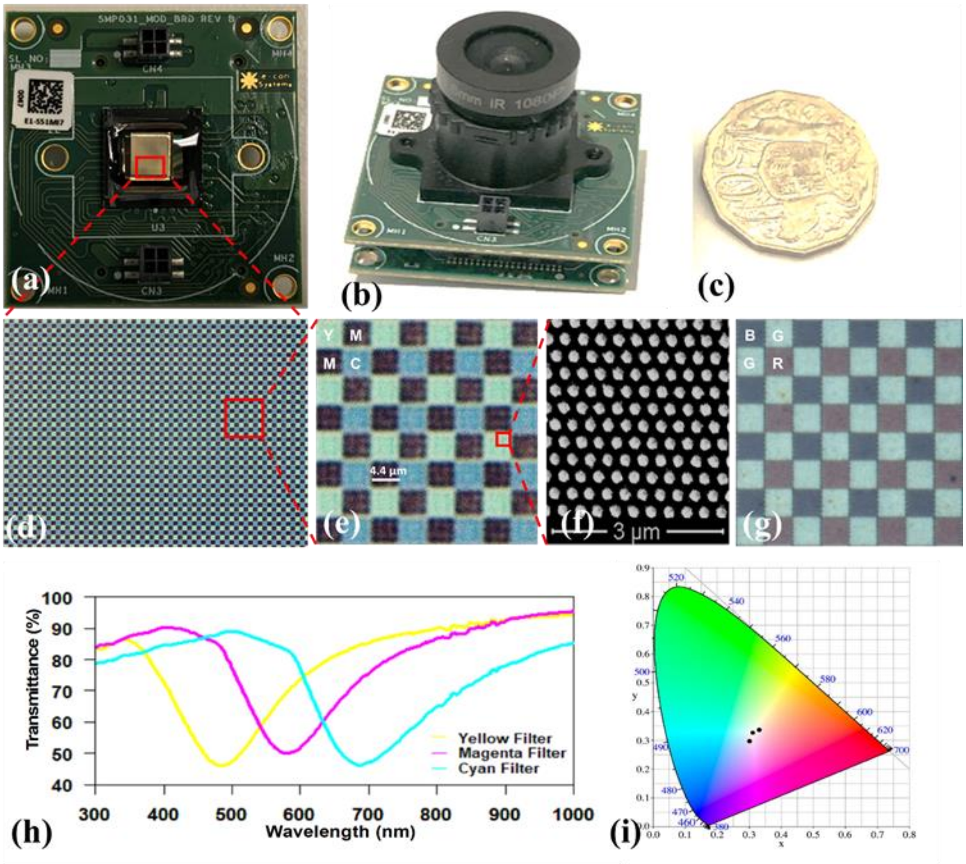

Figure 3.3 Integration of the CMY colour mosaic on the image sensor. (a) CMOS image sensor, MT9P031 integrated with 4mm x 4mm CMY colour mosaic using flip chip bonder for alignment (b) CMY camra developed with optics (*f* number 1.4) for imaging (c) a coin as a reference to show the compact size of the CMY camera (d) the CMY colour mosaic under optical microscope magnification ×20 (e) magnification ×40. (f) SEM image of the filter mosaic made of Al-TiO_2-Al nanorods from top view (cyan is shown) (g) Reflected RGB colours from Figure 3.3e (h) Experimental transmission spectra of the CMY color filters from the color mosaic (i) CIE chromaticity chart of the CMY filters in the mosaic from experimental data.

Figure 3.4 The fabricated CMY filter mosaic on the quartz substrate was cut into 4 mm x 4 mm using a dicing saw. The University of Melbourne logo on the white paper that could be seen through the filter clearly. This demonstrate the high transmission of the filter mosaic for the image sensor applications.

This CMY camera is then used for the colour imaging applications shown in Figure 3.5. Firstly, a raw image of the standard 12-colour Macbeth chart was taken with CMY camera (Figure 3.5a). The recorded 12-bit raw image data was then transmitted to a laptop for image processing using MATLAB. The raw data was analysed for saturation and signal intensity variation. Figure 3.5f shows a plot of the signals from the 12-colour Macbeth chart pixels across the transect indicated by the red dashed. The results show that the pixel intensity variations are captured in the CMY raw image. Then each colour pixels was picked up to form three different images for cyan, magenta and yellow (Figure 3.5b). Figure 3.5c shows the reconstructed CMY colour image. Next, a CMY to RGB conversion algorithm was applied to change the CMY image to standard RGB image: R=Y+M-C, G=Y+C-M, B=C+Y-M [148]. Lastly, the colour correction and white balance were applied to recover the Macbeth chart as shown in Figure 3.5e. Here colour balance and vibrance functiond in the photoshop software were used for the colour correction and the white balance. The results obtained demonstrates that colours can be retrieved from the 12-bit raw image data and working of the CMY camera. Due to the colours of fabricated filter is more close to the center in the CIE chart, the recovered colour intensity variation is not very evident. This causes missing colours in the recovered Macbeth chart.

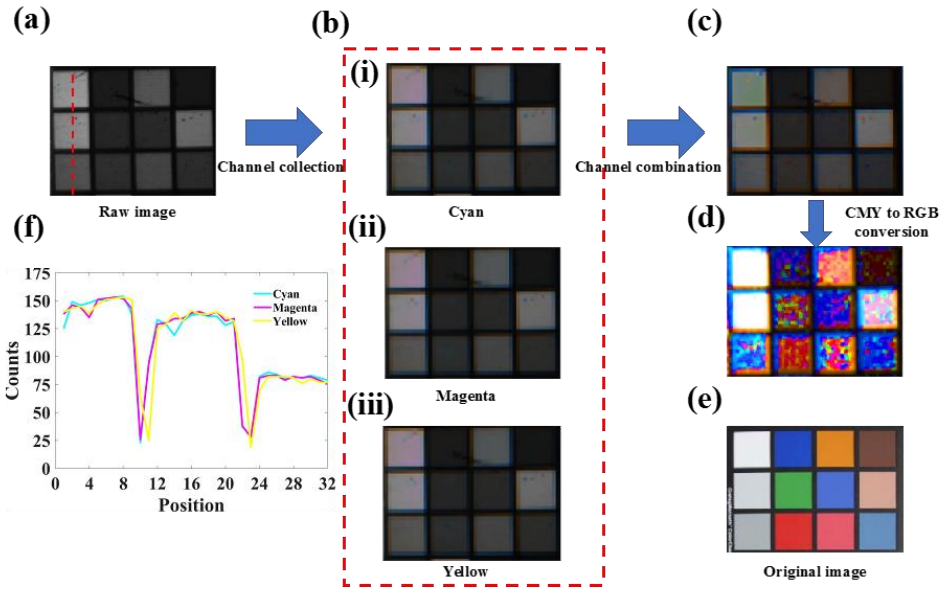

Figure 3.5 Demonstration of colour imaging by the CMY camera: (a) 12-bit raw image of the 12 colour Macbeth chart captured by CMY camera (b) Three bands (cyan, magenta and yellow) extracted from the raw image (c) The three bands (three channel combination) are recombined to get a CMY color image (d) The CMY colour image is converted into RGB and applied color correction and white balance (e) Standard image of the 12 colour Macbeth colorchart (f) The plot shows signals from three pixel numbers along the vertical red dotted line in the raw image.

3. Conclusion

In conclusion, a CMY camera is demonstrated using polarization independent nanoscale CMY colour filter mosaic made of Al-TiO_2-Al nanorods with high transmission. The filter mosaic size of 4 mm x 4mm with each filter colour size 4.4 µm in CMYM combination is integrated on a MT9P031 CMOS image sensor using flip-chip bonder and in-house prepared glue. The filter mosaic was characterised for its performance. The CMY camera was then characterized using a 12 colour Macbeth chart as an object and colours were retrieved using image processing algorithms. Use of more powerful image processing algorithms (used in commercial camera) will improve the colour performance. The presented technology will overcome the limitations imposed by conventional colour filter technology for making next generation submicron pixels based CMY colour image sensors and cameras. Furthermore, the developed technology will have applications in astronomy, low exposure time imaging in biology and photography. However, more advanced image processing algorithm for CMY filter should be focused for the future development. The processing for RGB camera and CMY camera is very different, there exists several algorithms for CMY to RGB conversion developed by image processing engineers. But with this kind of research based CMY camera, a customized algorithm should be developed.

Chapter 4 A Single Sensor Based Multispectral Imaging Camera using a Narrow Spectral Band Colour Mosaic Integrated on the Monochrome CMOS Image Sensor

A multispectral image camera captures image data within specific wavelength ranges in narrow wavelength bands across the electromagnetic spectrum. Images from a multispectral camera can extract additional information that the human eye or a normal camera fails to capture and thus may have important applications in precision agriculture, forestry, medicine and object identification. Conventional multispectral cameras are made up of multiple image sensors each fitted with a narrow passband wavelength filter and optics, which makes them heavy, bulky, power hungry and very expensive. The multiple optics also create image co-registration problem. This chapter demonstrates a single sensor based three band multispectral camera using a narrow spectral band RGB colour mosaic in a Bayer pattern integrated on a monochrome CMOS sensor. The narrow band colour mosaic is made of a hybrid combination of plasmonic colour filters and heterostructured dielectric multilayer. The demonstrated camera technology has reduced cost, weight, size and power by almost n times (where n is the number of bands) compared to a conventional multispectral camera.

1. Introduction

In a conventional CMOS based image sensor, colour imaging relies on the integration of filters on top of the photodetector array [14, 16, 159-161]. These filters typically cover the three primary colours (bands), red, green and blue (RGB), predominately in a Bayer pattern [18, 26, 102, 162]. As the human eye is more sensitive to green light than either red or blue, the widely used Bayer filter mosaic is formed from alternating rows of red-green and green-blue filters with twice as many green as red or blue filters. Three different materials are used for producing the primary colours with wide spectral bands (spectral width of around 90-100 nm) for all wavelengths [18, 26]. Multispectral cameras extend this concept to capture images with multiple colour bands and with narrow pass bands (i.e., narrow spectral widths) [80, 106, 163]. Images from a multispectral camera can extract significant amount of additional information that the human eye or a normal camera fails to capture and thus have important applications in precision agriculture, forestry, medicine, object identifications and classifications [25, 28, 80, 107, 163-164]. Conventional multispectral cameras are made up of multiple CMOS sensors each externally fitted with a narrow passband wavelength filter. For example, three bands would require three image sensors with associated electronics, three narrow bandpass filters and three optics. Depending on the application, the spectral width measured at the FWHM (Full Width Half Maximum) of a multispectral imaging camera varies between 10 nm and 90 nm [80, 107, 163]. Figure 4.1 and Table 4.1 show comparison between a conventional multispectral camera with six bands and a single sensor based multispectral camera. The need for multiple sensors for each band results in a number of problems. Firstly, it means that multispectral cameras tend to be bulky and power hungry, which in turn limits their wider deployment in portable applications such as drone-based precision agriculture or for hand- held and portable uses such as wound monitoring, vein detection and skin screening [25, 28, 164]. It also greatly complicates the task of optical alignment which ensures that precisely the same scene is captured across all bands. Further, image co-registration problems will emerge from a slight mismatch between images in each band, which will require complex image processing to correct [37, 165]. The above problems can be eliminated if a multispectral camera is developed using one single image sensor. This has prompted research in developing single sensor based multispectral cameras [41-42].

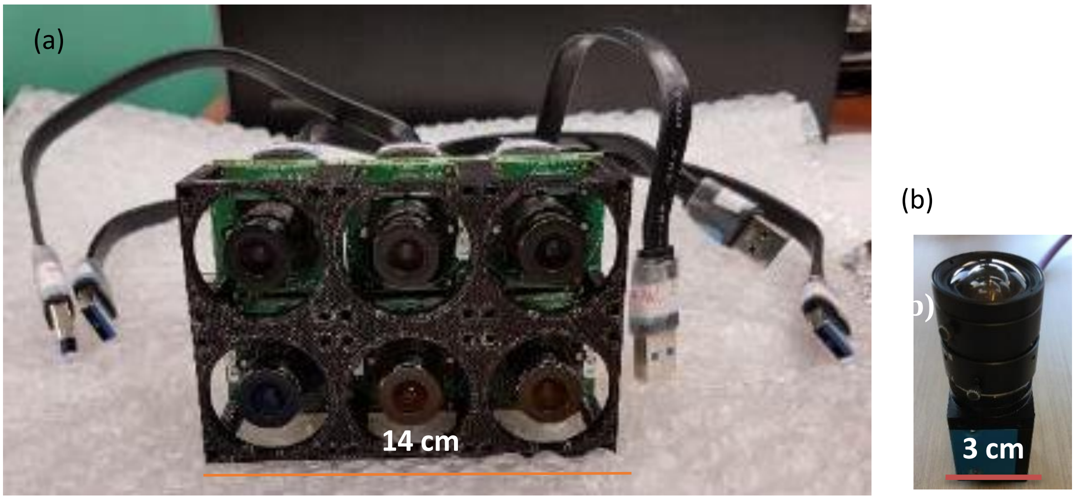

Figure 4.1 Comparison between *a conventional multispectral camera* and single sensor based multispectral camera (a) A compact conventional multispectral camera developed at Electrical and Electronic Engineering, the University of Melbourne. The sensor has 6 different cameras, 6 bandpass filters, 6 processing electronics, 6 optics and bulky connectors (b) *Single sensor based multispectral camera* developed by authors with the flexibility to integrate 3 to 6 bands.

Table 4.1 Comparison between commercially available conventional multispectral cameras and the proposed single sensor based multispectral camera

Parameters	Commercially available conventional multispectral cameras	Single sensor based multispectral camera
Size (L x W x D)	180mm x 65mm x 35 mm	43mm x 29mm x 62mm
Weight	520g	130g
Power Consumption	Around 8W	Around 1.25W
Image Co-registration problem	Yes	No

Conventional pigments and dye-based filters are not suitable for making narrow band filters mosaic because their spectral widths tend to be too large (90-180nm) and hence preventing the use of a normal colour camera for multispectral imaging applications [21, 80]. Furthermore, these pigments tend also to be sensitive to UV radiation, degrade at high temperatures and are not particularly environmentally friendly.

Conventional technology for making a single narrow bandpass filter requires deposition of several layers of different dielectric materials (for example, 40 layers [63]) with precise thickness. Here, for making each narrow colour band requires different thickness combinations for these 40 layers. For example, three narrow colour bands require three different filters with each colour band repeated thousands of time to form a filters mosaic on a CMOS sensor using the conventional technology for getting an image. This will require thousands of steps for laying down thin films of precise thickness for each band separately with multiple complex masking and alignment processes with a large failure rate that significantly increases manufacturing costs and complexity [21]. As a result, it is extremely difficult to develop a low cost colour mosaic with narrow pass bands integrated onto the pixels of a CMOS chip.

Advancement in nanofabrication has enabled fabrication of novel nanophotonic devices including colour filters [17-18, 166-169]. Plasmonic colour filters with different geometries have proven their ability to tune the wavelength from UV to NIR range [17, 19, 22-23, 44-45, 88-90, 92-93, 100, 105, 127, 132-134, 136, 170-174]. Furthermore, plasmonic filters are shown to be suitable for developing one single narrow band filter in the visible wavelengths [88-89] and short wavelength infrared (SWIR) [23]. In these filters, spectral FWHM values of 30nm (visible) and 80nm (SWIR) were achieved in selected wavelengths. However, these filter technologies are not suitable for fabricating a narrow filters mosaic (consists of multiple narrow colour bands next to each other) on a single substrate for multispectral imaging due to their complex architecture such as requirement of different film thicknesses values for each band. 1D metal grating filters has been explored with an aim to reduce the spectral width of plasmonic colour filters. In 1D metal grating filters, the plasmons are excited through an interface between the metal and dielectric [23, 88-90]. A spectral width of 64 nm was demonstrated using a 1D metal grating filter made of silver nanoslit array fabricated on a glass substrate [48]. In addition, a 1D metal grating filter based on Al nanoslit integrated onto a thick Al2O3 buffer layer has been demonstrated with spectral widths of 20nm [90]. However, it has been proved both theoretically and experimentally [22, 84] that 1D metal grating filters are polarization dependent and can produce colours only under transverse magnetic (TM) illumination. 2D metal grating filter and dielectric guided mode resonance (GMR) filters are reported to bypass the polarization effects [75-77, 169]. A hexagonal hole array inserted in a metal-dielectric-metal multilayer has been reported to slightly reduce the spectral width [21]. Overall, it appears that most of the narrow-band spectral filters reported are unsuited for use in multispectral image sensors for a range of reasons, including the inability to achieve a narrow spectral width over a wide range of wavelengths, fabrication complexity to achieve narrow multi-band filters mosaic, polarization sensitivity and the requirement for TM illumination in the case of 1D metal grating filters.

The single sensor-based multispectral camera is using a hybrid narrow spectral band RGB colour mosaic fabricated on a quartz substrate and then integrated on a monochrome CMOS image sensor. The presented filter mosaic can be easily tuned to any wavelength and requires only one processing stage to derive multiple bands. The filter mosaic consists of a hybrid combination of a double sandwich of silicon nitride-silica-silicon nitride layers (heterostructured dielectric multilayer) covered by a hole array patterned in CMOS compatible aluminium (the plasmonic filter). The heterostructured dielectric multilayer is a common base layer for all the bands and the thickness values were optimized to reduce the spectral width in a given wavelength range of interest. A single layer of plasmonic filter is used for wavelength tuning. The mosaic on quartz is then integrated onto a monochrome CMOS image chip (Sony) using a flip-chip bonder resulting in a 3 cm x 3 cm size, three-bands single-sensor based multispectral image camera. The performance of the camera is first demonstrated using a standard Macbeth Chart. It is then fitted onto a lightweight DJI Phantom 3 drone to demonstrate its imaging capabilities in the field and for making handheld sensors. Because only a single camera chip is required, weight, power and complexity can be reduced by a factor of n, where n is the number of bands compared to the conventional approach using multiple cameras.

2. Results

2.1 Design and Optimization of the Hybrid Colour Mosaic

The RGB hybrid filter mosaic was designed and optimized by 3D simulation within the finite element based COMSOL Multiphysics® package. Each filter geometry was investigated separately using a 10nm wavelength step size. Figure 4.2a shows 3D simulation model of the colour mosaic with 6 layers. The basic unit cell for this simulation encompassed the diamond shaped pattern of holes highlighted in red in the top of Figure 4.2a. The simulation model, Figure 4.2a consisted of a 150 nm thick layer of aluminium patterned with a hexagonal arrangement of holes (the plasmonic filter: 1 layer) over repeating layers of Si_3N_4 - SiO_2 – Si_3N_4 (heterostructured dielectric multilayer: 5 layers), deposited on a semi-infinite glass substrate (n=1.5). A 200nm layer of Spin-On-Glass (SOG) was assumed to cover the aluminium layer for index matching and to avoid any shorting with metallic pads on CMOS chip while integration. Finally, a perfectly matched layer (PML) was used at the top and bottom of the model to avoid the effects of reflected light in the transmittance spectrum and periodic boundary conditions were applied to the four sides to allow a large area to be simulated without costing excessive memory and time.

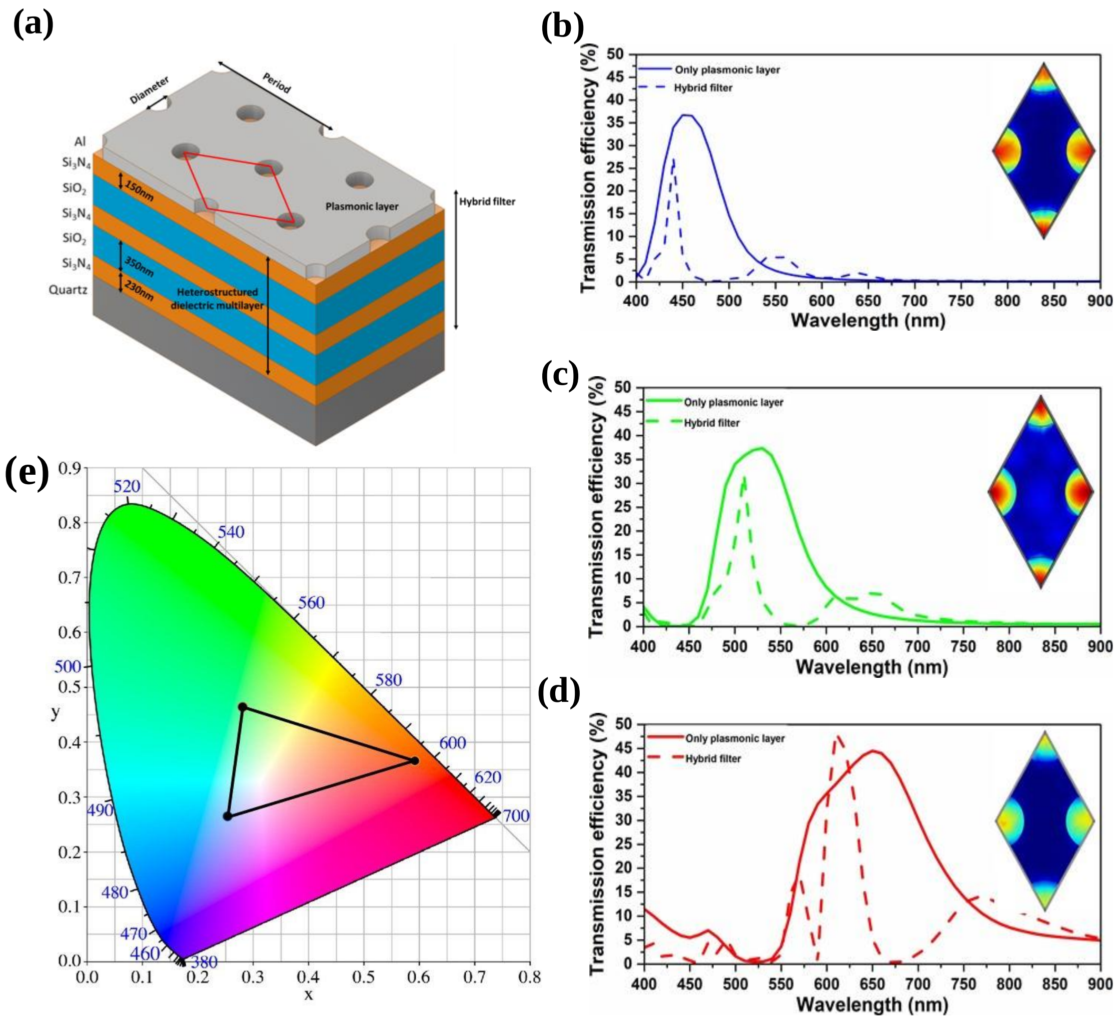

Figure 4.2 (a) 3D simulation model of hybrid filter in the colour mosaic. The hybrid filters consist of 6 layers made of double Si_3N_4 (230 nm) - SiO_2 (350 nm) - Si_3N_4 (230 nm) sandwich layers that forms a common base multilayer structure (heterostructured dielectric multilayer: 5 layers) and a 150 nm thick aluminium perforated with hexagonal arrangement of holes (plasmonic layer:1 layer). (b) Numerically simulated transmission spectra of the blue plasmonic layer and blue hybrid filter showing the reduction in spectral width. The wavelength was swept from 400 nm to 900 nm. The spectral width at full width at half maximum (FWHM) of the hybrid blue filter was reduced to 17 nm from 70 nm produced by the plasmonic aluminum layer. Subset image shows normalized electric field at the peak wavelength of 440 nm (c) The

spectral width (FWHM) of hybrid green filter was reduced to 30 nm from 95 nm produced by the plasmonic layer. Subset shows normalized electric field at the peak wavelength of 530 nm (d) The spectral width (FWHM) of the hybrid red filter was reduced to 35 nm from 160 nm produced by the plasmonic layer. Subset shows normalized electric field at the peak wavelength of 625 nm (e) CIE chromaticity chart of simulated blue, green and red hybrid colour filters in the mosaic.

The pitch and hole diameters were varied to obtain peak transmission at 440 nm, 530 nm and 625 nm [93] using the plasmonic layer. The objective was then to determine and validate the wavelength at which maximum transmittance occurs for these filters. Light was excited from the aluminium side (top side) using port boundary conditions and S-parameters used to find the transmittance (|S21|2) of the filters. As in [156], refractive index values of 1.42 and 1.5 were used for the SOG layer and quartz substrate, respectively. A Filmetrics Model F20 was used to experimentally determine a refractive index for SiO_2 of 1.45 and around 1.9 for the Si_3N_4 and then used in the simulations. As shown in Figure 4.1b - d, the plasmonic layer has produced the required transmission peak (colour), but with large spectral width of 70 nm, 95 nm and 160 nm for blue, green and red respectively.

The plasmonic layer was then combined with a heterostructured dielectric multilayer with 5 layers made of double Si_3N_4 (230 nm) - SiO_2 (350 nm) - Si_3N_4 (230 nm) sandwich layers to form the hybrid filter with optimized thickness values to reduce the spectral width. Here the photonic crystal theory is applied, layer 1 has the refractive index n_1 and thickness l_1 and its adjacent layer 2 with n_2 and l_2, then when $l_1n_1=l_2n_2$, the gap size will be maximized and therefore the incident light will produce a very narrow spectrum.

Such an effect can be used to create narrow bandpass optical filters. The sharp peaks in the transmission spectrum as shown in Figure 4.3 help to further narrows down the peak spectral width of the filters.

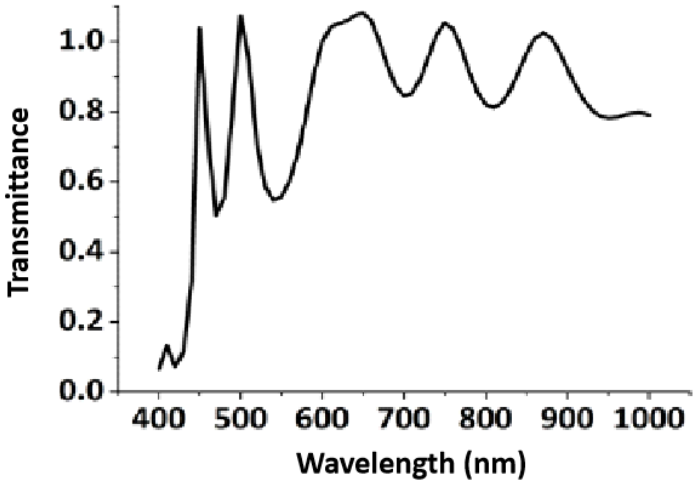

Figure 4.3 Transmission spectrum of heterostructured dielectric multilayer.

The heterostructured dielectric multilayer with a constant thickness values form a common base layer for all RGB bands in the filter mosaic. In the hybrid filter, one single plasmonic layer has removed most of the spectral contents on either side of the peak transmission wavelength in a given range of wavelengths. This has significantly reduced the requirement of large number of layers in the multilayer to produce narrow bands. Figure 4.2b - d shows the simulated spectra of the red, green and blue filters in the mosaic from 400nm to 900 nm along with the electric field distributions at peak wavelengths. Here, the thickness of the Si_3N_4 - SiO_2 - Si_3N_4 base layer and the plasmonic layer (Al) are kept constant and the pitch (period) and diameter of the holes in the 150 nm aluminium plasmonic layer varied to tune the red, green and blue filters. The optimized hybrid filter mosaic parameters are given in the Table 4.2.

Table 4.2 Optimized thickness Parameters of the hybrid filters in the mosaic from computational simulation with COMSOL Multiphysics® 5.2, the filter characteristics in the mosaic from simulations and experiments.

Parameters (nm)		Red – 620nm	Green – 520nm	Blue – 440nm
Common base structure: Thickness kept constant	Si_3N_4 (layer 1)	230	230	230
	SiO_2 (layer 2)	350	350	350
	Si_3N_4 (layer 3)	230	230	230
	SiO_2 (layer 4)	350	350	350
	Si_3N_4 (layer 5)	230	230	230
	Aluminium (layer 6)	150	150	150
Pitch		420	340	290
Hole Diameter		240	180	150
Simulated FWHM		35	30	17
Experimental measured FWHM		45	60	60

The FWHM of the hybrid red filter was reduced to 35nm from this simulated spectrum. For the green and blue filters, the FWHM was reduced to 30nm and 17nm respectively. Furthermore, this topology has considerably reduced the fabrication complexity as the thickness of the layers can be kept constant when fabricating the narrow band mosaic, and wavelength tuning can achieved by varying the pitch of the holes in the top single nanoscale thick plasmonic layer. The resonance peak shift with respect to different angle of incidence (0 – 80 degrees field of veiw, FOV) was estimated for the hybrid filter (green hybrid filter was taken as an example) as shown in Figure 4.4. The resonance peak position remains almost constant irrespective of the angle of incidence with slight decrease in the transmission intensity. This FOV is in the acceptable limit with suitable optics attached to the multispectral camera.

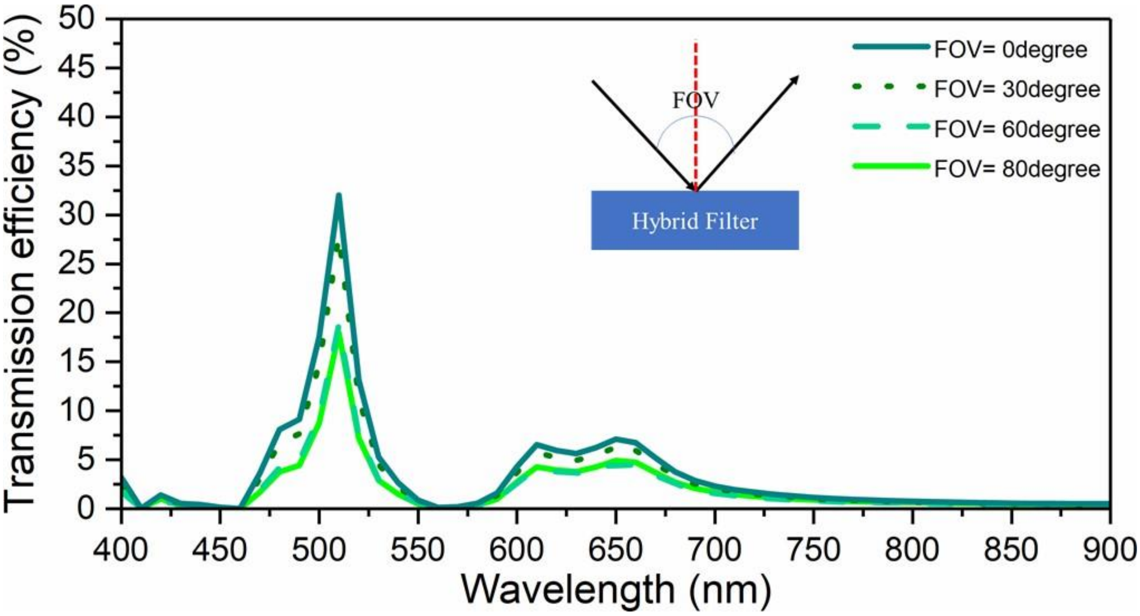

Figure 4.4 Angle dependence of the hybrid filters. The green hybrid filter is taken as an example. The angle was varied from 0 to 80 degrees FOV. The resonance peak position remains almost constant irrespective of the angle of incidence with slight decrease in the transmission intensity which is in the acceptable limit with suitable optics attached to the multispectral camera.

2.2 Fabrication of the Hybrid Colour Mosaic

The hybrid filter mosaic was fabricated on a 4-inch quartz wafer. The fabrication process is shown in Figure 4.5. Firstly, the wafer was cleaned using Acetone and IPA (Isopropyl alcohol) with ultrasonic agitation followed by 2 minutes of plasma pre-cleaning. The wafer was then deposited with a-Si_3N_4 and a-SiO_2 by Plasma enhanced CVD (Oxford Instruments PLASMALAB 100 PECVD). The circular 4-inch wafer was diced into 2 cm x 2 cm square pieces and the centre pieces were selected for further fabrication due to their uniformity of Si_3N_4 and SiO_2 film thicknesses. The measured refractive index of Si_3N_4 and SiO_2 developed by PECVD were 1.9 and 1.45, respectively. The deposition rates were optimized and approximately 23nm/min (10% tolerance) and 70nm/min with the composition shown in Table 4.3.

Table 4.3 Recipe of Si_3N_4 and SiO_2 deposition with PECVD.

	RF Forward Power (W)	Chamber Pressure (mT)	Temperature (°C Celsius)	5% SiH_4 and 95% Argon (Sccm)	NH_3 (Sccm)	N_2O (Sccm)	Depositing Rate (nm/min)
Si_3N_4	20	1000	250	40	200	0	23
SiO_2	20	1000	250	150	0	800	70

The thickness of Si_3N_4 was optimized to be 230nm and the SiO_2 to 350nm. Starting with Si_3N_4, a total of five layers of Si_3N_4 and SiO_2 were deposited on the quartz wafer. After fabricating the multilayer structure, a 150 nm thick aluminium layer was deposited on the top of the structure using an E-beam evaporator (Intlvac Nanochrome II) at a constant rate of 0.2Å/Sec. An ellipsometer was used to measure the refractive index of the aluminium and the result showed it fits Rakić's experiment [158]. These data were subsequently used in the simulation model. A metallic nanohole array comprising varying pitch and hole diameters was fabricated on the aluminium film using EBL lithography process and deep reactive ion etching using the optimized values from simulations (Table 4.2). A thin ZEP 520A resist was spin coated on the device at 1500rpm for 1.5 minutes, followed by 5 minutes baking at 180°C. The pattern was exposed by EBL (Vistec EBPG5000plusES) with 1.5nA current and 400um aperture for 4 hours. The sample was then developed in n-Amyl acetate for a minute followed by a rinse with IPA and DI water. The exposed pattern was etched by deep reactive-ion etching (DRIE Oxford Instruments PLASMALAB100 ICP380) at 40°C with forward power of 1000W and 20sccm Cl_2 under 2mT chamber pressure for 40 seconds to form the holes. ZEP resist was then removed by DRIE at 40°C with a forward power of 1000W and 50sccm O_2. Finally, the Spin-On-Glass [156] was spin coated on the top surface at 4000rpm for 20 seconds, followed by baking on a hotplate at 210°C for 10 minutes.

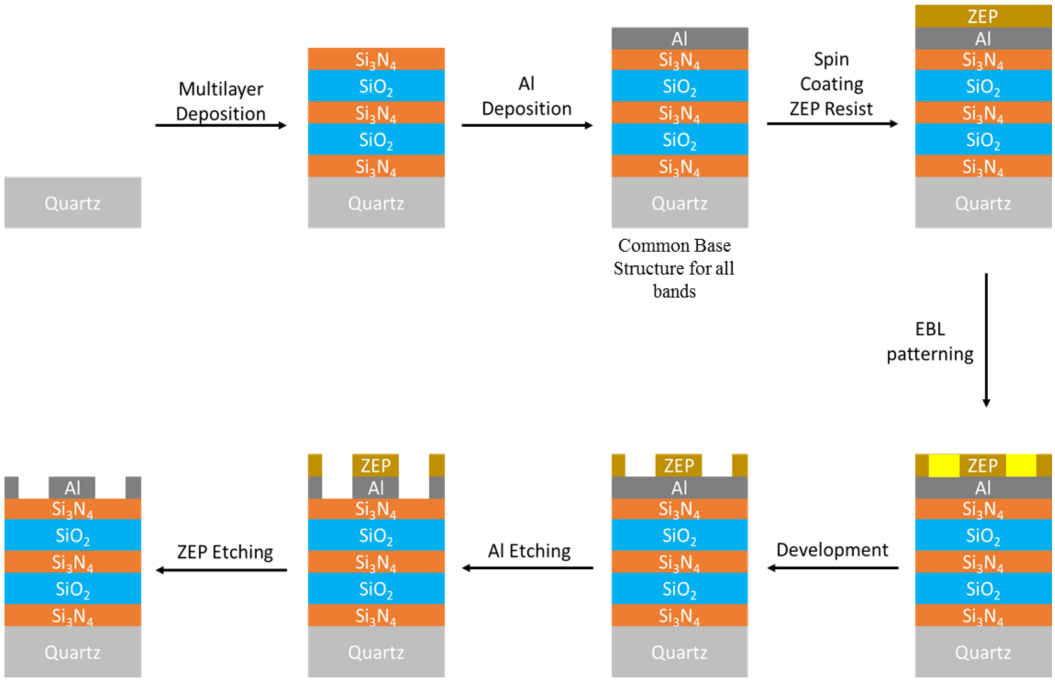

Figure 4.5 Fabrication process for our proposed narrow band filters mosaic with common base.

2.3 Spectrum Measurement and Discussion.

The fabricated hybrid colour filter on the quartz substrate was cut into 2×2 mm^2 squares using a dicing saw. The dicing step is carried out using G1A flange blade, and is optimized with hairline alignment. This alignment can adjust the cut on the substrate to the center of the hairline to precisely dice the edge with minimal edge damage. Hence, the dicing has not affected optical performances of the sensor. Figure 4.6a shows optical images of the RGB filter mosaic in transmission mode under an optical microscope (Olympus BX53M) with 40× magnification. SEM image of a section of the hybrid filter mosaic from top view is shown in Figure 4.6b. One unit size of the hybrid RGBG mosaic is 11.2 µm×11.2 µm. The spectra of the hybrid RGB filters were measured using a CRAIC spectrometer (Apollo Raman™ Microspectrometer) and CytoViva Hyperspectral Imaging in transmission mode. Figure 4.6c shows the RGB spectrum from 400nm to 900nm. The spectral sensitivity (responsivity) of most commercial image sensors working in the visible and near-IR have different sensitivity with respect to wavelengths (Figure 4.7). Hence the experimentally measured spectra of the RBG was multiplied with responsivity versus wavelength for the image sensor to get the actual spectra as shown in Figure 4.7b.

Figure 4.6f shows the CIE chromaticity chart overlaid with the transmission data, demonstrating that the RGB filter values are falling in the appropriate part of the colour space. There is a small shift of green towards yellow due to a minor secondary peak in the green transmission spectrum. However, this small shift in the green coordinate is still falling around the achromatic point and is within acceptable limits. The experimental transmission efficiency for RGB filters in the mosaic is around 10 %. The low transmission efficiency is compensated by making each filter band of size 11.2 um covering 2 by 2 pixels (one pixel size: 5.6 um) to increase the light absorption by the photodetectors and hence to increases the signal content. Further compensation can be achieved by increasing exposure time of the image sensor in low light conditions while capturing the images. The FWHM of the red filter in the mosaic has the best performance with a width of around 45nm, while the blue and green filters exhibit FWHM values of 60nm and 60nm, respectively.

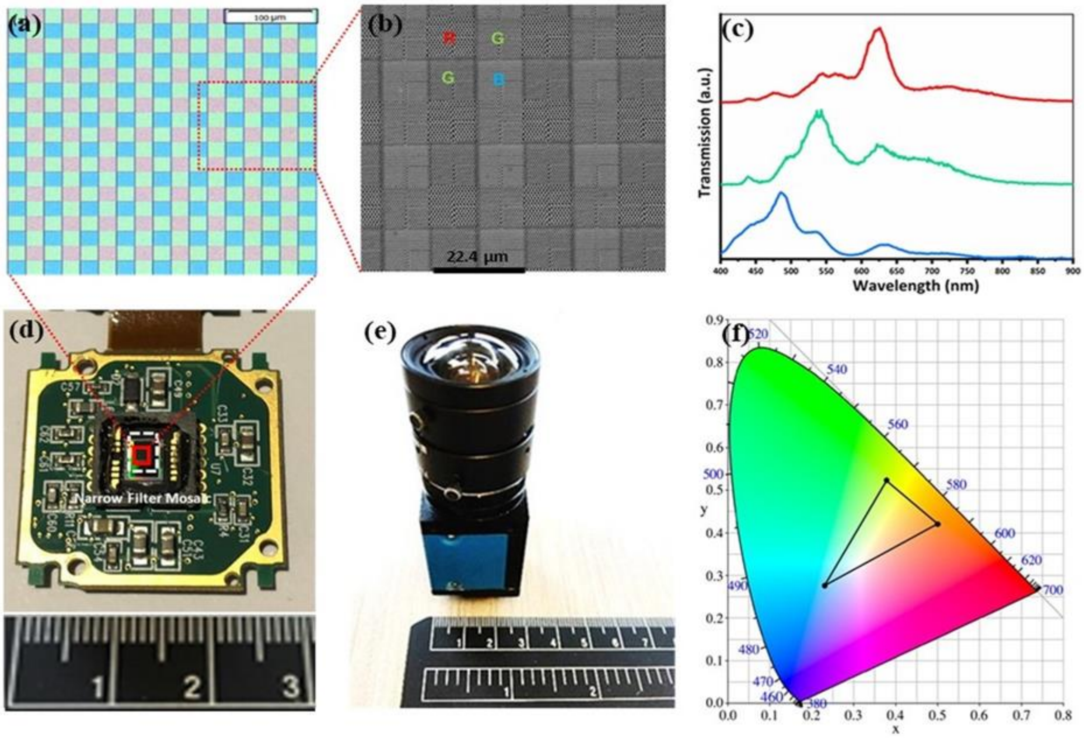

Figure 4.6 Integration of the hybrid narrow spectral band mosaic on the image sensor (a) Image of the colour mosaic under optical microscope in transmission mode with magnification × 40 (b) SEM image of a section of the hybrid mosaic from top view. One narrow band RGBG unit size is 11.2 µm×11.2 µm (c) Experimental transmission spectra of the narrow spectral band red, blue and green (RGB) colour filters from the colour mosaic. The spectral widths (FWHM) of RGB are 45 nm, 60nm and 60 nm, respectively (d) The colour mosaic integrated on SONY ICX618 sensor pixels using a flip chip bonder for alignment (size 3 cm× 3 cm) (e) The single sensor based multispectral camera. The mosaic integrated image sensor fitted with housing and optics with *f* number 1.4 for multispectral imaging (f) CIE chromaticity chart of the hybrid narrow band blue, green and red colour filters in the colour mosaic from experimental spectra.

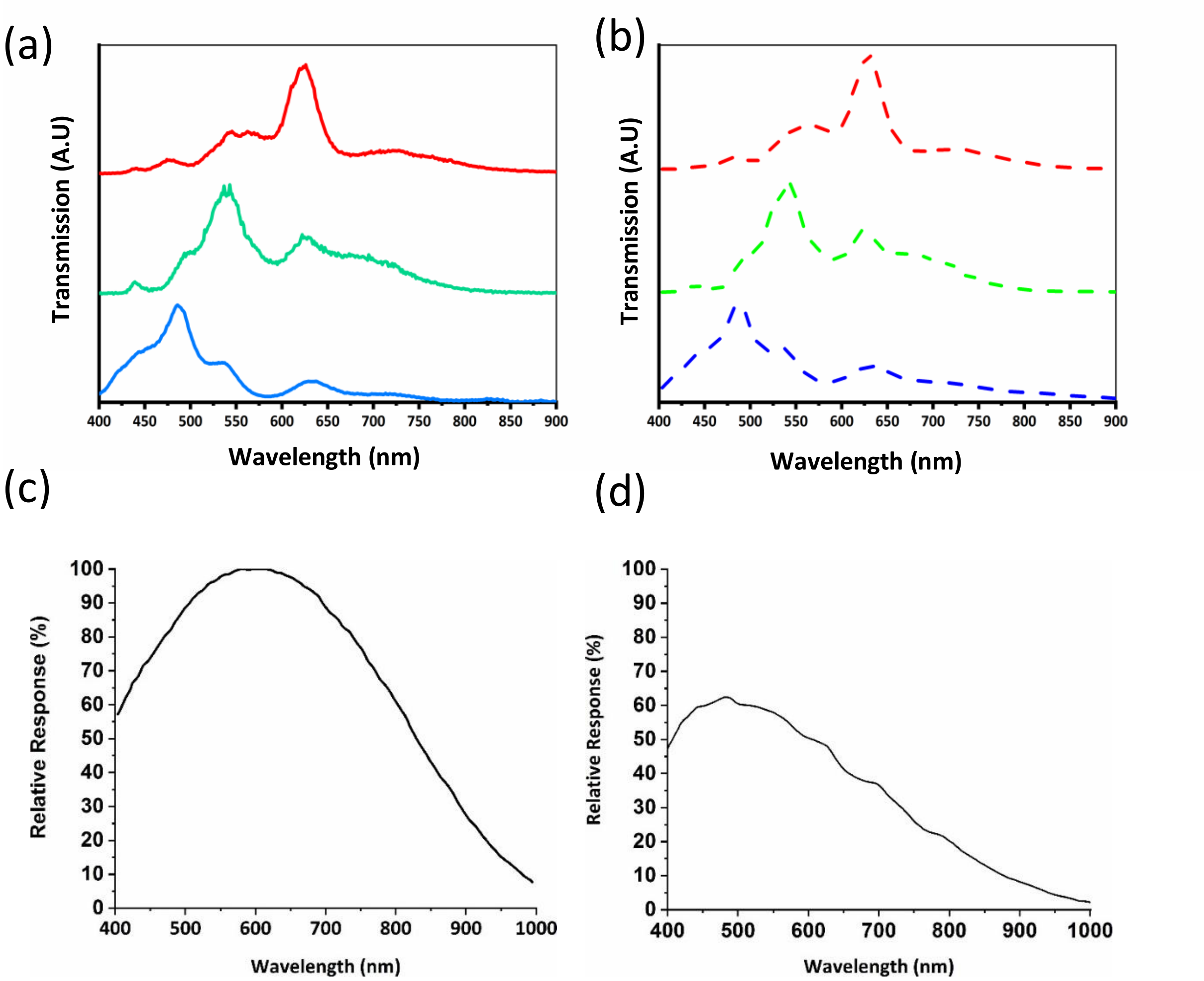

Figure 4.7 (a) Experimental transmission spectra of the narrow spectral band red, blue and green (RGB) colour filters from the colour mosaic. The spectral widths of RGB are 45 nm, 60nm and 60 nm, respectively (b) The relative transmission spectrum after multiplying with image sensor response with respect to wavelength (c) responsivity versus wavelength of ICX618 (d) responsivity versus wavelength of MT9P031.

The measured FWHM values are slightly wider than the results obtained from computer simulations for two primary reasons. Firstly, variations in the deposition rate of Si_3N_4 and the fact that SiO_2 growth using PECVD has larger tolerances than in the E-beam evaporator. While a high temperature (250°C) during the deposition of Si_3N_4 and SiO_2

results in a good quality of dielectric, it restricts the available methods for verifying the exact deposition thickness to the Filmetrics software sensor system in the PECVD, which is less accurate than AFM. Secondly, as shown in the SEM image in Figure 4.8, the pitch and the hole shape in the plasmonic layer can vary due to fabrication tolerances (such as minor under cut in holes and nanoscale thickness variations) from the ideal (simulated) case shown in Figure below:

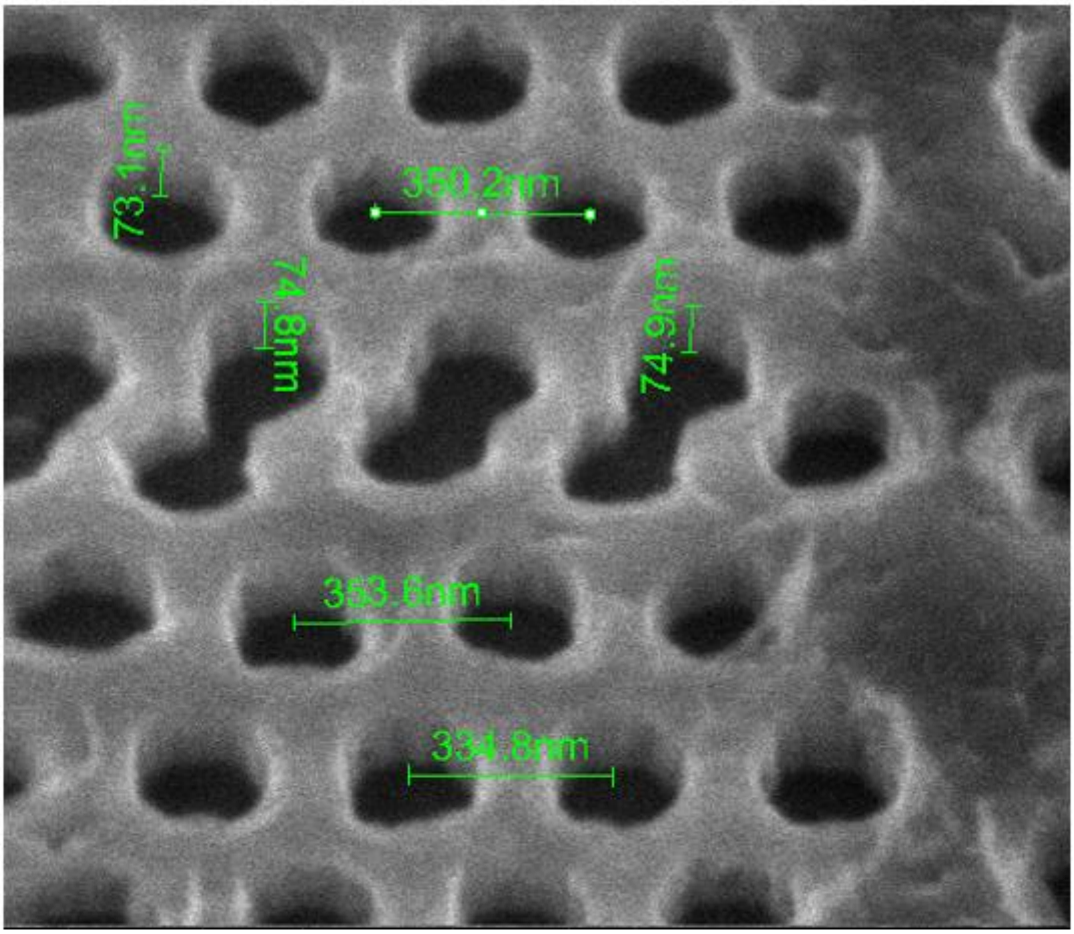

Figure 4.8 SEM images showing fabrication variation.

It can be seen that the target pitch size is 340nm, while the actual size varies from 334nm to 353nm. Furthermore, the shape of the hole is not a perfect circle. These fabrication tolerances result in the difference between experiments and simulations. Colour cross talk among pixels is reduced by mounting the filter mosaic upside down to minimize the effect of substrate thickness. This prevents the off normal incident light of one pixel entering the neighboring pixels. Further cross talk reduction was achieved by making each filter band of size 11.2 um covering 2 by 2 pixels (one pixel size: 5.6 um) to increase the light absorption by the photodetectors and hence to increases the signal content.

2.4 Integration of the hybrid colour mosaic onto a CMOS image sensor

The narrow band filter mosaic was then integrated onto a CMOS chip using a flip chip bonder (Figure 4.9) for accurate alignment as shown in Figure 4.6d.

Figure 4.9 Flip chip bonder (FINEPLACER@lambda) used to align the filter mosaic on the image sensor.

The top of the filter mosaic was coated with SOG to match the refractive index (thus increasing the transmission) and also to reduce the spectral width as well as preventing shorting the sensor while integration (the hybrid filter was integrated on the image sensor upside down to avoid cross talk). The image sensor used was SONY ICX618 with pixel size of 5.6µm and resolution of 0.3 Megapixels (640×480). The image sensor protective glass was removed for the filter integration (Figure 4.10).

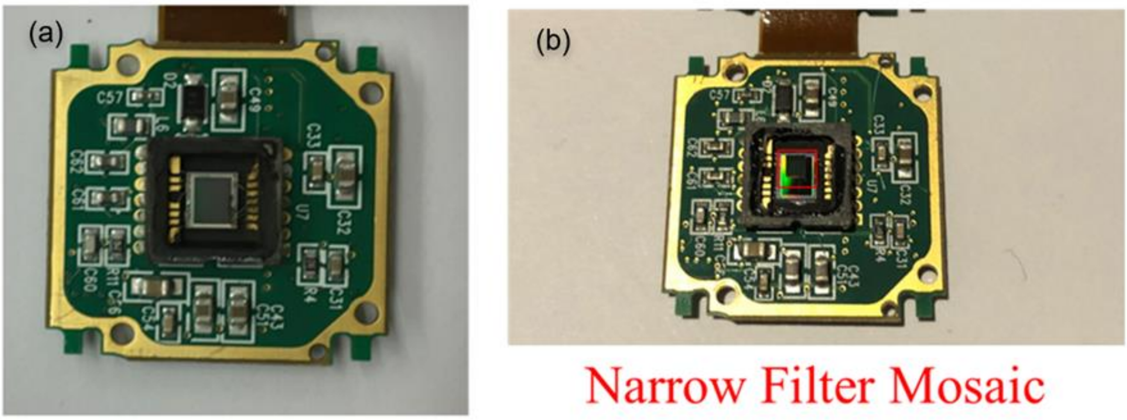

Figure 4.10 (a) SONY CMOS sensor with resolution 640×480 and a pixel size of 5.6 µm after removing the protective glass (b) The colour mosaic integrated on SONY CMOS sensor pixels using a flip chip bonder for alignment (size 3 cm× 3 cm).

To compensate for the low transmission of the filters and also to increase the light absorption in photodetectors (pixels), each filter in the mosaic covered a 2×2 block of photodetectors in the CMOS image sensor, resulting in 160×120 pixels per band. For the integration, the PMMA based homemade adhesive (the PMMA powder was diluted in a small amount of anisole, followed by staying in the 100 class cleaning room for two weeks for making the adhesive) is used between the filter mosaic and the image sensor while doing the integration using flip chip bonder. A thin layer of PMMA is spin coated on top of the image sensor and then integrate the filter on it after aligning with flip-chip bonder (Figure 4.9). The performance of the colour filter was also verified by integrating on another image sensor MT9P031.

The optics used for the camera has f number 1.4 with f = 6mm (f-focal length) and the developed single sensor based multispectral camera is shown in Figure 4.6e. The camera was characterized using a 24- patch Macbeth Color Checker as an object (Figure 4.11g).

8bit multispectral raw object data was captured by the camera and then transmitted to a laptop for image processing using MATLAB as shown in Figure 4.11a. Figure 4.11f shows a plot of the signals from the pixels across the transect indicated by the dashed red line across the Macbeth Chart in Figure 4.11a. The dotted red line spans across the grey colour patches on the Macbeth colour Checker and which shows the pixel intensity variations are captured in the raw image. A demosaicing algorithm was used to extract red, blue and green channels from the multispectral raw data of the Macbeth Chart (Figure 4.11b). The red, green and blue channels were recombined to get a colour image as shown in Figure 4.11c. Due to initial uncertainty of the RGB colour balance, colour correction and white balancing were required. Standard RGB spectrum could be sRGB, adobe RGB and so on, which indicate the values for R, G and B channel from 0 to 255 for 8 bit image. The three points of R, G and B for sRGB and adobe RGB are different, which results in a slightly different colour while using the same image processing such as interpolation or demosaicing. It is apparent that the CIE chart for the fabricated RGB filter in this chapter is also different from sRGB or adobe RGB, therefore requires colour corrections. Here colour balance and vibrance functions in the photoshop software were used for the colour correction and the white balance. Figure 4.11d and e show images after colour correction and white balancing, respectively.

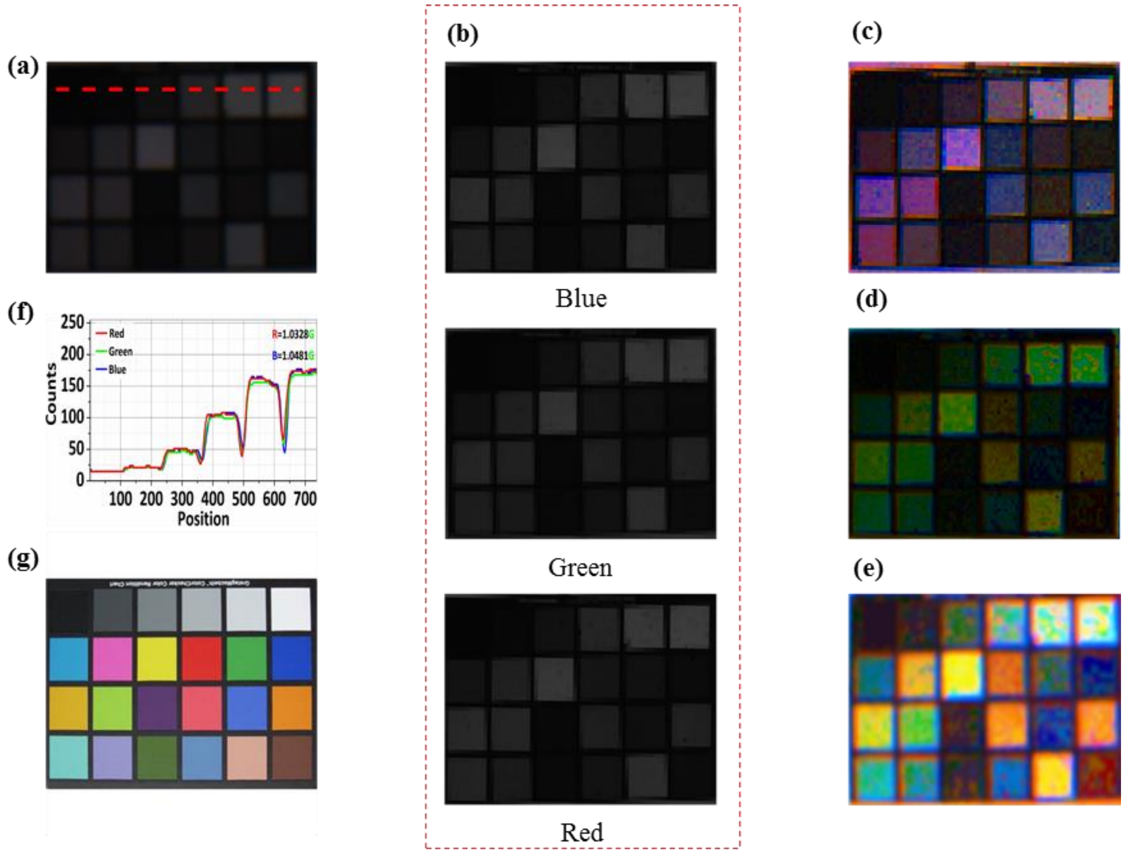

Figure 4.11 Image reconstruction process from the single sensor based multispectral camera (a) 8 bit multispectral raw data of 24 - patch Macbeth Chart captured by the multispectral camera (b) Three narrow wavelength channels (RGB) extracted from the raw image (c) The three channels are recombined to get a RGB colour image (d) The colour image after colour correction and (e) white balance, (f) the plot shows signals from pixel numbers along the dotted red line in the raw image (g) original image of the 24 -patch Macbeth Color Chart.

Figure 4.11 demonstrated that each band can be retrieved from the 8 bit multispectral raw image data. Another requirement of the multispectral image camera is extraction of each narrow band and then overlay for different spectral band combinations (red-green (RG), Green-Blue (GB) etc). Figure 4.12 shows that the recovered Macbeth Chart from Figure 4.11e can be used to recover different multispectral band combinations such as RG, RB and GB (Figure 4.12b) which is desirable in many applications for finding NDVI (normalised differential vegetation index) for precision agriculture to find plant diseases [26, 163], finding required information in a band for object identification and also in finding emissions in a narrow band for biomedical applications. Figure 4.12c shows the CIE chart of the recovered Macbeth Chart. The chart demonstrates that the recovered colour values are falling in the appropriate part of the colour space in comparison to a standard CIE chart of the Macbeth Chart (Figure 4.13).

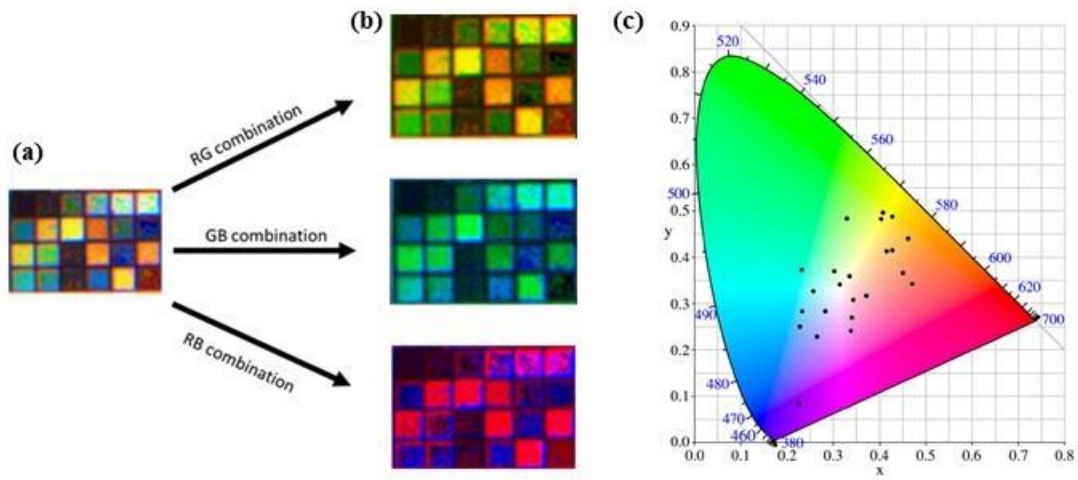

Figure 4.12 Demonstration of image overlay of different bands (a) recovered Macbeth Chart from the single sensor based multispectral camera from Figure 4.11 (b) RG, GB and RB combinations of Macbeth ColorChecker (c) CIE chart for the recovered 24-patch Macbeth colours.

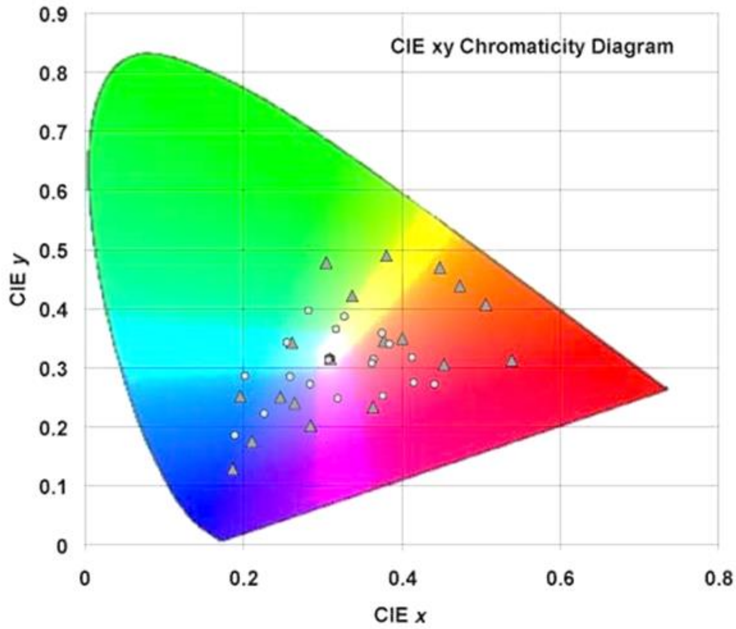

Figure 4.13 CIE chart of a standard Macbeth chart. Triangles indicate the original Macbeth chart in the CIE chart. Circles indicate the recovered Macbeth chart in the CIE chart.

The single sensor based multispectral camera was mounted on a DJI Phantom 3 for testing the sensor performance from a real aerial platform in an outdoor environment (an outer urban park) as shown in Figure 4.14a and b. The sensor was mounted without gimbal as shown in Figure 4.14a. Figure 4.14c shows the raw multispectral images of the Macbeth colour chart (printed on a A0 paper) on the ground captured from a 15 m height above the ground, the other patches are calibration images. Figure 4.14d shows pixel intensity values across a line over the white and black crossing and the Macbeth Chart images captured by the single sensor based multispectral camera. The pixel intensity variations with respect to positions are consistent with colour intensity variations in the Macbeth Chart and black and colour variations without any white balance. From the intensity variations, it was demonstrated that the image clarity was well within acceptable limits, which could clearly indicate the difference from black colour to grey and white colour. Furthermore, the suitability of the raw multispectral image for making handheld sensors for precision agriculture was demonstrated by creating a Red-Blue vegetation index (RBVI), $(R- B)\times255/(R+B)$. An area with green grass and dry grass was captured by holding the drone mounted camera 1.5 m above the ground and the recorded multispectral raw image is shown in Figure 4.14e. R, G and B individual bands were recovered from the raw multispectral image to get RBVI as shown in Figure 4.14f. RBVI image shows that area of high dense green grass (red colour in the image) compared to dry grass (blue colour) which demonstrates the capability of the sensor platform in real applications.

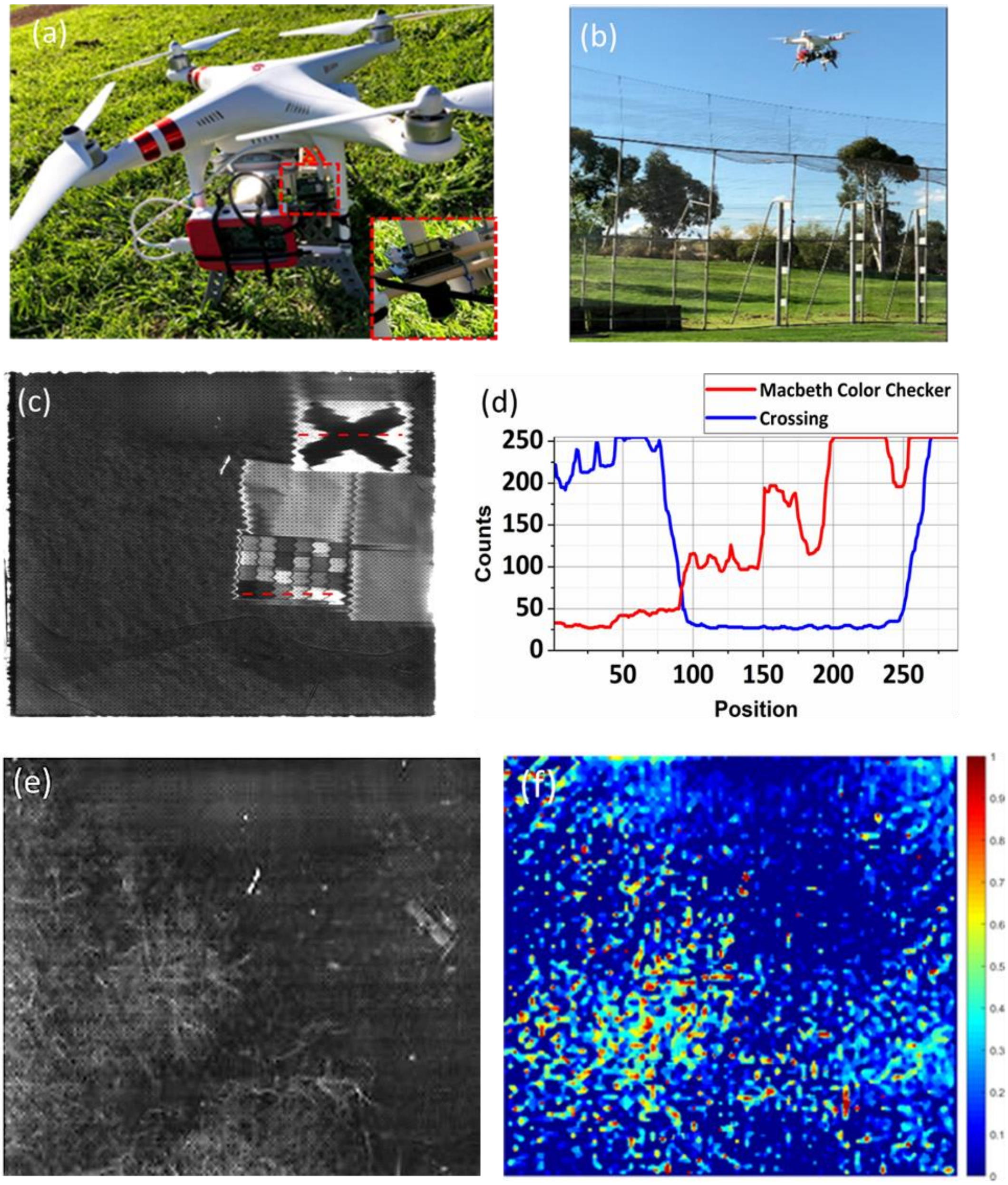

Figure 4.14 Demonstration of multispectral imaging of the camera using a drone platform (a) The single sensor based multispectral camera mounted on a DJI Phantom Drone without using any Gimbal (b) Image capturing using the camera (c) 8 bit raw Image captured from 15 m by the single sensor based camera showing the clarity of different patterns on ground (d) the plot shows signals from pixel numbers along the dotted red line in the raw image of crossing (blue line) and Macbeth Chart (red line) (e) 8 bit raw multispectral image of healthy grass and dry grass captured by the camera (f)

R, G and B bands are recovered from the raw multispectral image to get RB vegetation index (RBVI) . RBVI images shows area of high dense green grass (red colour in the image) compared to dry grass (blue colour).

3. Conclusion

In conclusion, the chapter demonstrated a single sensor based narrow band multispectral imaging using a hybrid RGB colour mosaic integrated onto a CMOS sensor. The colour mosaic was designed in such a way that multiple bands can be fabricated on a quartz wafer in a single run and offers easy tuning of colours, in contrast to conventional techniques that demand several independent runs with complex alignment processes. The hybrid filter mosaic was made of a heterostructured dielectric multilayer structure consisting of a Si_3N_4 – SiO_2 - Si_3N_4 sandwich as a common base layer for the filter mosaic to reduce the spectral width followed by a metal layer made of aluminum film perforated with holes on the base structure as a plasmonic layer. The colour tuning is achieved by varying the pitch of holes and hence can be fabricated in a single run with no complex alignment required for the different bands. The thickness values required for the base and the plasmonic layers were optimized to obtain narrow spectral widths. The spectral widths of the RGB mosaic are 60 nm, 60 nm and 45 nm for the red, green and blue, respectively. The mosaic is then integrated onto a Sony sensor using a flip-chip bonder for better alignment accuracy with a thin layer of PMMA for adhesion, and refractive index matching. The single sensor based narrow multispectral imaging capability was demonstrated using a Macbeth colour chart followed by retrieving individual bands using demosaicing techniques and their combination to retrieve the Macbeth Chart after colour correction and white balance. The sensor was then fitted onto a lightweight DJI Phantom 3 Drone to demonstrate its imaging capabilities in a field using RB Vegetation Index. Because only a single sensor chip was used for the camera, it required only around one third of the weight and power of a conventional multispectral camera. In general, weight, power and complexity were reduced by a factor of n times, (where n is the number of bands) compared to a conventional multispectral camera using multiple sensors, electronics and optics. The demonstrated sensor will have applications in drone-based imaging for precision agriculture, developing portable low-cost sensors for wound healing, blood vein detection, mining and forensic applications.

Furthermore, the low transmission in the measurement is due to the thick metal used in the design. However, to maintain a narrow FWHM, 150nm Al is optimized after rigorous simulations. There are several ways to increase the transmission efficiency and maintain a narrow FWHM and that aspect is discussed in Chapter 5.

Chapter 5 Hybrid colour filters for multispectral imaging

Multispectral cameras capture images in multiple wavelengths in narrow spectral bands. They offer advanced sensing well beyond normal cameras and many single sensor based multispectral cameras have been commercialized aimed at a broad range of applications, such as agroforestry research, medical analysis and so on. However, the existing single sensor based multispectral cameras require accurate alignment to overlay each filter on image sensor pixels, which makes their fabrication very complex, especially when the number of bands is large. This paper demonstrates a new filter technology using a hybrid combination of single plasmonic layer and dielectric layers by computational simulations. A filter mosaic of various bands with narrow spectral width can be achieved with single run manufacturing processes (i.e., exposure, development, deposition and other minor steps), regardless of the number of bands.

1. Introduction

Multispectral camera (MC) technology has the ability to collect information well beyond human eyes or normal colour cameras. This is because human eyes and conventional colour cameras receive an image in three colour bands (red, green and blue (RGB)) with broad spectral widths. Hence, it is difficult to distinguish fine spectral features within the image captured across the bands due to their overlap. For example, the spectral width in the conventional cameras is around 80 nm to 100 nm for each of the RGB bands. Multispectral cameras based on a single image sensor capture images in multiple wavelengths using narrow band filters fitted on each image sensor pixel [41-43, 175]. It is possible to extract additional spectral information otherwise not possible from these multiple images [25-26, 29-30, 35, 37, 41-43, 91, 175]. The spectral width of each band is measured at FWHM of the spectral distribution, where FWHM is defined as the wavelength range at which the received optical power is half of its maximum.

MC technology sub-divides the information collected by the image sensor into narrow bands defined by the small FWHM values of its constituent filters. The filtered information can then be grouped, processed and highlighted to show a large contrast with its reference background. Examples are already abound across diverse applications. In gastroenterology research, each observed case (i.e., tissue type) may relate to a particular range of electromagnetic radiation or to a different reflectance spectrum. In this case, ulceration of the colon has been shown to exhibit a larger reflectance at the boundary between red and NIR wavelengths (around 600nm to 1000nm) [26] and can therefore be made to appear much brighter against a non-diseased background. In the pathology area, the location of veins can be difficult to detect for many reasons, such as dark skin, excess loss of blood or even extreme dehydration. To solve this problem, MC been applied as either a combination of a commercial camera and a NIR bandpass filter or a standard camera together with a NIR illuminator. As NIR light will easily penetrate the skin, medical staff are able to more easily to identify the exact position of veins [25]. In agroforestry research, it is known that diseased or stressed plants reflect more NIR light than healthy leaves. Thus, MC systems have been installed on drone aircraft to fly over the crops, observing harvest conditions in real time [29].

There are three different types of MC system currently on the market. The first uses multiple cameras with a single narrow-band filter in front of each camera [30, 35]. This type of system can be easily customized simply by replacing the spectral filter with one appropriate to the specific application. The main disadvantage is that these multiple camera platforms tend to be bulk and power hungry, which limits their use [91]. Moreover, each camera has their own imaging viewpoint which creates co-registration problems [37-38]. While second MC systems with single camera plus a rotating optical filter disk can eliminate the viewpoint disparity problem, they are still quite bulky and introduce time shifts that complicate the processing of moving images, such as when the system is integrated with a drone for agroforestry applications [30].

The third type of MC available on the market is based on a single camera sensor called single sensor based multispectral camera (SSMCs) [41-43, 175]. While the filter technologies employed in these systems are almost universally commercial-in-confidence, the limited information available in the open literature (e.g., [175]) indicates that the filter wavelength is typically tuned by changing the filter material and/or its thickness. This kind of technology is also described in many recent research papers [57-58] and patents [67-70]. It is worth mentioning that the photodetector under each pixel collects the optical signal after it has passed through both a micro-lens and the filter layer(s) [1]. There are typically two ways to install a filter array on top of an image sensor. It can be either fabricated onto a substrate and then aligned with the image sensor, or the array can be directly fabricated onto the surface of the sensor itself. Either method requires a large number of separate fabrication processes for each individual spectral band, such as pixel-to-pixel mask alignment, UV exposure, and filter installation. Therefore, the fabrication can become extremely complicated for making a filter mosaic with required number of bands, particularly in the case of hyperspectral filters where the number of filters (bands) may reach into the hundreds [91, 175]. The filter technology makes the SSMCs very expensive and hence limits their usage in wide applications.

This has triggered research on new filter technologies suitable for SSMCs. The two main requirements of the filter technology are developing technologies with less complex fabrication process and getting spectral width (FWHM) narrow for bands. There has been much activity aimed at improving the FWHM of the bands, as evidenced by recent patents and published papers [1, 17-21, 23, 57-58, 67-70, 73, 80, 88-90, 94, 107]. By far the smallest FWHM reported to date in the visible/NIR range is approximately 0.11nm observed only over 10 nm wavelength range in a dielectric grating structure [73]. A metallic grating structure has also been demonstrated in which an aluminium grating built on an Al_2O_3 buffer layer, in turn located on a quartz substrate, results in a minimum FWHM of 20nm [90]. Metal-Dielectric-Metal (MDM) or even MDMDM metallic gratings have also been designed and optimized to exhibit good FWHM values of under 30nm [89]. However, as these metallic grating structures have been shown to be polarization dependent, SSMCs based on them may fail to collect an optical signal if the incident light is in an opposite polarization direction.

Metallic hole array based multispectral filters have been proposed [21, 23, 73, 91] that show FWHM value smaller than 50nm. Although these multispectral filters have been applied to colour and multispectral imaging applications [91], they are unable to operate cover the whole visible and NIR range. Si nanowire based narrow bandpass filter arrays have also been integrated on a monochrome image sensor for multispectral imaging, but with mechanical scanning and have a FWHM greater than 50nm [80].

In this paper, we demonstrate a new filter technology suitable for multispectral imaging using a hybrid combination of single plasmonic layer and dielectric multilayers. The hybrid filters can produce spectral width (FWHM) values smaller than 50nm, with a minimum FWHM as low as 17nm at some wavelengths. Moreover, these proposed multispectral filters are easily tuneable and a multiband filter mosaic can be manufactured using a single stage maskless fabrication process regardless of the number of spectral bands, including one-time exposure, chemical development and filter deposition. We have demonstrated two filter structures as examples, one exploiting localized surface plasmons resonances and other using surface plasmon resonances using the proposed hybrid topology to demonstrate their operation in the visible and NIR wavelengths by computational simulations.

2. Design of Hybrid Multispectral Filters

2.1 Angle Independent Narrow Bandpass Filters based on the Localized Surface Plasmon Resonances

In the first of the proposed filters presented here, Aluminium (Al) disks structures were investigated. Previously, these have been used to develop subtractive colour filtering as the different resonant wavelengths (valley wavelengths) depend largely on the disk diameter [100]. Subtractive primary colours typically include cyan, magenta and yellow, and are the inverse transmission spectra of red, green and blue respectively. This work has resulted in the multispectral filter mosaic (RGB colour filter plus NIR filter) using Al disk in a square array using the proposed hybrid technique; Al disc (plasmonic layer using localized surface plasmons) and dielectric layers (silicon nitride (Si_3N_4) and spin-on-glass (SOG)).

An initial narrow-band filter was designed and optimized using finite element method (FEM) implemented in the simulation software COMSOL Multiphysics 5.5. The device geometries were designed and simulated in 3D using radiofrequency module (RF module) in COMSOL Multiphysics. Periodic boundary condition (PBC) and semi-infinite boundary condition (perfect electric conductor and perfect magnetic conductor) were used for studying the effects of infinite and semi-infinite filter size. Perfectly Matched layers were used to suppress any unwanted reflections in the simulation model. Scattering boundary condition was used to terminate the simulation boundaries where reflection effects are minimal. Transmission coefficient is obtained from S- parameters using the port boundary conditions. We found by appropriately arranging the Al disks in a square array as shown in Fig. 1(a), the peak transmission wavelength can be tuned by varying the diameter of the Al disk, while the optimal spacing between two adjacent disks was found to be around 1/10th of the peak wavelength. In these simulations, the substrate is quartz with a refractive index of 1.5. A 250nm thick Si_3N_4 layer with a refractive index of 2 was deposited as a buffer layer on the quartz. Onto this buffer layer, a thin plasmonic layer of 50nm Al disks with refractive index [158] was designed to tune the peak wavelength. Lastly, a coating of 200nm Spin on glass (SOG) covered the sample. The general 3D structure of the filter is shown in Fig. 1(b). PMLs were applied at the top and bottom, SBCs layers to the remaining sides of the simulation model. Port boundary conditions with propagation constants of $2\pi\times1.42/\lambda$ for SOG and $2\pi\times1.5/\lambda$ for quartz were used between the top PML and SOG as well as between the bottom PML and the quartz. Periodic boundary conditions (PBC) were applied on the four sides of the middle Al disk (unit cell as shown in Fig 1 (a) dotted lines) and Si_3N_4 block.

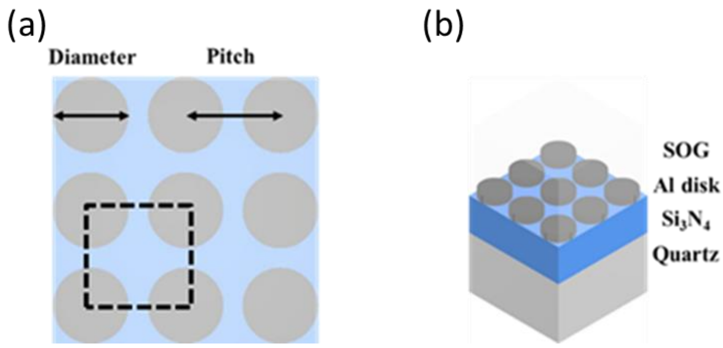

Figure 5.1 Schematic of the proposed narrow-band filter based on the hybrid Al disk (a) top view of the filter (dotted line shows the unit cell used in the simulation) (b) 3D representation of the filter structure with the plasmonic layer (Al disc) and dielectric layers (Si_3N_4 and SOG).

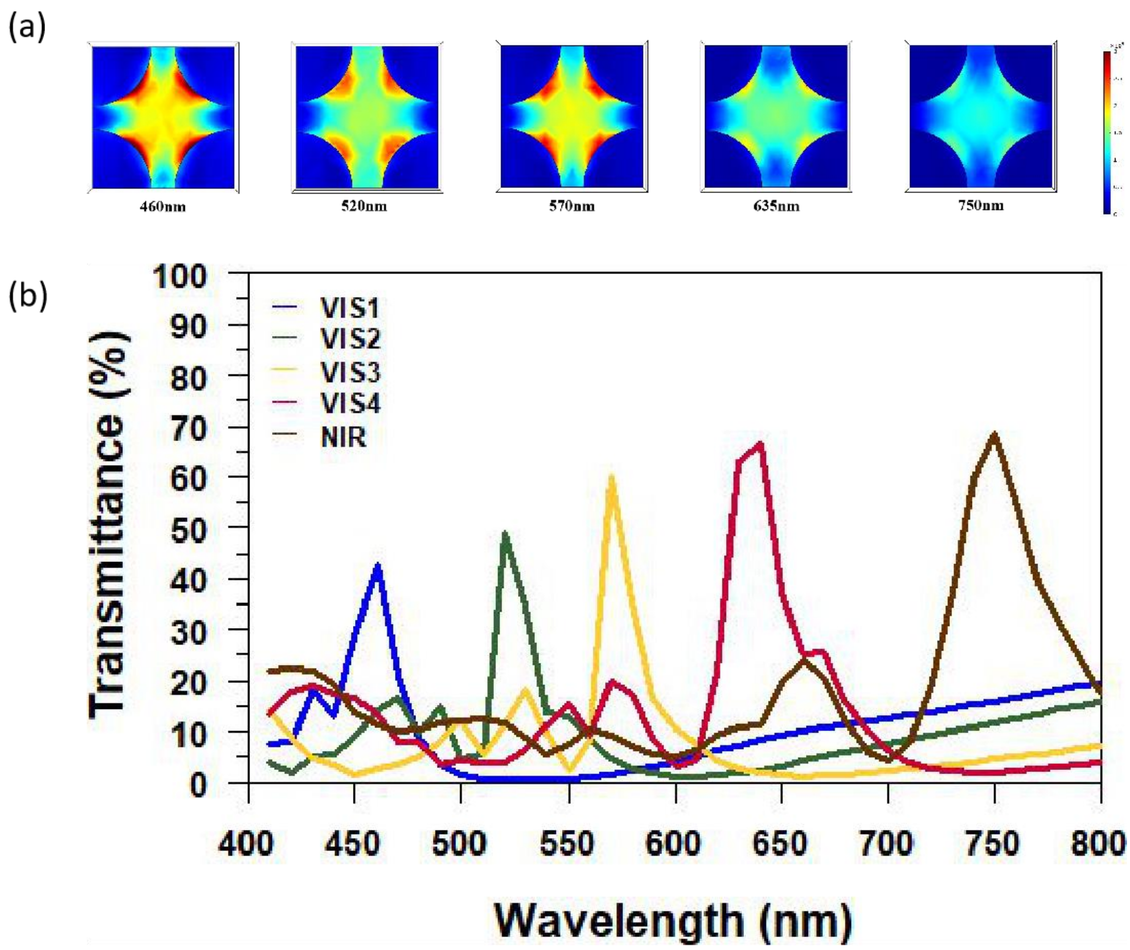

Figure 5.2 (a) Normalized electric field of localised surface plasmons for blue (460 nm), green (520 nm), yellow (570 nm), red (635 nm) and NIR (750 nm) (b) Transmission spectra of hybrid Al disk based multispectral filters with respect to the wavelengths mentioned in (a).

The transmission efficiency was calculated using s-parameter, $|S21|^2$. Figure 5.2a shows the normalized electric field at peak wavelengths for blue (460 nm), green (520 nm), yellow (570 nm), red (635 nm) and NIR (750 nm) showing the localized surface plasmons. The resulting FWHM for green and yellow (Figure 5.2b) are about 18nm and 15nm, respectively, with transmission efficiency values larger than 45%. The wavelength tuning was mainly achieved by tuning diameter of the disk (Figure 5.1a). Table 5.1 shows the optimized filter parameters along with their optical characteristics.

Table 5.1 Results of blue, green, yellow, red and NIR narrow bandpass filters.

Parameter	Blue	Green	Yellow	Red	NIR
Peak Wavelength (nm)	460	520	570	635	750
Period (nm)	240	280	310	350	420
Disk Diameter (nm)	200	220	260	280	340
Peak Transmission	42%	48%	60%	65%	68%
FWHM (nm)	25	18	15	30	45

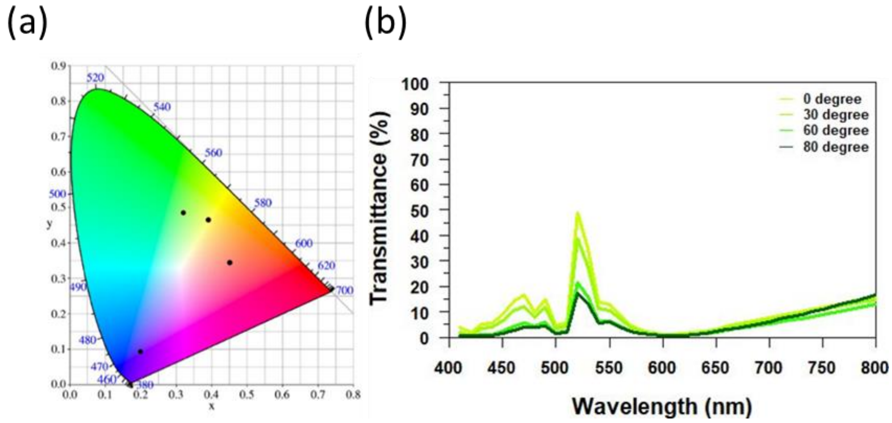

Figure 5.3 (a) CIE chromaticity chart for green, blue, yellow and red (b) Transmission vs Wavelength over FFOV: 0° ≤ Angle of Incidence ≤ 80°

Figure 5.3a shows the CIE chromaticity chart overlaid with the transmission data of blue, green and red showing that the filter values are falling in the appropriate part of the color space. The transmission efficiency with respect to angle of incidence was investigated using the green filter (520nm) as shown in Figure 5.3b. The full field of view (FFOV) values varied from 0° (i.e., normal to the surface) to 80° off-axis. It was observed that the peak wavelength position not shifted with respect to the angle with minimum reduction in the transmission intensity up to 30%. Furthermore, when the FFOV is 80°, the green filter may adversely affect the optical response of the NIR.

It can be seen from Table 1 that the proposed hybrid filter geometry made of Al nano-disks and a Si_3N_4 layer exhibits FWHM values smaller than 50nm in the visible and NIR wavelength and is therefore a promising candidate for making multispectral filter mosaic. When the peak wavelength is smaller than 600nm, the FWHM reduces to about 15nm, which is suitable for making multispectral cameras with high number of bands. Moreover, the proposed narrow-band filter behavior is independent of the angle of incidence and, as all the structures (substrate, Si_3N_4, Al, SOG) have the same base thickness, the array requires only a single-exposure fabrication process without any mask alignment.

2.2 Metallic Nanohole Array Integrated on a Dielectric Multilayer for IR Multispectral Imaging

The second of the two structures presented in this paper is a hybrid filter illustrated in Fig. 4 using surface plasmon resonances. This filter is made up of a plasmonic filter on a dielectric multilayer on top of a quartz substrate (refractive index 1.5) covered with Spin on Glass with refractive index 1.42 (Fig. 4). A dielectric multilayer is formed from a layer of SiO_2 with refractive index (n1) of 1.45 surrounded by two TiO_2 layers with larger refractive indexes (n2) of 2.1. The thickness of the TiO_2 layers are both 190nm, which is a quarter of the target NIR wavelength of 760nm. The SiO_2 layer is determined by the equation $d_1n_1=d_2n_2$, where d_1 and d_2 are the thicknesses of the SiO_2 and TiO_2 layers, respectively, and $n_{1/2}$ are the corresponding refractive indices, resulting in a SiO_2 thickness of approximately 280nm. This part of the filter on its own behaves as an anti-reflection layer with a passband from approximately 650nm to 1000nm as illustrated by the transmission spectrum (Fig. 5.) of the dielectric multilayer before the plasmonic layer is added. The plasmonic filter comprises an array of nano-holes in a hexagonal arrangement [38] inserted in the 150nm Au film. Fig. 5 (a) shows the normalized electric field of the surface plasmons in the hole array (top view) at peak wavelengths for NIR 1-5.

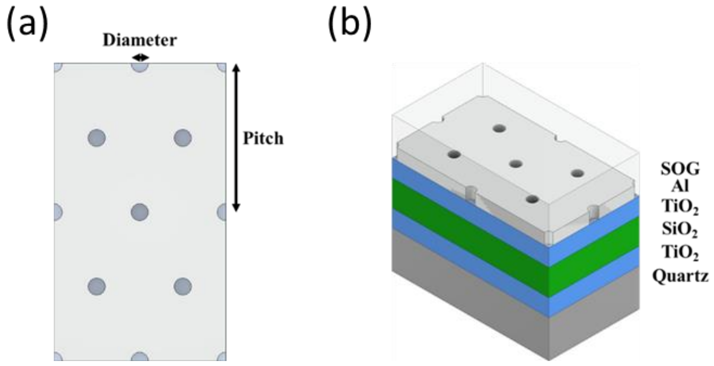

Figure 5.4 Nanostructure of the proposed hybrid IR multispectral filter (a) top view (b) 3D structure of the filter structure (Al – Plasmonic layer and TiO_2, SiO_2, SOG are dielectric layers)

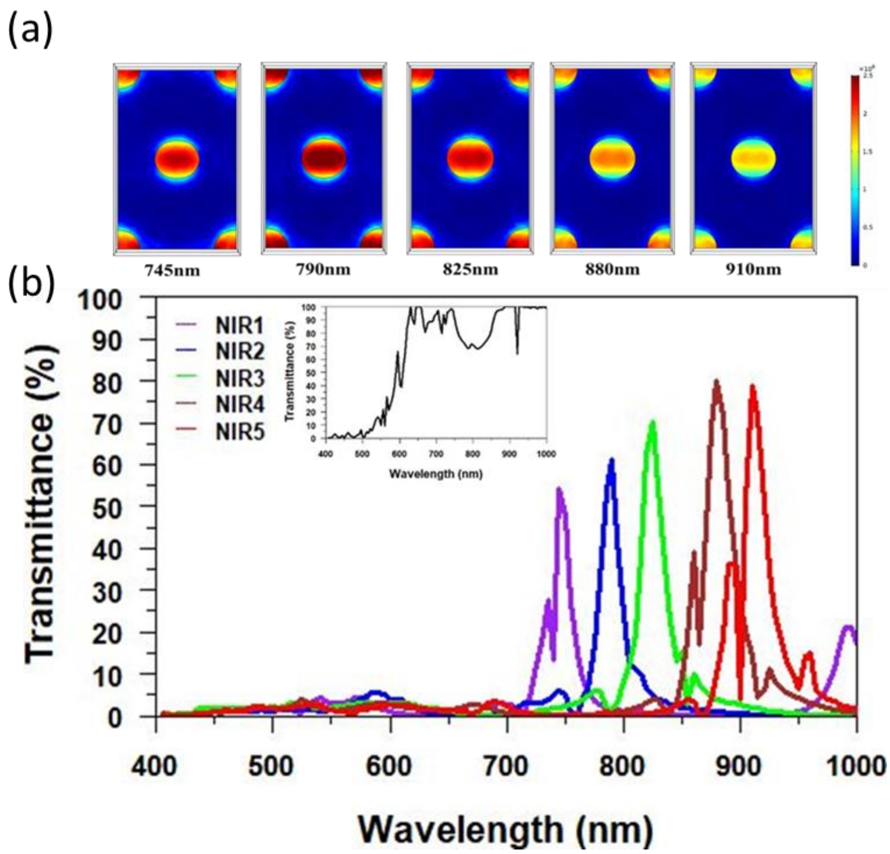

Figure 5.5 (a) Normalized electric field of the surface plasmons in the hole array at peak wavelengths for NIR 1-5 (b) The simulated transmission spectrum of the hybrid IR multispectral filters. The inset shows the transmission spectrum of TiO_2-SiO_2-TiO_2 dielectric multi-layer without the plasmonic layer.

Table 5.2 Results of Au hole array integrated with TiO_2-SiO_2-TiO_2 multilayer.

Peak wavelength (nm)	745	790	825	880	910
Period (nm)	480	520	550	600	630
Hole diameter (nm)	180	200	220	240	240
Peak transmission efficiency (%)	55	60	70	80	78
FWHM (nm)	20	20	22	25	20

The transmission efficiency and the resulting spectrum of the hybrid filter is plotted in Fig. 5 (b). The inset of Fig. 5 (b) shows the spectrum from TiO_2-SiO_2-TiO_2 dielectric multilayers without the plasmonic layer. The FWHM and peak transmission efficiency results for the device are presented in Table 2. As shown in Table 2, the FWHM of a multispectral filter in the NIR wavelength can be less than 25nm (typically around 20nm) with a best-case transmission efficiency of 80%. The dielectric multilayer remains the same in each case, showing that the peak wavelength can be tuned by simply adjusting the period between adjacent holes. However, hole array based filters are limited in the angle independant performance due to the SPPs. Colour filters based on LSPs are more angle independent than SPPs based ones. We have carried out further simulations to study the effect of non-infinite filter size on the transmission coefficient and spectral width by replacing the periodic boundary conditions with semi-infinite boundary condition. The transmission efficiency and spectral width are almost the same for the metallic disk based structure due the LSP, where one single disc can produce colour. But hole array requires interference of surface plasmons and hence multiple holes are required for producing a colour. For the hole array based structure, the spectral width and transmission efficiency were reduced as the pixel size decreased. This requires covering the hole array based filter on at least 2x2 pixels on the image sensor with filter pixel size of 4.8 um along with suitable optics to produce required spectral width and acceptable transmission.

3. Conclusion

In conclusion, this paper has presented a multispectral filter technology using a hybrid combination of single plasmonic layer and dielectric layers by computational simulations. The hybrid filter technology has reduced the fabrication complexity to a single stage process for making any number of bands in a filter mosaic with narrow spectral widths and easy wavelength tuneability. We have demonstrated working of the proposed hybrid design in the visible and NIR using two filter examples, one using localized surface plasmons resonances and other surface plasmon resonances. This proposed technology will significantly reduce the fabrication complexity and cost of multispectral filter mosaic compared to the existing complex SSMC filter techniques. The current technology will further make the SSMCs applied in wider applications in precision agriculture, medicine, forestry, night vision and remote sensing. While in the future, the number of bands should be increased and spectral width is expected to be reduced to less than 10nm for making low cost single sensor based hyper spectral cameras.

Chapter 6 Conclusions and Future Research Directions

This thesis investigated the development of a new low-cost single sensor based multispectral image camera exploring the nanophotonics. Different filter mosaic structures were designed, optimised and fabricated. The performance of the filter mosaics were tested by integrating with monochrome image sensors and processing the captured images using the standard Macbeth chart.

The study started with a novel strategy developed using computational simulations to overcome the challenge with low transmittance plasmonic coaxial hole array based colour filters without compromising its advantages, such as polarization and incident angel independence. Therefore, in the future with more advanced nanotechnology, this kind of nanostructure should be further researched and fabricated, as it combines the advantage of SPP based colour filter (e.g. metallic nanohole array) and LSP based colour filter (e.g. Al disk).

The CMY colour filter with new nanostructure was also demonstrated. This structure is based on the symmetric metal-dielectric-metal nanorod. In this case, the transmission spectrum can be sharp, and its transmission contrast can be maximized. Later, this CMY filter was integrated on a monochrome image sensor to make a CMY camera. A raw image was taken with CMY camera, after image processing, the colour of the images can be recovered.

A single sensor based multispectral cameras were presented in Chapter 4 and Appendix. As introduced in Chapter 1, the current multispectral imaging system (MIS) with multiple cameras has the following problem, such as power hungry, bulk size, image co-registration. Even though single sensor based multispectral camera in the markets can solve this problem, each band has its own thickness or material and requires mask alignment, making the whole filter fabrication complicated when the number of bands is more than hundred. The filter technology in Chapter 4 can solve these problems addressed above, the multispectral filter mosaic with spectral width (FWHM) of 45nm was integrated on a monochrome image sensor for colour imaging and multispectral imaging. Appendix demonstrates a novel mass producible filter mosaic technology to further reduce spectral width (FWHM) to 17nm. A 6 band filter mosaic was also integrated on an image sensor for the multispectral imaging applications.

Future development would focus on combining the advantage of filter technology in Chapter 4, which requires single exposure fabrication but has FWHM smaller. The multispectral filter design in Chapter 5 may be a good start to solve this issue. This novel filter technology results in a minimum FWHM of 15nm, and can cover visible and NIR wavelength, it is only presented with simulations, and can be fabricated in the future.

Reference

[1] Huo, Y., Fesenmaier, C. C., & Catrysse, P. B. (2010). Microlens performance limits in sub-2μm pixel CMOS image sensors. Opt. Express, 18, 5861-5872. doi:10.1364/OE.18.005861

[2] Lee, W.-G., Kim, J.-S., Kim, H.J., Kim, S.Y., Hwang, S.B., & Lee, J.-G. (2005). Two-dimensional optical simulation on a visible ray passing through inter-metal dielectric layers of CMOS image sensor device. Journal- Korean Physical Society, 47. 434-439.

[3] Ahn, J., Moon, C.-R., Kim, B., Lee, K., Kim, Y., Lim, M., Lee, W., Park, H., Moon, K., Yoo, J., Lee, Y., Park, B., Jung, S., Lee, J., Lee, T.-H., Lee, Y., Jung, J., Kim, J.-H., Kim, T.-C., Cho, H., Lee, D., & Lee, Y. (2008). Advanced image sensor technology for pixel scaling down toward 1.0μm (Invited). 2008 IEEE International Electron Devices Meeting, CA, 1-4. doi:10.1109/IEDM.2008.4796671

[4] Moon, C., Shin, J.-C., Kim, J., Lee, Y. K., Cho, Y.-J., Yu, Y.-Y., Hwang, S.-H., Park, D.-C., Park, B. J., Kim, H.-Y., Lee, S.-H., Jung, J., Cho, S.-H., Lee, K., Koh, K., Lee, D., Kim, K. (2007). Dedicated process architecture and the characteristics of 1.4 μm pixel CMOS image sensor with 8M density. 2007 IEEE Symposium on VLSI Technology, Kyoto, 62-63. doi:10.1109/VLSIT.2007.4339728

[5] Catrysse, P. B., & Wandell, B. A. (2002). Optical efficiency of image sensor pixels. J. Opt. Soc. Am. A, 19, 1610-1620. doi:10.1364/JOSAA.19.001610

[6] Fesenmaier, C. C., Huo, Y., & Catrysse, P. B. (2008). Optical confinement methods for continued scaling of CMOS image sensor pixels. Opt. Express, 16, 20457-20470. doi:10.1364/OE.16.020457

[7] Catrysse, P. B., & Wandell, B. A. (2003). Integrated color pixels in 0.18-μm complementary metal oxide semiconductor technology. J. Opt. Soc. Am. A, 20, 2293-2306. doi:10.1364/JOSAA.20.002293

[8] Structure of Color Filters. (2020, April). Retrieved from https://www.toyo-visual.com/en/products/fpdcf/colorfilter.html

[9] Technology of color filter materials for image sensor. (2020, April). Retrieved from https://www.imagesensors.org/Past%20Workshops/2011%20Workshop/2011%20Papers/I01_Taguchi_ColorFilter.pdf

[10] Agranov, G., Berezin, V., & Tsai, R. H. (2003). Crosstalk and microlens study in a color CMOS image sensor. IEEE Transactions on Electron Devices, 50(1), 4-11. doi:10.1109/TED.2002.806473

[11] Rhodes, H., Agranov, G., Hong, C., Boettiger, U., Mauritzson, R., Ladd, J., Karasev, I., McKee, J., Jenkins, E., Quinlin, W., Patrick, I., Li, J., Fan, X., Panicacci, R., Smith, S., Mouli, C., & Bruce, J. (2004). CMOS imager technology shrinks and image performance. IEEE Workshop on Microelectronics and Electron Devices, USA, 7-18. doi:10.1109/WMED.2004.1297338

[12] Hsu, T. H., Fang, Y. K., Lin, C. Y., Chen, S. F., Lin, C. S., Yaung, D. N., Wuu, S. G., Chien, H. C., Tseng, C. H., Lin, J. S., & Wang, C. S. (2004). Light guide for pixel crosstalk improvement in deep submicron CMOS image sensor. IEEE Electron Device Letters, 25(1), 22-24. doi:10.1109/LED.2003.821597

[13] Kim, S., Han, S., Kang, B., Lee, K., Kim, J. D. K., & Kim, C.-Y. (2010). A Three-Dimensional Time-of-Flight CMOS Image Sensor With Pinned-Photodiode Pixel Structure. IEEE Electron Device Letters, 31(11), 1272-1274. doi:10.1109/LED.2010.2066254

[14] Goossens, S., Navickaite, G., Monasterio, Gupta,C. S., Piqueras, J. J., Pérez, R., Burwell, G., Nikitskiy, I., Lasanta, T., Galán, T., Puma, Eric., Centeno, A., Pesquera, A., Zurutuza, A., Konstantatos, G., & Koppens, F. (2017). Broadband image sensor array based on graphene–CMOS integration. Nature Photon, 11, 366–371. doi:10.1038/nphoton.2017.75

[15] Yu, Y., Chen, Q., Wen, L., Hu, X., & Zhang, H.-F. (2015). Spatial optical crosstalk in CMOS image sensors integrated with plasmonic color filters. Opt. Express, 23, 21994-22003. doi:10.1364/OE.23.021994

[16] Miyata, M., Nakajima, M., & Hashimoto, T. (2019). High-Sensitivity Color Imaging Using Pixel-Scale Color Splitters Based on Dielectric Metasurfaces, ACS Photonics, 6(6), 1442-1450. doi:10.1021/acsphotonics.9b00042

[17] He, X., O'Keefe, N., Liu, Y., Sun, D., Uddin, H., Nirmalathas, A., & Rajasekharan Unnithan, R. (2018). Transmission Enhancement in Coaxial Hole Array Based Plasmonic Color Filter for Image Sensor Applications. IEEE Photonics Journal, 10(4), 1-9. doi:10.1109/JPHOT.2018.2855684

[18] Rajasekharan, R., Balaur, E., Minovich, A., Collins, S., James, T. D., Djalalian-Assl A., Ganesan, K., Tomljenovic-Hanic, S., Kandasamy, S., Skafidas, E., Neshev, D. N., Mulvaney, P., Roberts, A. & Prawer, S. (2015). Filling schemes at submicron scale: Development of submicron sized plasmonic colour filters. Sci Rep, 4, 6435. doi:10.1038/srep06435

[19] Rajasekharan Unnithan, R., Sun, M., He, X., Balaur, E., Minovich, A., Neshev, D. N., Skafidas, E., & Roberts, A. (2017). Plasmonic Colour Filters Based on Coaxial Holes in Aluminium. Materials, 10(4). doi:10.3390/ma10040383

[20] He, X., Liu, Y., Beckett, P., Uddin, H., Nirmalathas, A., & Rajasekharan Unnithan, R. (2019). Transmission enhancement in plasmonic nanohole array for colour imaging applications. Proc. SPIE, AOS Australian Conference on Optical Fibre Technology (ACOFT) and Australian Conference on Optics, Lasers, and Spectroscopy (ACOLS), 11200. doi:10.1117/12.2541299

[21] He, X., O'Keefe, N., Sun, D., Liu, Y., Uddin, H., Nirmalathas, A., & Unnithan, R. R. (2018). Plasmonic Narrow Bandpass Filters Based on Metal-Dielectric-Metal for Multispectral Imaging. CLEO Pacific Rim Conference 2018, Th4E.5. doi:10.1364/CLEOPR.2018.Th4E.5

[22] Zeng, B., Gao, Y., & Bartoli, F. (2013). Ultrathin Nanostructured Metals for Highly Transmissive Plasmonic Subtractive Color Filters. Sci Rep, 3, 2840. doi:10.1038/srep02840

[23] Liang, Y., Zhang, S., Cao, X., Lu, Y., & Xu, T. (2017). Free-standing plasmonic metal-dielectric-metal bandpass filter with high transmission efficiency. Sci Rep, 7, 4357. doi:10.1038/s41598-017-04540-9

[24] Multispectral Imaging, Detection and Active Reflectance (MiDAR). (2020, April). Retrieved from https://www.nasa.gov/centers/ames/cct/office/cif/ved-chirayath

[25] Pan, C.-T., Francisco, M.D., Yen, C.-K., Wang, S.-Y., & Shiue, Y.-L. (2019). Vein Pattern Locating Technology for Cannulation: A Review of the Low-Cost Vein Finder Prototypes Utilizing near Infrared (NIR) Light to Improve Peripheral Subcutaneous Vein Selection for Phlebotomy. Sensors, 19, 3573. doi:10.3390/s19163573

[26] Ortega, S., Fabelo, H., Iakovidis, D.K., Koulaouzidis, A., & Callico, G.M. (2019) Use of Hyperspectral/Multispectral Imaging in Gastroenterology. Shedding Some–Different–Light into the Dark. J. Clin. Med, 8(36). doi:10.3390/jcm8010036

[27] Yao, L., Gu, X., Zhong, Y., Han, Z., Shi, Q., Fu, Y., Liu, C., Wang, X., & Xie, T. (2016). Image enhancement based on in vivo hyperspectral gastroscopic images: a case study. Journal of Biomedical Optics, 21(10), 101412. doi: 10.1117/1.jbo.21.10.101412

[28] Ai, X., Wang, Z., Cheong, H., Wang, Y., Zhang, R., Lin, J., Zheng, Y., Gao, M. & Xing, B. (2019). Multispectral optoacoustic imaging of dynamic redox correlation and pathophysiological progression utilizing upconversion nanoprobes. Nat Commun, 10, 1087. doi:10.1038/s41467-019-09001-7

[29] Mahajan, Ujjwal. (2016). Drones for Normalized Difference Vegetation Index (NDVI), to Estimate Crop Health for Precision Agriculture: A Cheaper Alternative for Spatial Satellite Sensors.

[30] Themelis, G., Yoo, J. S., & Ntziachristos, V. (2008). Multispectral imaging using multiple-bandpass filters. Opt. Lett, 33, 1023-1025. doi:10.1364/OL.33.001023

[31] Hohmann, M., Kanawade, R., Klämpfl, F., Douplik, A., Mudter, J., Neurath, M.F., & Albrecht, H. (2017). In-vivo multispectral video endoscopy towards in-vivo hyperspectral video endoscopy. J. Biophotonics, 10, 553–564. doi:10.1002/jbio.201600021

[32] Masood, K., Rajpoot, N., Rajpoot, K., & Qureshi, H. (2006). Hyperspectral Colon Tissue Classification using Morphological Analysis. In Proceedings of the International Conference on Emerging Technologies, Pakistan, 735–741. doi:10.1109/ICET.2006.335947

[33] Rajpoot, K., & Rajpoot, N. (2004). SVM Optimization for Hyperspectral Colon Tissue Cell Classification. Medical Image Computing and Computer-Assisted Intervention – MICCAI 2004, Germany. 3217. doi:10.1007/978-3-540-30136-3_101

[34] Maryanto, A., Widijatmiko, N., Sunarmodo, W., Soleh, M. & Arief, R. (2017). DEVELOPMENT OF PUSHBROOM AIRBORNE CAMERA SYSTEM USING MULTISPECTRUM LINE SCAN INDUSTRIAL CAMERA. International Journal of Remote Sensing and Earth Sciences (IJReSES), 13(27). doi:10.30536/j.ijreses.2016.v13.a2701

[35] Imaging system. (2020, April). Retrieved from http://www.tetracam.com/ImagingSystems.htm

[36] Mathews, S. A. (2008). Design and fabrication of a low-cost, multispectral imaging system. Appl. Opt, 47, 71-76. doi:10.1364/AO.47.000F71

[37] Skauli, T. (2012). An upper-bound metric for characterizing spectral and spatial coregistration errors in spectral imaging. Opt. Express, 20, 918-933. doi:10.1364/OE.20.000918

[38] Coulter, L.L., & Stow, D.A. (2008). Assessment of the Spatial Co-registration of Multitemporal Imagery from Large Format Digital Cameras in the Context of Detailed Change Detection. Sensors, 8, 2161-2173. doi:10.3390/s8042161

[39] Khaghani, F., & Nelson, R. J. (2007). Co-registration of multispectral images for enhanced target recognition. Proceedings of SPIE - The International Society for Optical Engineering, United States, 6565. doi:10.1117/12.719755.

[40] Han, Y., Choi, J., Jung, J., Chang, A., Oh, S., & Yeom, J. (2019). Automated Coregistration of Multisensor Orthophotos Generated from Unmanned Aerial Vehicle Platforms. Journal of Sensors, 1-10. doi:10.1155/2019/2962734

[41] Hyperspectral Imaging. (2020, April). Retrieved from https://www.imec-int.com/en/hyperspectral-imaging

[42] SpectralDevice. (2020, April). Retrieved from https://www.spectraldevices.com/

[43] Ocean Insight. (2020, April). Retrieved from https://www.oceaninsight.com/products/

[44] de Lang, H., Bouwhuis, G. (1965). U.S. Patent No. 3202039. Washington, DC: U.S. Patent and Trademark Office.

[45] Lapray, P.-J., Wang, X., Thomas, J.-B., Gouton, P. (2014). Multispectral Filter Arrays: Recent Advances and Practical Implementation. Sensors, 14, 21626-21659. doi:10.3390/s141121626

[46] Matchett, J. D., Billmers, R. I., Billmers, E. J., & Ludwig, M. E. (2007). Volume holographic beam splitter for hyperspectral imaging applications. Proc. SPIE, United States, 6668. doi:10.1117/12.733778.

[47] Ebbesen, T., Lezec, H., Ghaemi, H., Thio, T. & Wolff, P. A. (1998). Extraordinary optical transmission through sub-wavelength hole arrays. Nature, 391, 667–669. doi:10.1038/35570

[48] Bethe, H. A. (1944). Theory of diffraction by small holes. Phys. Rev, 66, 163. doi:10.1103/PhysRev.66.163

[49] Diest, K., Dionne, J. A., Spain, M., & Atwater, H. A. (2009). Tunable Color Filters Based on Metal−Insulator−Metal Resonators. Nano Lett, 9(7), 2579-2583. doi:10.1021/nl900755b

[50] Jen, Y.-J., Lakhtakia, A., Lin, M.-J., Wang, W.-H., Wu, H.-M., & Liao, H.-S. (2013). Metal/dielectric/metal sandwich film for broadband reflection reduction. Sci Rep, 3, 1672. doi:10.1038/srep01672

[51] Medvedev, V. V., Gubarev, V. M., & Lee, C. J. (2018). Optical performance of a dielectric-metal-dielectric antireflective absorber structure. J. Opt. Soc. Am. A, 35, 1450-1456. doi:10.1364/JOSAA.35.001450

[52] Li, Q., Li, Z., Xiang, X., Wang, T., Yang, H., Wang, X., Gong, Y., & Gao, J. (2019). Tunable Perfect Narrow-Band Absorber Based on a Metal-Dielectric-Metal Structure. Coatings, 9, 393. doi:10.3390/coatings9060393

[53] Loh, J.Y.Y., & Kherani, N. Design of Nano-Porous Multilayer Antireflective Coatings. Coatings 2017, 7, 134. doi:10.3390/coatings7090134

[54] Matsuoka, Y., Mathonnèire, S., Peters, S., & Masselink, W.T. (2018). Broadband multilayer anti-reflection coating for mid-infrared range from 7 µm to 12 µm. Appl. Opt, 57, 1645–1649. doi:10.1364/AO.57.001645

[55] Li, Z., Li, Q., Quan, X., Zhang, X., Song, C., Yang, H., Wang, X., & Gao, J. (2019). Broadband High-Reflection Dielectric PVD Coating with Low Stress and High Adhesion on PMMA. Coatings, 9, 237. doi:10.3390/coatings9040237

[56] Hu, C., Liu, J., Wang, J., Gu, Z., Li, C., Li, Q., Li, Y., Zhang, S., Bi, C., Fan, X. & Zheng, W. (2018). New design for highly durable infrared-reflective coatings. Light Sci. Appl, 7, 17175. doi:10.1038/lsa.2017.175

[57] Pimenta, S., Cardoso, S., Miranda, A., De Beule, P., Castanheira, E.M.S., & Minas, G. (2015). Design and fabrication of SiO2/TiO2 and MgO/TiO2 based high selective optical filters for diffuse reflectance and fluorescence signals extraction. Biomed. Opt. Express, 6, 3084-3098. doi:10.1364/BOE.6.003084

[58] Jen, Y.-J., Lee, C.-C., Lu, K.-H., Jheng, C.-Y., & Chen, Y.-J. (2015). Fabry-Perot based metal-dielectric multilayered filters and metamaterials. Opt. Express, 23, 33008-33017. doi:10.1364/BOE.6.003084

[59] Williams, C., Gordon, G. S. D., Wilkinson, T. D. & Bohndiek, S. E. (2019). Grayscale-to-Color: Scalable Fabrication of Custom Multispectral Filter Arrays. ACS Photonics, 6, 12, 3132–3141. doi:10.1021/acsphotonics.9b01196

[60] Joannopoulos, J. D., Johnson, S. G., Winn, J. N., & Meade, R. D. (2008). Photonic Crystals: Molding the Flow of Light (2nd. ed.). Princeton University Press.

[61] Ojha, S.P., Srivastava, S. K., Kumar, N., & Srivastava, S.K. (2004). Design of an optical filter using photonic band gap material. Optik, 114(3). doi:10.1078/0030-4026-00234

[62] Qian, Q., Xu, C., & Wang, C. (2017). All-dielectric polarization-independent optical angular filter. Sci Rep, 7, 16574. doi:10.1038/s41598-017-16837-w

[63] Scalora, M., Bloemer, M. J., Pethel, A. S., Dowling, J. P., Bowden, C. M., & Manka, A. S. (1998). Transparent, metallo-dielectric, one-dimensional, photonic band-gap structures. Journal of Applied Physics, 83(5), 2377-2383. doi:10.1063/1.366996

[64] Cushing, D. H. (1997). U.S. Patent No. 6018421A. Washington, DC: U.S. Patent and Trademark Office.

[65] Cushing, D. H. (1996). U.S. Patent No. 5926317A. Washington, DC: U.S. Patent and Trademark Office.

[66] Cushing, D. H. (1997). U.S. Patent No. 6011652A. Washington, DC: U.S. Patent and Trademark Office.

[67] Cushing, D. H. (1995). U.S. Patent No. 5999322A. Washington, DC: U.S. Patent and Trademark Office.

[68] Tsai, R., Lin, H., Chen, Y., Chang, C. (2000). U.S. No. 20020080493A1. Washington, DC: U.S. Patent and Trademark Office.

[69] Lewis, K. L. (1999). U.S. Patent No. 6631033B1. Washington, DC: U.S. Patent and Trademark Office.

[70] Kundu, A. C. (2005). U.S. Patent No. 7312676B2. Washington, DC: U.S. Patent and Trademark Office.

[71] Wang, S. S., & Magnusson, R. (1993). Theory and applications of guided-mode resonance filters. Appl. Opt, 32, 2606-2613. doi:10.1364/AO.32.002606

[72] Sharon, A., Rosenblatt, D., & Friesem, A. A. (1996). Narrow spectral bandwidths with grating waveguide structures. Appl. Phys. Lett, 69, 4154. doi:10.1063/1.116969

[73] Tibuleac, S., & Magnusson, R. (2011). Narrow-linewidth bandpass filters with diffractive thin-film layers. Opt. Lett, 26, 584-586. doi:10.1364/OL.26.000584

[74] Tibuleac, S., & Magnusson, R. (1997). Reflection and transmission guided-mode resonance filters. J. Opt. Soc. Am. A, 14, 1617-1626. doi:10.1364/JOSAA.14.001617

[75] Babu, S., & Lee, J.-B. (2019). Axially-Anisotropic Hierarchical Grating 2D Guided-Mode Resonance Strain-Sensor. Sensors, 19, 5223. doi:10.3390/s19235223

[76] Kuo, W., & Hsu, C. (2017). Two-dimensional grating guided-mode resonance tunable filter. Opt. Express, 25, 29642-29649. doi:10.1364/OE.25.029642

[77] Ren, Z., Sun, Y., Zhang, S., Zhang, K., Lin, Z., & Wang, S. (2018). 2D non-polarising transmission filters based on GMR for optical communications. Micro & Nano Letters, 13(11), 1621-1626. doi:10.1049/mnl.2018.5115

[78] Cao, L., Fan, P., Barnard, E. S., Brown, A. M., & Brongersma, M. L. (2010). Tuning the Color of Silicon Nanostructures. Nano Lett, 10(7), 2649-2654. doi:10.1021/nl1013794

[79] Park, H., Seo, K., & Crozier, K. B. (2012). Adding colors to polydimethylsiloxane by embedding vertical silicon nanowires. Appl. Phys. Lett, 101, 193107. doi:10.1063/1.4766944

[80] Park, H., Crozier, K. (2013). Multispectral imaging with vertical silicon nanowires. Sci Rep, 3, 2460. doi:10.1038/srep02460

[81] Song, H.S., Lee, G.J., Yoo, D.E., Kim, Y. J., Yoo, Y. J., Lee, D.-W., Siva, V., Kang, I.-S., & Song, Y. M. (2019). Reflective color filter with precise control of the color coordinate achieved by stacking silicon nanowire arrays onto ultrathin optical coatings. Sci Rep, 9, 3350. doi:10.1038/s41598-019-40001-1

[82] Cao, L., Fan, P., Barnard, E. S., Brown, A. M., & Brongersma, M. L. (2010). Filter-Free Image Sensor Pixels Comprising Silicon Nanowires with Selective Color Absorption. Nano Lett, 10(7), 2649-2654. doi:10.1021/nl404379w

[83] N, D., J, W., M, P., I, K., WS, W., & SS, S. (2016). Adjustable optical response of amorphous silicon nanowires integrated with thin films. Nanotechnology, 27(14), 145703. doi:10.1088/0957-4484/27/14/145703

[84] Maier, S. A. (2007). Plasmonics - Fundamentals and Applications. (1st. ed.). Springer.

[85] Porto, J. A., García-Vidal, F. J., & Pendry, J. B. (1999). Transmission Resonances on Metallic Gratings with Very Narrow Slits. Phys. Rev. Lett, 83, 2845. doi:10.1103/PhysRevLett.83.2845

[86] Xu, T., Wu, Y., Luo, X., & Guo, L. J. (2010). Plasmonic nanoresonators for high-resolution colour filtering and spectral imaging. Nat Commun, 1(59). doi:10.1038/ncomms1058

[87] Lee, H.-S. Yoon, Y.-T., Lee, S.-S., Kim, S.-H., & Lee, K.-D. (2007). Color filter based on a subwavelength patterned metal grating. Opt. Express, 15, 15457-15463. doi:10.1364/OE.15.015457

[88] Fleischman, D., Sweatlock, L. A., Murakami, H., & Atwater, H. (2017). Hyper-selective plasmonic color filters. Opt. Express, 25, 27386-27395. doi:10.1364/OE.25.027386

[89] Fleischman, D., Fountaine, K. T., Bukowsky, C. R., Tagliabue, G., Sweatlock, L. A., & Atwater, H.A. (2019). High Spectral Resolution Plasmonic Color Filters with Subwavelength Dimensions. ACS Photonics, 6(2) 332-338. doi:10.1021/acsphotonics.8b01634

[90] Mazulquim, D. B., Lee, K. J., Yoon, J. W., Muniz, L. V., Borges, B.-H. V., Neto, L. G., & Magnusson, R. (2014). Efficient band-pass color filters enabled by resonant modes and plasmons near the Rayleigh anomaly. Opt. Express, 22, 30843-30851. doi:10.1364/OE.22.030843

[91] He, X., Liu, Y., Ganesan, K., Ahnood, A., Beckett, P., Eftekhari, F., Smith, D., Md Uddin, H., Skafidas, E., Nirmalathas, A., & Unnithan, R. R. (2020). A single sensor based multispectral imaging camera using a narrow spectral band color mosaic integrated on the monochrome CMOS image sensor. APL Photonics, 5(4) 046104. doi:10.1063/1.5140215

[92] Yokogawa, S., Burgos, S. P., and Atwater, H. A. (2012). Plasmonic Color Filters for CMOS Image Sensor Applications. Nano Lett, 12(8), 4349-4354. doi:10.1021/nl302110z

[93] Burgos, S. P., Yokogawa, S., & Atwater, H. A. (2013). Color Imaging via Nearest Neighbor Hole Coupling in Plasmonic Color Filters Integrated onto a Complementary Metal-Oxide Semiconductor Image Sensor. ACS Nano, 7(11), 10038-10047. doi:10.1021/nn403991d

[94] Chen, Q., & Cumming, D. R. S. (2010). High transmission and low color cross-talk plasmonic color filters using triangular-lattice hole arrays in aluminum films. Opt. Express, 18, 14056-14062. doi:10.1364/OE.18.014056

[95] Najiminaini, M., Vasefi, F., Kaminska, B., & Carson, J. J. L. (2013). Nanohole-array-based device for 2D snapshot multispectral imaging. Sci Rep, 3, 2589. doi:10.1038/srep02589

[96] Jang, W., Ku, Z., Jeon, J., Kim, J. O., Lee, S. J., Park, J., Noyola, M. J., & Urbas, A. (2016). Experimental Demonstration of Adaptive Infrared Multispectral Imaging using Plasmonic Filter Array. Sci Rep, 6, 34876. doi:10.1038/srep34876

[97] Manjavacas, A., & García de Abajo, F. J. (2014). Tunable plasmons in atomically thin gold nanodisks. Nat. Commun, 5,3548. doi:10.1038/ncomms4548

[98] Langhammer, C., Schwind, M., Kasemo, B., & Zorić, I. (2008). Localized Surface Plasmon Resonances in Aluminum Nanodisks. Nano Lett, 8(5), 1461-1471. doi:10.1021/nl080453i

[99] Clausen, J. S., Højlund-Nielsen, E., Christiansen, A. B., Yazdi, S., Grajower, M., Taha, H., Levy, U., Kristensen, A., & Mortensen, N. A. (2014). Plasmonic Metasurfaces for Coloration of Plastic Consumer Products. Nano Lett, 14(8), 4499-4504. doi:10.1021/nl5014986

[100] Ye, M., Sun, L., Hu, X., Shi, B., Zeng, B., Wang, L., Zhao, J., Yang, S., Tai, R., Fecht, H.-J., Jiang, J.-Z., & Zhang, D.-X. (2015). Angle-insensitive plasmonic color filters with randomly distributed silver nanodisks. Opt. Lett, 40, 4979-4982. doi:10.1364/OL.40.004979

[101] Chua, K. C., Chao, C. Y., & Chen, Y. F. (2006). Electrically controlled surface plasmon resonance frequency of gold nanorods. Appl. Phys. Lett, 89, 103107. doi:10.1063/1.2335812

[102] Zhang, J., ElKabbash, M., Wei, R., Singh, S. C., Lam, B., & Guo, C. (2019). Plasmonic metasurfaces with 42.3% transmission efficiency in the visible. Light Sci Appl, 8, 53. doi:10.1038/s41377-019-0164-8

[103] Heshmat, B., Li, D., Darcie, T. E., & Gordon, R. (2011). Tuning plasmonic resonances of an annular aperture in metal plate. Opt. Express, 19, 5912-5923. doi:10.1364/OE.19.005912

[104] Salvi, J., Roussey, M., Baida, F. I., Bernal, M.-P., Mussot, A., Sylvestre, T., Maillotte, H., Van Labeke, D., Perentes, A., Utke, I., Sandu, C., Hoffmann, P., & Dwir, B. (2005). Annular aperture arrays: study in the visible region of the electromagnetic spectrum. Opt. Lett, 30, 1611-1613. doi:10.1364/OL.30.001611

[105] Si, G., Zhao, Y., Liu, H., Teo, S., Zhang, M., Huang, T. J., Danner, A. J., & Teng, J. (2011). Annular aperture array based color filter. Appl. Phys. Lett, 99, 033105. doi:10.1063/1.3608147

[106] Lyon, R. F. & Hubel, P. M. Eyeing the camera: Into the next century. In Color and Imaging Conference, 2002, pp. 349-355. Foveon X3 camera technology.

[107] Duempelmann, L., Gallinet, B., & Novotny, L. (2017). Multispectral Imaging with Tunable Plasmonic Filters. ACS Photonics, 4(2), 236-241. doi:10.1021/acsphotonics.6b01003

[108] Rodríguez-de Marcos, L. V., Larruquert, J. I., Méndez, J. A., & Aznárez, J. A. (2016). Self-consistent optical constants of SiO_2 and Ta_2O_5 films. Opt. Mater. Express, 6, 3622-3637. doi.10.1364/OME.6.003622

[109] Knight, M. W., King, N. S., Liu, L., Everitt, H. O., Nordlander, P., & Halas, N. J. (2014). Aluminum for Plasmonics. ACS Nano, 8(1), 834-840. doi:10.1021/nn405495q

[110] Ji, C., Lee, K.-T., Xu, T., Zhou, J., Park, H. J., & Guo, L. J. (2017). Engineering Light at the Nanoscale: Structural Color Filters and Broadband Perfect Absorbers. Advanced Optical Materials, 5, 1700368. doi:10.1002/adom.201700368

[111] Todeschini, M., da Silva Fanta, A. B., Jensen, F., Wagner, J. B., & Han, A. (2017). Influence of Ti and Cr Adhesion Layers on Ultrathin Au Films. ACS Appl. Mater. Interfaces, 9(42), 37374-37385. doi:10.1021/acsami.7b10136

[112] The finite element method. (2020, April). Retrieved from https://www.comsol.com/multiphysics/finite-element-method

[113] RF module user's guide. (2020, April). Retrieved from https://doc.comsol.com/5.5/doc/com.comsol.help.rf/RFModuleUsersGuide.pdf

[114] Broers, A. N., Hoole, A. C. F., & Ryan, J. M. (1996). Electron beam lithography—Resolution limits. Microelectronic Engineering, 32, 1–4. doi:10.1016/0167-9317(95)00368-1.

[115] Lee, K. W. (2009). Secondary electron generation in electron-beam-irradiated solids:resolution limits to nanolithography. J. Kor. Phys. Soc, 55 (4), 1720. doi:10.3938/jkps.55.1720

[116] Holzner, F., Paul, P., Zientek, M., Knoll, A., Rawlings, C. (2013). U.S. Patent. No. 10209630B2. Washington, DC: U.S. Patent and Trademark Office.

[117] Wolf, H., Rawlings, C., Mensch, P., Hedrick, J. L., Coady, D. J., Duerig, U., & Knoll, A. W. (2015). Sub-20 nm silicon patterning and metal lift-off using thermal scanning probe lithography. Journal of Vacuum Science & Technology B, 33(2). doi:10.1116/1.4901413.

[118] NanoFrazor Explore. (2020, April). Retrieved from https://heidelberg-instruments.com/en/products/nanofrazor-explore.html

[119] Burnett, T. L., Kelley, R., Winiarski, B., Contreras, L., Daly, M., Gholinia, A., Burke, M. G., & Withers, P. J. (2016). Large volume serial section tomography by Xe Plasma FIB dual beam microscopy. Ultramicroscopy, 161, 119–129. doi:10.1016/j.ultramic.2015.11.001.

[120] Orloff, J. (1996). Fundamental limits to imaging resolution for focused ion beams. Journal of Vacuum Science and Technology B, 14 (6), 3759. doi:10.1116/1.588663

[121] Sterling, H. F., Swann, R.C.G. (1965). Chemical vapour deposition promoted by r.f. discharge. Solid-State Electronics, 8(8), 653–654. doi:10.1016/0038-1101(65)90033-X.

[122] K. Ishii (1989). High-rate low kinetic energy gas-flow-sputtering system. Journal of Vacuum Science and Technology A, 7 (2): 256–258. doi:10.1116/1.576129.

[123] McMullan, D. (2006). Scanning electron microscopy 1928–1965. Scanning, 17(3) 175–185. doi:10.1002/sca.4950170309.

[124] Hirsch, P., Kässens, M., Püttmann, M. and Reimer, L. (1994), Contamination in a scanning electron microscope and the influence of specimen cooling. Scanning, 16: 101-110. doi:10.1002/sca.4950160207.

[125] Bennig, G. K. (1986). U.S. Patent. No. 4724318. Washington, DC: U.S. Patent and Trademark Office.

[126] Rothen, A. (1945). The Ellipsometer, an Apparatus to Measure Thickness of Thin Surface Films. Rev. Sci. Instrum, 16(2), 26. doi:10.1063/1.1770315.

[127] Chen, Q., Chitnis, Walls, D. K., Drysdale, T. D., Collins, S., & Cumming, D. R. S. (2012). CMOS photodetectors integrated with plasmonic color filters. IEEE Photonics Technol. Lett, 24(3), 197–199. doi: 10.1109/LPT.2011.2176333.

[128] Dai, Q., Rajasekharan, R., Butt, H., Won, K., & Wang, X. Z. (2011). Transparent liquid-crystal-based microlens array using vertically aligned carbon nanofiber electrodes on quartz substrates. Nanotechnology, 22(11). doi:10.1088/0957-4484/22/11/115201.

[129] Rajasekharan, R., Wilkinson, T. D., Hands, P. J. W., & Dai, Q. (2011). Nanophotonic Three-Dimensional Microscope. Nano Lett, 11(7), 2770-2773. doi:10.1021/nl201056s.

[130] Rajasekharan, R., Bay, C., Dai, Q., Freeman, J., & Wilkinson, T. D. (2010). Electrically reconfigurable nanophotonic hybrid grating lens array. Appl. Phys. Lett, 96, 233108. doi:10.1063/1.3449130.

[131] Yang, B., Liu, W. W., Li, Z. C., Cheng, H., Chen, S. Q., & Tian, J. G. (2018). Polarization-Sensitive Structural Colors with Hue-and-Saturation Tuning Based on All-Dielectric Nanopixels. Adv. Optical Mater, 6, 1701009. doi:10.1002/adom.201701009.

[132] Sun, L. B., Hu, X. L., Zeng, B. B., Wang, L. S., Yang, S. M., Tai, R. Z., Fecht, H. J., Zhang, D. X., & Jiang, J. Z. (2015). Effect of relative nanohole position on colour purity of ultrathin plasmonic substractive colour filters. Nanotechnology, 26 (30). doi:10.1088/0957-4484/26/30/305204.

[133] Genet, C., & Ebbesen, T. W. (2007). Light in tiny holes. Nature, 445, 39-46.

doi:10.1038/nature05350.

[134] Inoue, D., Miura, A., Nomura, T., Fujikawa, H., Sato, K., Ikeda, N., Tsuya, D., Sugimoto, Y., & Koide, Y. (2011). Polarization independent visible color filter comprising an aluminum film with surface-plasmon enhanced transmission through a subwavelength array of holes. Appl. Phys. Lett, 98, 093113. doi:10.1063/1.3560467.

[135] Liu, W., Sukhorukov, A., Miroshnichenko, A., Poulton, C., Xu, Z. Y., Neshev, D., & Kivshar, Y. (2010). Complete spectral gap in coupled dielectric waveguides embedded into metal. Appl. Phys. Lett, 97, 021106. doi:10.1063/1.3458694.

[136] Lee, H. S., Yoon, Y. T., Lee, S. S., Kim, S. H., & Lee, K. D. (2007). Color filter based on a subwavelength patterned metal grating. Opt. Express, 15(23), 15457–15463. doi:10.1364/OE.15.015457.

[137] Lezec, H. J., & T. Thio. (2004). Diffracted evanescent wave model for enhanced and suppressed optical transmission through subwavelength hole arrays. Opt. Express, 12(16), 3629–3651. doi:10.1364/OPEX.12.003629.

[138] Balakrishnan, S., Najiminaini, M., Singh, M. R., & Carson, J. J. L. (2016). A study of angle dependent surface plasmon polaritons in nano-hole array structures. Journal of Applied Physics, 120, 034302. doi:10.1063/1.4958870.

[139] Zheng, B. Y., Wang, Y. M., Nordlander, P., & Halas, N. J. (2014). Color-Selective and CMOS-Compatible Photodetection Based on Aluminum Plasmonics. Advanced Materials, 26(36). doi.org/10.1002/adma.201401168.

[140] Zhang, X. N., Liu, G. Q., Liu, Z. Q., Cai, Z. J., Hu, Y., Liu, X. S., Fu, G. L., Gao, H. G., & Huang, S. (2015). Effects of Compound Rectangular Subwavelength Hole Arrays on Enhancing Optical Transmission. IEEE Photonics Journal, 7(1), 1-8. doi: 10.1109/JPHOT.2015.2402125.

[141] Wang, C. M., Huang, H. I., Chao, C. C., Chang, J. Y., & Sheng, Y. (2007). Transmission enhancement through a trench-surrounded nano metallic slit by bump reflectors. Opt. Express, 15(6). doi:10.1364/OE.15.003496.

[142] Lu, H., Liu, X. M., Gong, Y. K., Mao, D., & Wang, L. R. (2011). Enhancement of transmission efficiency of nanoplasmonic wavelength demultiplexer based on channel drop filters and reflection nanocavities. Opt. Express, 19(14). doi:10.1364/OE.19.012885.

[143] Li, Q., Du, K. K., Mao, K. N., Fang, X., Zhao, D., Ye, H., & Qiu, M. (2016). Transmission enhancement based on strong interference in metal-semiconductor layered film for energy harvesting. Sci. Rep, 6, 29195. doi:10.1038/srep29195.

[144] Setting excitation in 3D. (2017, August). Retrieved from http://srdjancomsol.weebly.com/setting-excitation-in-3d.html

[145] Palik, E. D. (1998). Handbook of Optical Constants. Academic Press.

[146] Diest, K., Dionne, J. A., Spain, M., & Atwater, H. A. (2009). Tunable Color Filters Based on Metal−Insulator−Metal Resonators. Nano Lett, 9(7), 2579-2583. doi:10.1021/nl900755b.

[147] Song, M., Wang, D., Peana, S., Choudhury, S., Nyga, P., Kudyshev, Z. A., Yu, H., Boltasseva, A., Shalaev, V. M., & Kildishev, A. V. (2019). Colors with plasmonic nanostructures: A full-spectrum review. Applied Physics Reviews, 6, 041308. doi:10.1063/1.5110051.

[148] RGB VERSUS CMY COLOR IMAGERY. (2020, Jan). Retrieved from http://www.astrosurf.com/buil/us/cmy/cmy.htm

[149] Shrestha, V. R., Lee, S.-S., Kim, E.-S., & Choi, D.-Y. (2014). Aluminum Plasmonics Based Highly Transmissive Polarization-Independent Subtractive Color Filters Exploiting a Nanopatch Array. Nano Lett, 6672-6678. doi:10.1021/nl503353z.

[150] Yang, C., Shen, W., Zhou, J., Fang, X., Zhao, D., Zhang, X., Ji, C., Fang, B., Zhang, Y., Liu, X., & Guo, L.J. (2016). Angle Robust Reflection/Transmission Plasmonic Filters Using Ultrathin Metal Patch Array. Advanced Optical Materials, 4, 1981-1986. doi:10.1002/adom.201600397.

[151] Wu, Y., Hollowell, A., Zhang, C., & Guo, L. J. (2013). Angle-Insensitive Structural Colours based on Metallic Nanocavities and Coloured Pixels beyond the Diffraction Limit. Sci Rep, 3, 1194. doi:10.1038/srep01194.

[152] Yue, W., Gao, S., Lee, S., Kim E.-S., & Choi D.-Y. (2016). Subtractive Color Filters Based on a Silicon-Aluminum Hybrid-Nanodisk Metasurface Enabling Enhanced Color Purity. Sci Rep, 6, 29756. doi:10.1038/srep29756.

[153] Cheng, F., Gao, J., Stan, L., Rosenmann, D., Czaplewski, D., & Yang, X. (2015). Aluminum plasmonic metamaterials for structural color printing. Opt. Express, 23, 14552-14560. doi:10.1364/OE.23.014552.

[154] Yang, C., Shen, W., Zhang, Y., Peng, H., Zhang, X., & Liu, X. (2014). Design and simulation of omnidirectional reflective color filters based on metal-dielectric-metal structure. Opt. Express, 22, 11384-11391. doi:10.1364/OE.22.011384.

[155] Wang, H., Wang, X., Yan, C., Zhao, H., Zhang, J., Santschi, C., & Martin, O. J. F. (2017). Full Color Generation Using Silver Tandem Nanodisks. ACS Nano, **11** (5), 4419-4427. doi:10.1021/acsnano.6b08465.

[156] Desert Spin-On Glass. (2020, Jan). Retrieved from http://desertsilicon.com/spin-on-glass/

[157] Pakizeh, T., Dmitriev, A., Abrishamian, M. S., Granpayeh, N., & Käll, M. (2008). Structural asymmetry and induced optical magnetism in plasmonic nanosandwiches. J. Opt. Soc. Am. B, 25, 659-667. doi:10.1364/JOSAB.25.000659.

[158] Rakić, A. D. (1995). Algorithm for the determination of intrinsic optical constants of metal films: application to aluminum. Appl. Opt, 34, 4755-4767. doi:10.1364/AO.34.004755.

[159] Tang, J., Cao, Q., Tulevski, G., Jenkins, K. A., Nela, L., Farmer, D. B., & Han, S. (2018). Flexible CMOS integrated circuits based on carbon nanotubes with sub-10 ns stage delays. Nat Electron, 1, 191–196. doi:10.1038/s41928-018-0038-8.

[160] Bariya, M., Nyein, H. Y. Y., & Javey, A. (2018). Wearable sweat sensors. Nat Electron, 1, 160–171. doi:10.1038/s41928-018-0043-y.

[161] Sugie, T., Akamatsu, T., Nishitsuji, T., Hirayama, R., Masuda, N., Nakayama, H., Ichihashi, Y., Shiraki, A., Oikawa, M., Takada, N., Endo, Y., Kakue, T., Shimobaba, T., & Ito, T. (2018). High-

performance parallel computing for next-generation holographic imaging. Nat Electron, 1, 254–259. doi:10.1038/s41928-018-0057-5.

[162] Fan, Z., Qiu, H., Zhang, H., Pang, X., Zhou, L., Liu, L., Ren, H., Wang, Q., & Dong, J. (2019). A broadband achromatic metalens array for integral imaging in the visible. Light Sci Appl, 8, 67. doi:10.1038/s41377-019-0178-2.

[163] Lebourgeois, V., Bégué, A., Labbé, S., Mallavan, B., Prévot, L., & Roux, B. (2008). Commercial Digital Cameras Be Used as Multispectral Sensors? A Crop Monitoring Test. Sensors (Basel), 8, 7300–7322. doi:10.3390/s8117300.

[164] Chang, Y., Hu, Y., Chen, Z., & Xing, D. (2019). Co-impulse multispectral photoacoustic microscopy and optical coherence tomography system using a single supercontinuum laser. Opt. Lett, 44, 4459-4462. doi:10.1364/OL.44.004459.

[165] Zhao, X., Zhang, J., Yang, C., Song, H., Shi, Y., Zhou, X., Zhang, D., & Zhang, G. (2018). Registration for Optical Multimodal Remote Sensing Images Based on FAST Detection, Window Selection, and Histogram Specification. Remote Sens, 10, 663. doi:10.3390/rs10050663.

[166] Rajasekharan, R., Butt, H., Dai, Q., Wilkinson, T. D., & Amaratunga, G. A. J. (2012). Can nanotubes make a lens array? Advanced materials, 24 (23), OP170-OP173. doi:10.1002/adma.201200296.

[167] Butt, H., Dai, Q., Rajasekharan, R., Wilkinson, T. D., & Amaratunga, G. A. J. (2011). Enhanced reflection from arrays of silicon based inverted nanocones. Applied Physics Letters, 99 (13), 133105. doi:10.1063/1.3633119.

[168] Rajasekharan, R., Dai, Q., & Wilkinson, T. D. (2010). Electro-optic characteristics of a transparent nanophotonic device based on carbon nanotubes and liquid crystals. Applied optics, 49 (11), 2099-2104. doi:10.1364/AO.49.002099.

[169] Ding, Y., & Magnusson, R. (2004). Resonant leaky-mode spectral-band engineering and device applications. Optics Express, 5661-5674. doi:10.1364/OPEX.12.005661.

[170] Uddin, M. J., Khaleque, T., & Magnusson, R. (2014). Guided-mode resonant polarization-controlled tunable color filters. Opt. Express, 22, 12307-12315. doi:10.1364/OE.22.012307.

[171] Duan, X., Kamin, S., & Liu, N. (2017). Dynamic plasmonic colour display. Nat Commun, 8, 14606. doi:10.1038/ncomms14606.

[172] Sautter, J., Staude, I., Decker, M., Rusak, E., Neshev, D. N., Brener, I., & Kivshar, Y. S. (2015). Active Tuning of All-Dielectric Metasurfaces. ACS Nano, 9(4), 4308-4315. doi:10.1021/acsnano.5b00723.

[173] Yoon, Y., Park, C., & Lee, S. (2012). Highly Efficient Color Filter Incorporating a Thin Metal–Dielectric Resonant Structure. Appl. Phys. Express, 5, 2. doi:10.1143/apex.5.022501.

[174] Zheng, B. Y., Wang, Y., Nordlander, P., & Halas, N. J. (2014). Color-selective and CMOS-compatible photodetection based on aluminum plasmonics. Adv. Mater, 26, 6318-6323. doi:10.1002/adma.201401168.

[175] HYPER SPECTRAL IMAGING. (2020, April). Retrieved from https://www.ximea.com/support/attachments/4675/XIMEA_imec_HSI_technology-Part-V1.1.pdf

Appendix

This appendix presents a new mass producible (using photolithography and metal deposition) narrow band filter technology suitable for multispectral camera system development. The design and fabrication details are kept as a trade secret due to a startup formed called PIXsensor.

1. Introduction

The current multispectral imaging system (MIS) has the following disadvantages: power hungry, bulk size and have image co-registration problem for some applications, such as aerial imaging. For example, 6 bands tetracam MIS has the size of 131.4 x 78.3 x 87.6 mm, and weight of 600g and power requirement of 21 W [1]. Therefore, these disadvantages greatly limits its applications. Current single sensor based multispectral cameras in the market was presented in Chapter 1, their filter technology was confidential. It can be predicted from many US patents and literatures, their filter structures are based on the multilayer coating, and the number of layers is usually more than ten as shown in Chapter 1. The whole filter array fabrication requires multiple stages with mask alignment, making the fabrication cost. The single sensor based multispectral camera with single exposure fabrication was demonstrated in Chapter 4, which only requires maskless nanolithography technology to fabricate the whole filter array, and the minimum spectral width (FWHM) in experiments is 45nm. This chapter would introduce novel filter structures based on the Fabry–Pérot theory. Even though the whole filter array fabrication still needs multiple stages and mask alignment, the minimum FWHM with experimental measurement is 17nm and the total number of layers is 5.

This chapter has two parts. In the first part, design and fabrication of large size narrow band pass wavelength filters operating at different wavelengths is presented based on the metal-dieletric multilayer approach. Secondly, single sensor based multispectral camera (design and fabrication of narrow band pass filters mosaic and their integration technique on an image sensor for making multispectral camera) using the above recipe with photolithography (mass producible, used in chip fabrication) is presented.

2. Design and Fabrication of Large Size Narrow Bandpass Wavelength Filters

2.1 Simulation Methods and Results

Optical bandpass filter permits a simple and novel technology with E-beam evaporator which is based on thin film deposition of the common materials (e.g. TiO_2, SiO_2 and Au) to produce band pass filters with low cost, narrow bandwidth and sufficient transmission percentage. Our current capability allows us to produce and tune to any wavelength from 400 nm to 1200 nm. Additional work will allow us to be able to produce and tune to any wavelength between 1 microns and 14 microns to make filters in the mid -infrared region.

The working principle of our proposed optical filter is based on two major theory. As the literature points out that an adhesion layer (seed layer) is critical for depositing materials like Au/ Ag on substrates. Materials with current adhesion methods can produce a range of optical performance. Most of the researchers use Cr, Ti and Ge to increase the adhesion. However, it has been proved that the adhesion layer of thickness (even 2-5 nm) will significantly increases the bandwidth and therefore reduce the optical performance. Hence these materials could be replaced by optical grade material

Titanium Oxide, which not only has different refractive index with different oxygen density during the deposition, but also could stick both on quartz (or glass) and metals (Au, Ag, Al).

For dielectric based Fabry-Perot, the thickness of mirror and cavity is determined by their refractive index with relationship: $\mathrm{n_1 \times l_1 = n_2 \times l_2}$, where $\mathrm{n_1}$ and $\mathrm{n_2}$ is the refractive index of mirror and cavity, $\mathrm{l_1}$ and $\mathrm{l_2}$ is the thickness of mirror and cavity. Furthermore, the thickness of mirror depends on the desired peak wavelength, $\lambda = 4\mathrm{n_1 l_1}$. When using metal instead of dielectric for the mirror, the refractive index of metal has both real and imaginary part and is defined as: $\mathrm{n_1 = n + ki}$. Then the suitable thickness for mirror and cavity can be determined as: $\mathrm{|n_1| \times l_1 = n_2 \times l_2}$, $\sqrt{n^2 + k^2} \times \mathrm{l_1 = n_2 \times l_2}$. The equation above is effective when ignoring the adhesion layer thickness. To incorporate the effect of adhesion layer, simulation software COMSOL is used to find the peak wavelength. The large difference between the refractive index of mirror and cavity introduces smaller bandwidth. As Au cannot adhere on most material, during this work, when using Silicon Dioxide as the cavity material, a thin 10nm Titanium Oxide has been deposited as well. The basic structure and results of our proposed optical filter in the visible and near IR range (VIS and NIR) are shown below (Figure A1). In the structure below, the thickness of metal is chosen as at least twice as its skin depth. The thickness of middle dielectric layer varies from 20nm to 200nm depends on the wavelength. Figure A2 shows the optical theory of Fabry–Pérot, that the incident light from the top is reflected several times and most of the electric field is concentrated in the cavity.

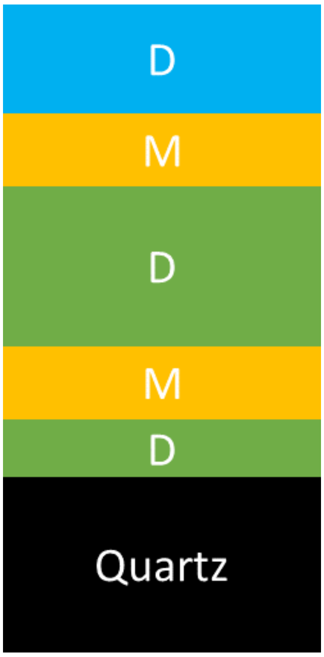

Figure A1 Proposed structures of optical bandpass filter.

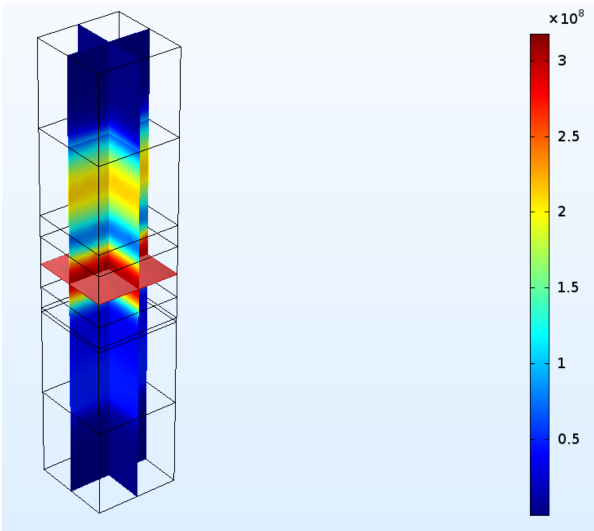

Figure A2 Electric strength distribution (V/m) of our designed filter

2.2 Experimental Results:

Bandpass filters operating in VIS and NIR region are shown below (Figure A3). The experimental measurements are also presented in Figure A4 and Table A1. The NIR filter performs better with minimum FWHM 17nm. With such simple structure, the fabrication complication and costs can be reduced significantly. Moreover, FWHM can be reduced further when the peak wavelength is shifted towards Mid IR wavelength (2.5µm). This will have more applications in the gas detection, healthcare and other research area.

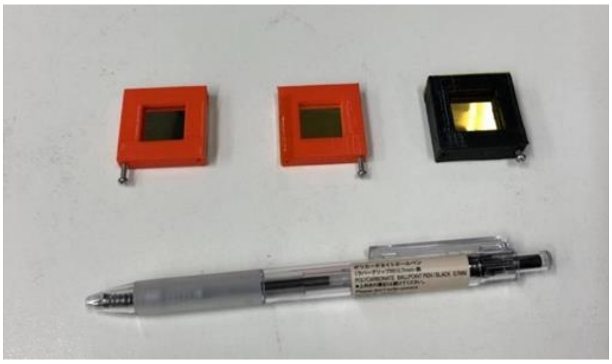

Figure A3 Optical bandpass filters with threads.

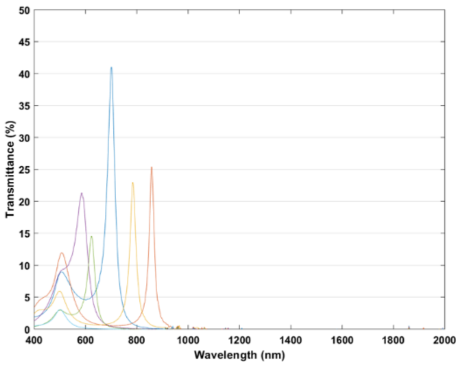

Figure A4 Experimentally measured transmission spectra of the VIS and NIR filters showing the narrow bandwidth.

Table A1 Experimental results of multispectral filters

Peak wavelength (nm)	**500**	**580**	**620**	**700**	**790**	**840**
FWHM (nm)	**55**	**40**	**25**	**20**	**19**	**17**

Later, the narrow bandpass filters are placed in front of a camera lens to image plants at different wavelength.

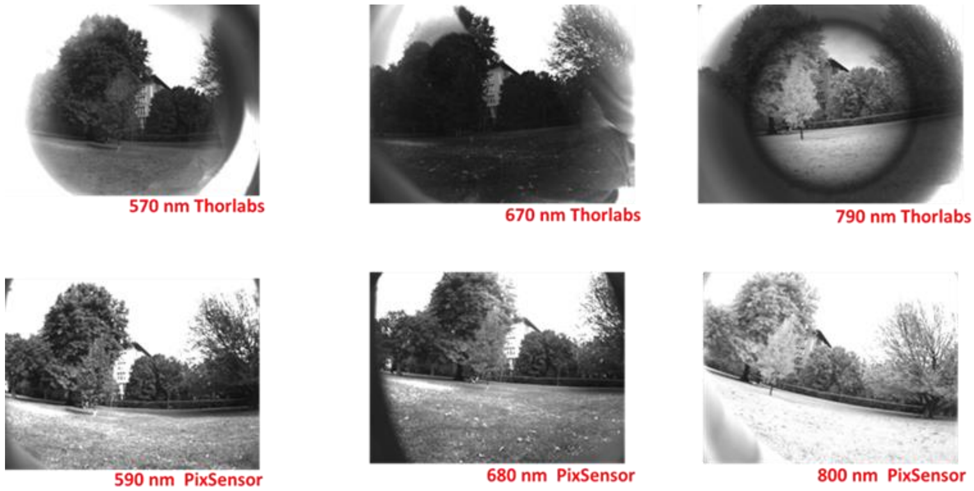

Figure A5 Comparison of the performance with our filters and Thorlabs [2] in agriculture application

The colour checker was also used to examine the performance of our bandpass filter. The following image shows optical bandpass filters for multispectral imaging. The standard Macbeth colour chart is used as a reference. The results from the individual colours is shown in the middle. A6 shows the results of different channel combinations from raw data that is a common image processing practice in the multispectral imaging applications.

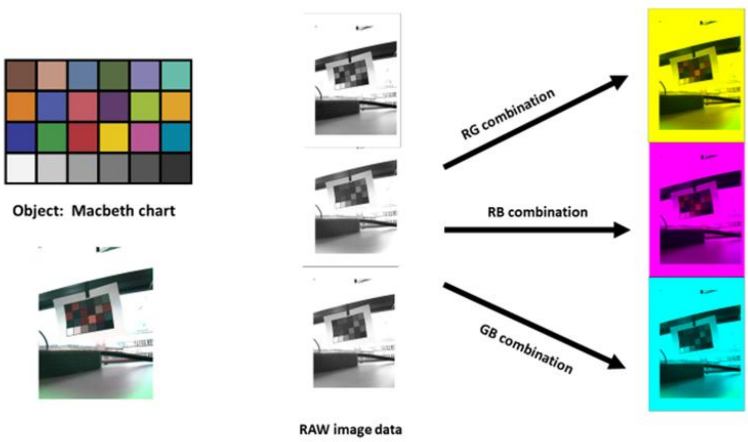

Figure A6 Colour imaging and band combination with PIXsensor bandpass filter

3. Single Sensor based Multispectral Camera

3.1 Design and Fabrication of Narrow Bandpass Filters Mosaic

The low-cost narrow wavelength mosaic filters was developed for use in single sensor based multispectral imaging. By using the Level-to-Level alignment technology with Direct Write Lithography, multiple filters could be deposited on a quartz substrate separately.

Furthermore, this multispectral narrow wavelength band pass filters mosaic can be integrated on a coin size image sensor with electronics after removing the protective glass on the sensor. Our designed multispectral filter on single sensor with different combinations are shown in Figure A7 and Figure A8.

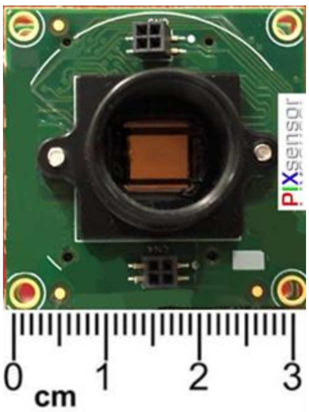

Figure A7 PIXsensor multispectral camera with 6 bands

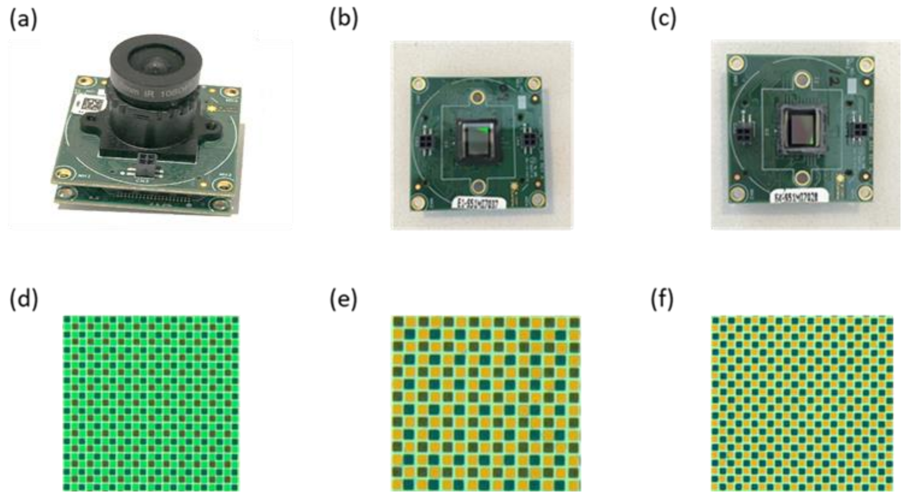

Figure A8 (a) the standard board camera that can be easily modified today. (b) CMOS image sensor board with protective glass on the sensor after removing the optics, (c) the same CMOS image sensor with the protective glass removed. Images D, E, and F are filters mosaic (d) a RGB multispectral filter, (e) Red+IR1 multispectral filter, (f) Red +IR1+IR2 multispectral filter.

3.2 Test with PIXsensor Multispectral Camera

Then the multispectral camera was used to image the plants in the University of Melbourne. Figure A9a is the environment taken with iphone 8 plus, where the left part trees are greener and healthier than those on the right part. Figure A9b is the multispectral raw image taken with 6 band multispectral camera. After using image processing to collect the images for each band, it can be seen the result is consistent with the theory, as healthy leaf emits more NIR than dead leaf, the left part is brighter for NIR images (800nm) in Figure A10.

(a) (b)

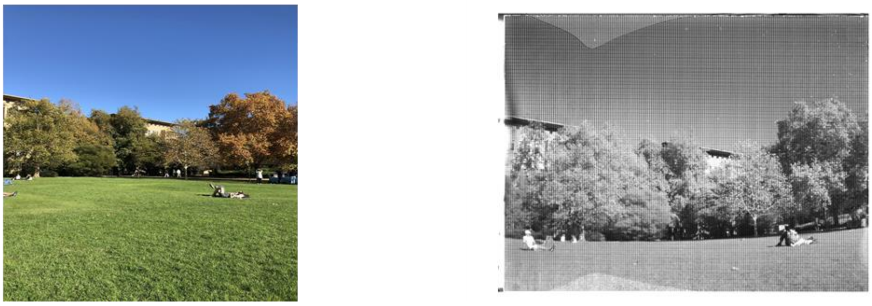

Figure A9 (a) Colour image taken with iphone 8 plus, (b) Raw image taken with 6 band PIXsensor multispectral camera.

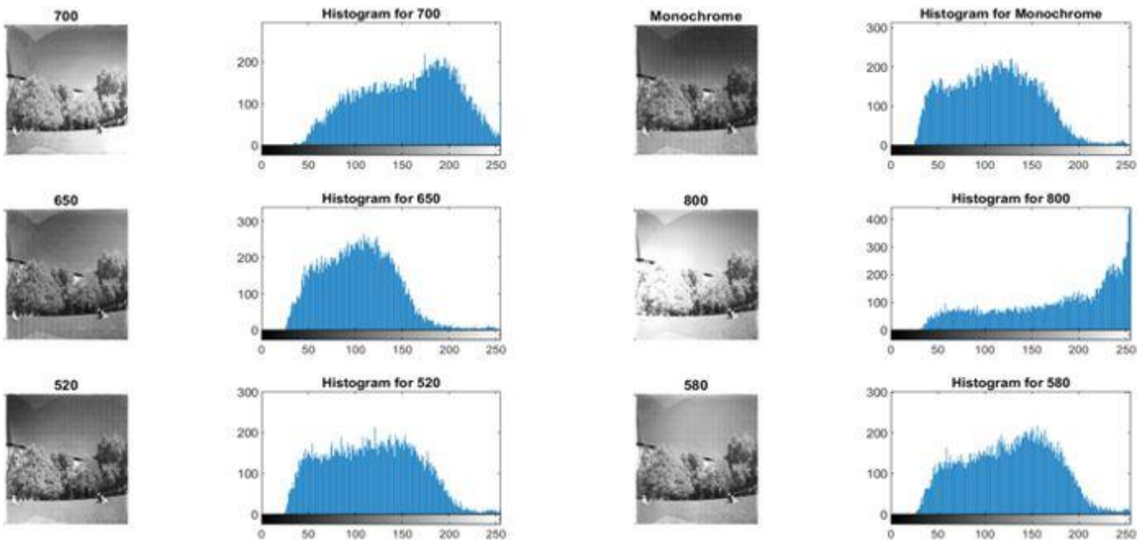

Figure A10 Images for 6 separate band after band collection.

Reference

[1] Tetracam. (2020, April). Retrieved from http://www.tetracam.com/

[2] Thorlab. (2020, April). Retrieved from https://www.thorlabs.com/